Organic light-emitting diodes with $FeCl_3$ intercalated few-layer graphene electrodes

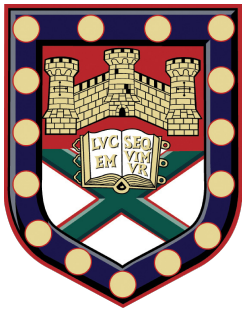

Submitted by Conor Murphy to the University of Exeter as a thesis for the degree of Doctor of Philosophy in Physics/Engineering

March 2022

I certify that all material in this thesis which is not my own work has been identified and that any material that has previously been submitted and approved for the award of a degree by this or any other university has been acknowledged.

Conor Murphy

ABSTRACT

Every day we interact with dozens of screens and touchscreens, as almost every consumer electronic device now has one. At the same time photovoltaic (PV) cells are becoming an important energy generation technology. All types of screens, such as those based on organic light-emitting diodes (OLEDs), and PVs, require a transparent conductive electrode (TCE) to enable charge carriers to enter/exit the device, while allowing light out of the screen or into the PV cell. Currently the material of choice for all these devices in commercial applications is indium tin oxide (ITO). However, there are some detrimental issues which face ITO. One of the most significant presently is its lack of flexibility. ITO is extremely brittle, making it unsuitable for use in bendable devices now being seen commercially for the first time. As wearables become more mainstream this will significantly limit its use in flexible applications, like clothing. Another major problem for ITO is the global indium stock. Reports vary, but it is estimated that there is as little as 30 years of indium left on the planet, of which its primary use is TCEs. Finally, there are other undesirable properties, such as the high financial cost, high environmental cost, and sub-optimal work function.

Graphene materials for the past decade and a half have been lauded as a major breakthrough in materials science with many possible applications, including as TCE. One form of graphene which has proven to have electrical and transmittance properties required to replace ITO in OLED technology is $FeCl_3$ intercalated FLG ($FeCl_3$-FLG). First reported in 2012, it was remarkable for its low sheet resistance, high optical transmittance, and notable unforeseen stability to humidity and heat. It has since shown potential scalability, increasing from the micron to wafer scale, and its work function matching with organic materials used in OLEDs and PVs indicates its potential suitability as TCE for high efficiency devices. The work presented in this thesis investigates the potential of $FeCl_3$-FLG as a possible replacement of ITO in OLEDs. This includes

a systematic investigation of its relevant properties for OLEDs, how and if the material can be integrated into such devices, and what is the resulting performance compared to ITO for a range of substrates, both rigid and flexible, while always ensuring low temperature, and solution processed fabrication.

The initial part of the thesis focuses on $FeCl_3$-FLG material optimisation and characterisation, as well as OLED materials and device fabrication optimisation. A $FeCl_3$-FLG material specific characterisation technique is developed using Raman spectroscopy to non-destructively assess the large-scale doping of few-layer graphene (FLG) induced by the $FeCl_3$ intercalation. Specifically, a metric is developed to represent the quality of intercalation, allowing for the direct comparison of the levels of intercalation in different samples, giving a more representative figure of the sample as a whole. A wafer-scale transfer technique is developed to enable the material to be transferred from its fabrication substrate (silicon wafer) to transparent or flexible substrates and used in large-area displays. A bending apparatus is developed that enables the measurement of the material's flexibility in a relevant way. This apparatus has shown that the resistance of ITO increases by a factor of 50 after just 100 bending cycles, while the resistance of $FeCl_3$-FLG increases by a factor of just 5 after 2000 bending cycles, demonstrating the superiority of $FeCl_3$-FLG a as flexible conductor. Fabrication of the OLEDs was developed and optimised for the combination of the equipment available, low temperature processing, and solution processed fabrication. Techniques were developed in-house to allow characterisation of OLED device performance such as luminance, emission profile, current efficiency, power efficiency, and external quantum efficiency.

The second part of the work describes the integration of $FeCl_3$-FLG into OLED devices. When comparing $FeCl_3$-FLG based devices to ITO based devices, the turn on voltage indicates good work function matching, however there was a reduction in performance, indicating material issues primarily surrounding roughness and lifetime. I investigated multiple ways to overcome the deficits of the material, such as encapsulation using a novel wax-based method. I then investigated several other ways of improving device performance including roughness and a new transfer technique. Finally, I propose and investigate a $FeCl_3$-FLG-ITO hybrid material which shows improved performance over $FeCl_3$-FLG in OLEDs, and a significant improvement in flexibility.

I show in this work that $FeCl_3$-FLG can work as a TCE in OLEDs, and that there

are signs that with more refined fabrication this could be achieved. I propose several ways of achieving this with refined methods. Significant further work is required to bring this material to commercial viability for use as a TCE in OLEDs.

ACKNOWLEDGEMENTS

Firstly, I would like to thank my supervisors: Professor Monica Craciun and Professor Saverio Russo. Your support and guidance at every step was invaluable, Monica for the continuous guidance and drive throughout, Saverio for the insight, assistance with LabVIEW and of course gardening tips during lockdown.

Thank you to everyone in the two research groups who has helped along the way, especially Kieran for invaluable chats about fabrication of materials and devices, Liping for guidance and expertise in OLED fabrication, and Adolfo for constant availability to help with Raman and other measurements. Thanks to Hong for always being helpful and patient, and also Mark, always on hand to help with problems, and reload the aluminium boat about 3 times a week after I've broken it.

Thanks to everyone in the CDT and my old housemates for always having great advice on issues in the lab, and of course being able to run off to the pub on a Friday evening and not discuss any of it!

Of course, thanks to my family, who are always keen to visit, help to de-stress, and provide financial bailouts when required! Hopefully this thesis will help you all understand what I do. I hope you enjoy reading it!

And most importantly thanks to Katie. For always being there to help when I needed it, and most importantly to put up with all my bullshit! You have made the whole process so much more enjoyable, being able to share it with you was the best part.

Finally, I acknowledge financial support from the Engineering and Physical Sciences Research Council (EPSRC) of the United Kingdom, via the EPSRC Centre for Doctoral Training in Metamaterials (Grant No. EP/L015331/1).

All data created during this research are available from the University of Exeter's institutional repository at https://doi.org/10.24378/exe.XXXX

Point of contact for any queries on the thesis/data and relevant code/software is M.F.Craciun@exeter.ac.uk

CONTENTS

LIST OF FIGURES

LIST OF TABLES

ACRONYMS

2D two-dimensional.

2DGF two-dimensional graphene film.

2LG bilayer graphene.

3D three-dimensional.

ACEL alternating current electroluminescent.

AFM atomic force microscopy.

ALD atomic layer deposition.

AZO aluminium doped zinc oxide.

CCD charge-coupled device.

CE current efficiency.

CNT carbon nanotube.

CVD chemical vapour deposition.

DC direct current.

DI deionised.

EBL electron blocking layer.

EIL electron injection layer.

EL electroluminescence.

EML emissive layer.

EQE external quantum efficiency.

ETL electron transport layer.

F8 poly(9,9-di-n-octylfluorenyl-2,7-diyl).

F8BT poly(9,9-dioctylfluorene-alt-benzothiadiazole).

FBZ first Brillouin zone.

$FeCl_3$-FLG:ITO $FeCl_3$-FLG enhanced ITO

$FeCl_3$-FLG $FeCl_3$ intercalated FLG.

FIB focused ion beam.

FLG few-layer graphene.

FoM figure of merit.

FWHM full width at half maximum.

GIC graphite intercalation compound.

HBL hole blocking layer.

HIL hole injection layer.

HOMO highest occupied molecular orbital.

HTL hole transport layer.

IPA propan-2-ol.

ITO indium tin oxide.

LCD liquid-crystal display.

LED light-emitting diode.

Liq 8-hydroxyquinolinolato-lithium.

LPE liquid-phase exfoliation.

LUMO lowest unoccupied molecular orbital.

NMP n-methyl-2-pyrrolidone.

OLED organic light-emitting diode.

OTR oxygen transmission rate.

PE power efficiency.

PEDOT:PSS poly(3,4-ethylenedioxythiophene) polystyrene sulfonate.

PEIE polyethylenimine ethoxylated.

PEN poly(ethylene 2,6-naphthalate).

PET polyethylene terephthalate.
PMMA poly(methyl 2-methylpropenoate).
PTFE poly(1,1,2,2-tetrafluoroethylene).
PV photovoltaic.
PVA poly(vinyl alcohol).
QE quantum efficiency.
RMS root mean squared.
SCLC space charge limited current.
SEM scanning electron microscope.
SKPFM scanning Kelvin probe force microscopy.
SLG single layer graphene.
TCE transparent conductive electrode.
TFB poly(9,9-dioctylfluorene-alt-N-(4-sec-butylphenyl)-diphenylamine).
TIR total internal reflection.
TO transverse optical.
UV ultraviolet.
UV-Vis ultraviolet-visible.
WVTR water vapour transmission rate.

1

INTRODUCTION

Over the past two decades display technology has become more mobile and versatile than ever before. It has become much more prevalent in our lives yet much less intrusive. We now have smaller and more useful displays than ever, and it is now widely recognised as an indispensable part of the modern world.[1] Mobile technology such as smartphones, smart watches, and tablets have meant technology has been able to penetrate deeper into our everyday lives. We are just now beginning to see curved, wearable and bendable display technologies integrate themselves into our lives too. They almost all contain high resolution full colour touchscreens. The thickness of these screens is now negligible as seen in recent "wallpaper" TVs. One feature they all lack however is real flexibility. Smartphones with rigid screens that are prone to breaking are in our pockets, TVs and displays which are a fixed size and shape hang on our walls, we wear smart watches and sports watches which need to be versatile and rugged, therefore they are commonly made from soft flexible components, except the screen. Some manufacturers have demonstrated "flexible" and curved demo devices. None of these currently available are fully flexible, only bendable in a very controlled way, involving complex hinge mechanisms. Future screens are envisaged to be fully flexible, however the technology needed to bring this idea to market is not yet fully developed.

Figure 1.1 shows an illustration of organic light-emitting diodes (OLEDs) from the point of view of their fabrication, properties, and applications. As mentioned, applications can include lighting, displays, and signage, however one aspect missing from this recent 2021 example which will appear shortly is in the wearables space. In terms of properties this relies on excellent mechanical flexibility and low cost. Both of these factors mean the fabrication must be carried out in a solution processed fashion.

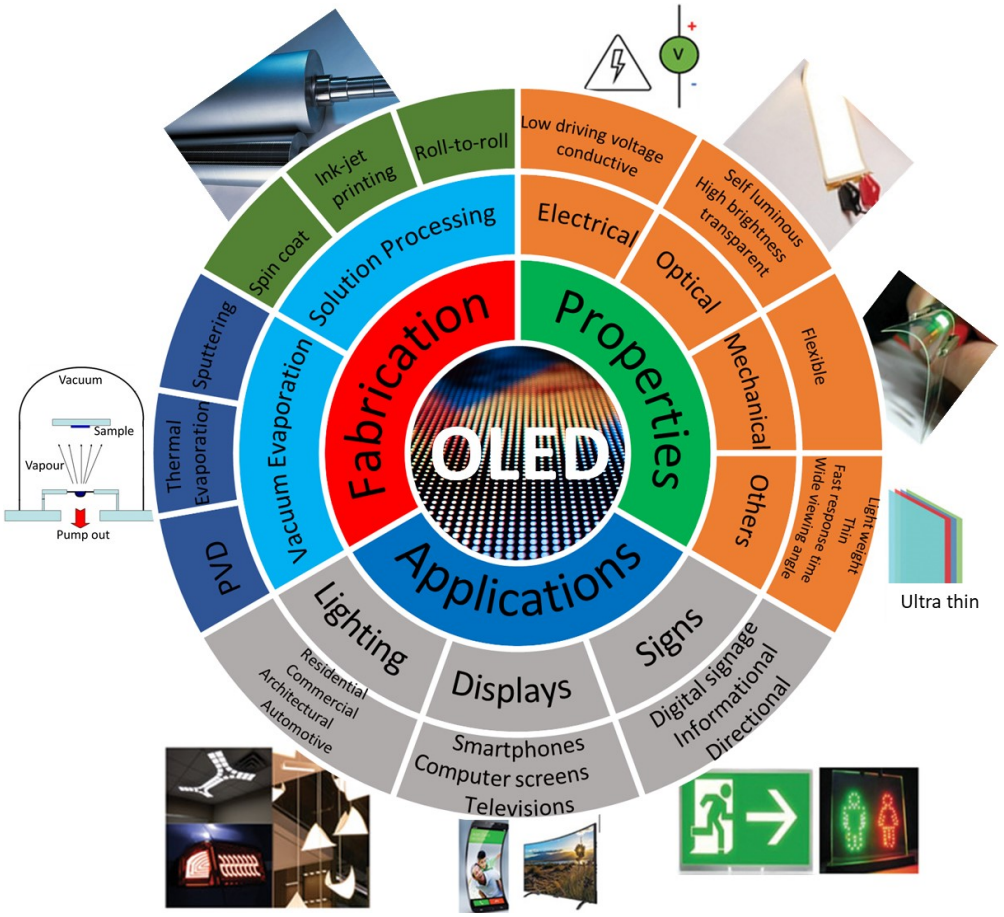

Figure 1.1: Illustration of OLEDs from three aspects: fabrication, properties, and applications. Reproduced with permission.[2]

It is this set of unrealised future application that drives the desire for low-cost, flexible, and solution processable devices at low temperature.

The screen technology which has been relied upon for almost all mobile and flat panel applications for the past two decades is liquid-crystal display (LCD). This has been the screen technology of choice for almost all high-performance applications. Developed in the 1960s and 1970s[3–8] it is now a mature technology. It has successfully overcome some fundamental hurdles such as viewing angle, response time and colour gamut.[9] This means it is now the go-to technology for high-end displays. Recently a newer technology known as OLED has begun to displace LCD in the small-sized display market.[10–12] OLED offers several advantages over LCD: negligible thickness ($< 1\ \mu m$),

infinite contrast ratios, wide colour gamut, high response rate and the potential to be both fully flexible and transparent.[12;13] It can do all of this while remaining comparable to LCD on viewing angle and power consumption. Almost all materials used in the manufacture of OLEDs can be chosen to be flexible; the notable exception is the transparent conductive electrode (TCE). Indium tin oxide (ITO) is used almost universally in displays as transparent electrode, however as a metal oxide it is not flexible. Under small applied tensile loads, it cracks, and conductivity is severely reduced. To make OLEDs in the future which are flexible, a TCE with properties to outperform ITO and flexibility will need to be found.

Graphene for the past decade and a half has been lauded as a major breakthrough in materials science. Discovered in 2004 after previously being thought to be inherently unstable, graphene was quickly discussed as being the superstar material for the 21^{st} century. In this thesis graphene shall refer only to the material in its single-layer form. In this form graphene has 97.7% optical transmittance, remarkably high electrical and thermal conductivity, and is the strongest known material. It is made up entirely of carbon and is therefore safe to use, stable, abundant, and environmentally friendly. Crucially, for use commercially its constituent element is extremely cheap. Graphene is just now reaching the point at which it is sufficiently understood to begin to integrate itself into our lives in the form of heat dissipation in smart phones, rigidity enhancement in footwear, and reinforcement and conductivity enhancement in building materials like asphalt.[14–16] While graphene has inherently attractive properties, it must prove itself to be significantly better, and offer more than currently used materials to justify the cost of redesigning devices and fabrication facilities to accommodate it.

One form of graphene which has proven it has the electrical and transmittance properties required to replace ITO in OLED technology is $FeCl_3$ intercalated FLG ($FeCl_3$-FLG).[17] By intercalating iron chloride molecules ($FeCl_3$) between each graphene layer in a stack of 3 - 10 layer graphene the conductivity can be improved to a level that outperforms ITO, while transmittance remains high. This $FeCl_3$-FLG brings flexibility, which ITO lacks, and high stability which other forms of doped graphene lack. Since it was first discovered in 2012, a unique gamut of properties associated with the material have been discovered. Examples include an unforeseen stability to harsh environmental conditions[19], ease of large-area processing[21] and the potential to enhance the efficiency of photovoltaic (PV) and OLEDs.[18;20–22] Figure 1.2 (a - d) shows some of the reported

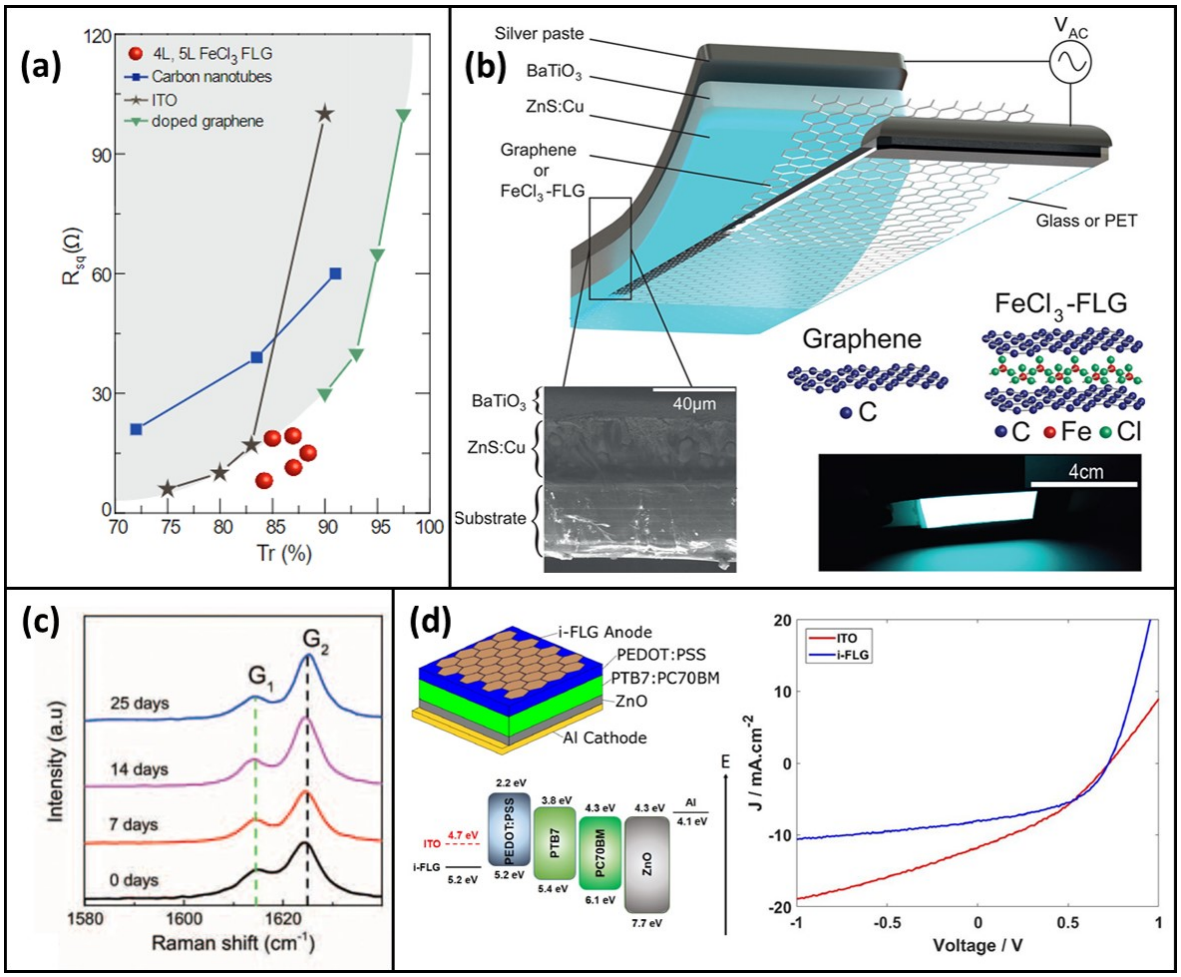

Figure 1.2: **(a)** Exceptional optoelectronic properties were reported for mechanically exfoliated $FeCl_3$-FLG for the first time in 2012.[17], **(b)** $FeCl_3$-FLG was integrated into a working ACEL device.[18] **(c)** $FeCl_3$-FLG showed exceptional stability compared to other intercalated graphene materials.[19] **(d)** $FeCl_3$-FLG was successfully integrated into a PV device.[20] Figures reproduced with permission.

properties of $FeCl_3$-FLG, such as its excellent optoelectrical properties, demonstration in alternating current electroluminescent (ACEL) devices, stability, and its successful demonstration in PVs.

The aim of this thesis is to investigate $FeCl_3$-FLG as a candidate for replacing ITO in OLEDs. In Chapter 2 I will introduce the main theoretical and empirical background to graphene, functionalised graphene, TCEs, OLEDs, and finally, provide some context

in the form of a review of recent publications involving graphene-based OLEDs.

In Chapter 3 I will introduce the experimental background; this will be the work done in the past which I have extensively used and which an understanding of is required. Here I will primarily outline the fabrication and characterisation techniques used later in this work.

Chapter 4 will cover the experimental development. This is the experimental work, which was improved on, or produced entirely by me. This work is critical to investigating the devices and materials specific to this work.

In Chapter 5 I will investigate $FeCl_3$-FLG as a TCE in OLEDs. I will look at the performance in two different device architectures and compare to ITO at all times.

Chapter 6 will investigate the roll of encapsulation in device longevity. I will look at some of the more common encapsulation methods, as well as a novel encapsulation method. The purpose of this chapter is to address some of the device stability issues highlighted in the previous chapter.

Chapter 7 will continue along this line, by employing several other strategies to improve the device and electrode performance, and propose an alternative hybrid material which might be able to address them.

Chapter 8 will look at a novel hybrid graphene based TCE as a potential solution to the poor performance exhibited by $FeCl_3$-FLG in OLEDs. I will characterise this material and investigate its performance in OLED devices.

Finally, in Chapter 9 I will conclude the work by summarising the main points from each chapter, and discussing what future work can be done based on the results of this thesis.

BIBLIOGRAPHY

[1] Joseph A. Castellano. *Handbook of Display Technology*. Academic Press, 1992.

[2] Adeniji E. Adetayo, Tanjina N. Ahmed, Alex Zakhidov, and Gary W. Beall. Improvements of Organic Light-Emitting Diodes Using Graphene as an Emerging and Efficient Transparent Conducting Electrode Material. *Advanced Optical Materials*, 9(14):2002102, 7 2021.

[3] George H. Heilmeier, Louis A. Zanoni, and Lucian A. Barton. Dynamic Scattering: A New Electrooptic Effect in Certain Classes of Nematic Liquid Crystals. *Proceedings of the IEEE*, 56(7):1162–1171, 1968.

[4] G. H. Heilmeier, L. A. Zanoni, and L. A. Barton. Dynamic scattering in nematic liquid crystals. *Applied Physics Letters*, 13(1):46–47, 7 1968.

[5] G. H. Heilmeier, L. A. Zanoni, and L. A. Barton. Further Studies of the Dynamic Scattering Mode in Nematic Liquid Crystals. *IEEE Transactions on Electron Devices*, ED-17(1):22–26, 1 1970.

[6] M. Schadt and W. Helfrich. Voltage-dependent optical activity of a twisted nematic liquid crystal. *Applied Physics Letters*, 18(4):127–128, 2 1971.

[7] M. F. Schiekel and K. Fahrenschon. Deformation of nematic liquid crystals with vertical orientation in electrical fields. *Applied Physics Letters*, 19(10):391–393, 11 1971.

[8] R. A. Soref. Transverse field effects in nematic liquid crystals. *Applied Physics Letters*, 22(4):165–166, 2 1973.

[9] Deng Ke Yang and Shin Tson Wu. *Fundamentals of Liquid Crystal Devices*, volume 9781118752. 2014.

[10] Bernard Geffroy, Philippe le Roy, and Christophe Prat. Organic light-emitting diode (OLED) technology: Materials, devices and display technologies. *Polymer International*, 55(6):572–582, 6 2006.

[11] Alastair Buckley. *Organic Light-Emitting Diodes (OLEDs): Materials, Devices and Applications*. 2013.

[12] Takatoshi Tsujimura. *OLED Display Fundamentals and Applications*. John Wiley & Sons, Inc., Hoboken, New Jersey, 4 2017.

[13] David Barnes. LCD or OLED: Who wins? *Digest of Technical Papers - SID International Symposium*, 44(1):26–27, 6 2013.

[14] Huawei Mate P30 Pro adopts a graphene-based heat management film — Graphene-Info.

[15] Versarien to provide graphene-enhanced elastomers to Flux Footwear — Graphene-Info.

[16] New graphene-enhanced asphalt trial to take place on Oxford road — Graphene-Info.

[17] Ivan Khrapach, Freddie Withers, Thomas H. Bointon, Dmitry K. Polyushkin, William L. Barnes, Saverio Russo, and Monica F. Craciun. Novel highly conductive and transparent graphene-based conductors. *Advanced Materials*, 24(21):2844–2849, 6 2012.

[18] Elias Torres Alonso, George Karkera, Gareth F Jones, Monica F Craciun, and Saverio Russo. Homogeneously Bright, Flexible, and Foldable Lighting Devices with Functionalized Graphene Electrodes. *ACS Applied Materials and Interfaces*, 8(26):16541–16545, 2016.

[19] Dominique Joseph Wehenkel, Thomas Hardisty Bointon, Tim Booth, Peter Bøggild, Monica Felicia Craciun, and Saverio Russo. Unforeseen high temperature and humidity stability of FeCl3 intercalated few layer graphene. *Scientific Reports*, 5(1):7609, 7 2015.

[20] Kieran K. Walsh, Conor Murphy, Saverio Russo, and Monica F. Craciun. Improved Stability of Organic Photovotlaic Devices With FeCl3 Intercalated Graphene Electrodes. *Frontiers in Electronics*, 2:2, 4 2021.

[21] Thomas H. Bointon, Matthew D. Barnes, Saverio Russo, and Monica F. Craciun. High Quality Monolayer Graphene Synthesized by Resistive Heating Cold Wall Chemical Vapor Deposition. *Advanced Materials*, 27(28):4200–4206, 7 2015.

[22] Thomas H. Bointon, Gareth F. Jones, Adolfo De Sanctis, Ruth Hill-Pearce, Monica F. Craciun, and Saverio Russo. Large-area functionalized CVD graphene for work function matched transparent electrodes. *Scientific Reports*, 5(1):16464, 12 2015.

2

THEORETICAL BACKGROUND AND CONTEXT

2.1 GRAPHENE

2.1.1 *Discovery of graphene*

The term graphene was first used in 1986 by Boehm et al. when referring to a single layer of graphite in the context of graphite intercalation compounds (GICs).[1] At this time an intense amount of research had already been done theoretically and experimentally on graphite. The interesting properties of graphite have been known since 1947, and even graphene was theoretically studied at this time by Philip R Wallace and its electrical properties predicted.[2] Experimentally this research was not verified until 2004.[3] This was due primarily to the fact it was thought to be an impossible material to exist in isolation. It had been shown theoretically in the 1930s that in its monolayer form graphite would be thermally unstable.[4;5] This prevented scientists from looking further into the material in the mid twentieth century. It wasn't until 2004 in Manchester that Andre Geim and Konstantin Novoselov isolated and characterised graphene on a SiO_2 substrate that the material was discovered.[3] They characterised the materials structure, and properties, particularly its extraordinary electrical properties for the first time. This led to them winning the 2010 Nobel Prize in physics.

Before graphene was officially discovered in 2004 a vast amount of research was done on other carbon-based materials. Carbon nanotubes (CNTs), are form of carbon similar to graphene, where graphene monolayers, bilayers and few layers can be thought of as being rolled-up into a tube. Before these, graphite-based materials such as GICs were widely studied. I will revisit these later as with few-layer graphene (FLG) they

can vastly enhance the electrical properties.

As it became known that the forces between carbon atoms in graphite are highly anisotropic, attention turned again to producing FLG or even single layer graphene (SLG). The inter-planar forces between individual sheets of graphite were known to be up to two orders of magnitude smaller than those forces connecting atoms in the plane.[6;7] This led to researchers to begin to attempt to mechanically separate graphite into its constituent layers.[8;9] It wasn't until 2004 that this process, using the micro-mechanical cleavage technique, also popularly known as the "scotch tape" method, resulted in the isolation of graphene on a SiO_2 substrate.[3]

2.1.2 *Structure of graphene*

2.1.2.1 *Carbon*

Carbon is the only element present in graphene. The element is the fourth most abundant in the universe and its chemical versatility makes it the base element of life on Earth. It occurs naturally on this planet in several forms. The most well-known form being amorphous carbon, graphite, and diamond. Its chemical versatility allows it to react readily to form large and small stable compounds. In chemistry any compound containing carbon is known as "organic".

The atom itself is the sixth on the periodic table and has two stable isotopes, C^{12} which is the most abundant and C^{13} which is much rarer. C^{14} is also one of the best known non-stable isotopes of carbon, used famously in C^{14} dating.

Carbon has six electrons arranged in atomic orbitals in the form $1s^2$, $2s^2$, $2p^2$. In carbon the energy difference between the 2s and 2p orbitals is much smaller than their bond energy, this leads to their wave functions combining in a process called hybridization. This results in three hybrid orbitals known as sp, sp^2 and sp^3. Each of these bonding orbitals yields a different form of carbon.

In sp bonding carbon can bond through either bonding with two double bonds or a triple and a single bond to two other elements. This means the bonding will give a linear arrangement of atoms (180 ° bonding angle). This is common in organic compounds such as polymers but is not common in solid crystals.

In sp^2 bonding a carbon atom can bond through a double bond and two single bonds to three other elements. This gives a molecule which is flat and has a bond angle of

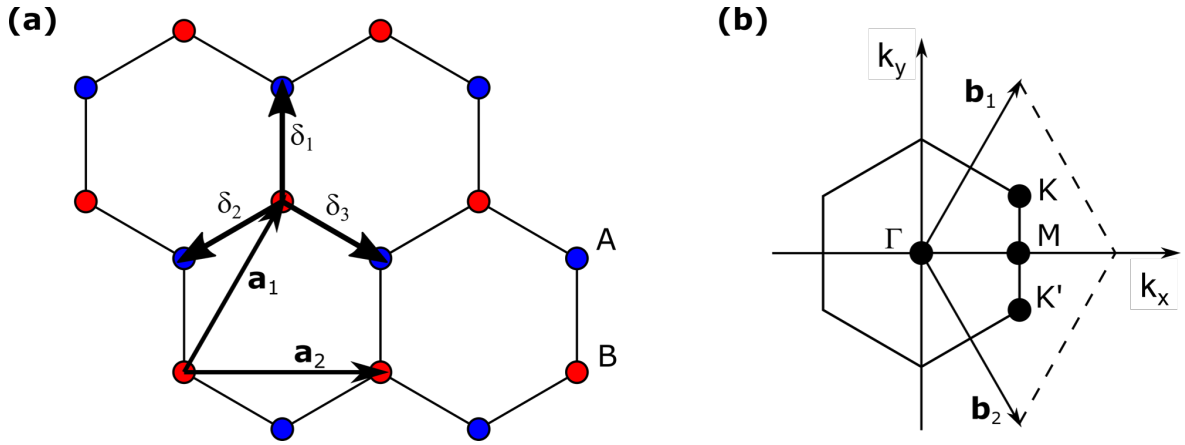

Figure 2.1: **(a)** Hexagonal lattice structure of graphene with sublattices A and B in blue and red. The lattice vectors, $\mathbf{a_1}$ and $\mathbf{a_2}$, and the nearest neighbour distances, δ_1, δ_2 and δ_3 are shown. **(b)** The Brillouin zone of the reciprocal lattice. Lattice vectors, $\mathbf{b_1}$ and $\mathbf{b_2}$, and high symmetry points, Γ, K, K', and M are shown.
. Reproduced with permission.[10]

120 °. This is known as a trigonal planar configuration. This bonding configuration leaves an unbonded, unhybridized $2p_z$ orbital, perpendicular to the others. The sp^2 bonds are known as σ bonds and are much stronger than the unbonded $2p_z$ π bond. It is this π bond that bonds with other layers of graphene to form graphite, and which is responsible for graphene's conductivity. This π bond is much weaker than the σ bonds and is what allows for mechanical cleavage of graphite layers into graphene.

In sp^3 bonding a carbon atom can bond through four single bonds to four other elements in a tetrahedral structure where the bond angle is 109.5 °. This leads to four extremely strong σ bonds. This is the atomic structure seen in diamond.

2.1.2.2 *Graphene lattice & energy band structure*

Graphene consists of a planar array of sp^2 bonded carbon atoms which form a honeycomb or chicken wire lattice structure. Each carbon atom is σ bonded to three adjacent carbon atoms. In graphene the $2p_z$ orbital, perpendicular to the graphene plane is left unbonded and results in strong electron delocalisation, and therefore the unique electrical properties that can be seen in graphene, these can be calculated by applying the tight-binding model.[10]

The crystal structure of graphene can be seen in Figure 2.1 (a). The Bravais lattice is trigonal planar, and the unit cell is a rhombus with a basis of 2 (A & B). The unit cell contains one atom from each sub-lattice. The lattice vectors can be written in terms of the length of the σ bonds between carbon atoms, a. The lattice vectors of the sub-lattice denoted A are[10]:

$$\mathbf{a}_1 = \frac{a}{2}\left(3, \sqrt{3}\right) \tag{2.1}$$

$$\mathbf{a}_2 = \frac{a}{2}\left(3, -\sqrt{3}\right) \tag{2.2}$$

where $a = 1.42$ Å.

The first Brillouin zone (FBZ) (Figure 2.1 (b)) is also hexagonal and has the following reciprocal lattice vectors:

$$\mathbf{b}_1 = \frac{2\pi}{3a}\left(1, \sqrt{3}\right) \tag{2.3}$$

$$\mathbf{b}_2 = \frac{2\pi}{3a}\left(1, -\sqrt{3}\right) \tag{2.4}$$

The high symmetry points worth noting in the FBZ are K and K' whose wave vectors are described by:

$$\mathbf{K} = \left(\frac{2\pi}{3a}, \frac{2\pi}{3\sqrt{3}a}\right) \tag{2.5}$$

$$\mathbf{K}' = \left(\frac{2\pi}{3a}, \frac{2\pi}{3\sqrt{3}a}\right) \tag{2.6}$$

The energy band structure of graphene can be calculated by solving the Schrodinger equation using the tight binding Hamiltonian if only the interactions between the orbitals which take part in σ bonding are considered, i.e. the vectors δ_1, δ_2 and ${\delta_3}^2$ (Figure 2.1 (a)). Doing this gives us the energy dispersion:

$$E(k_x, k_y) = \pm\gamma_0\sqrt{1 + 4cos\left(\frac{3ak_x}{2}\right)cos\left(\frac{\sqrt{3}ak_y}{2}\right) + 4cos^2\left(\frac{\sqrt{3}ak_y}{2}\right)} \tag{2.7}$$

Here $\gamma_0 \approx 2.8eV$.[10] This is the hopping integral between nearest neighbour atomic orbitals. When this equation is plotted, as has been done in Figure 2.2, with k_x and k_y extending out beyond the FBZ, valence and conduction bands are formed, where for the

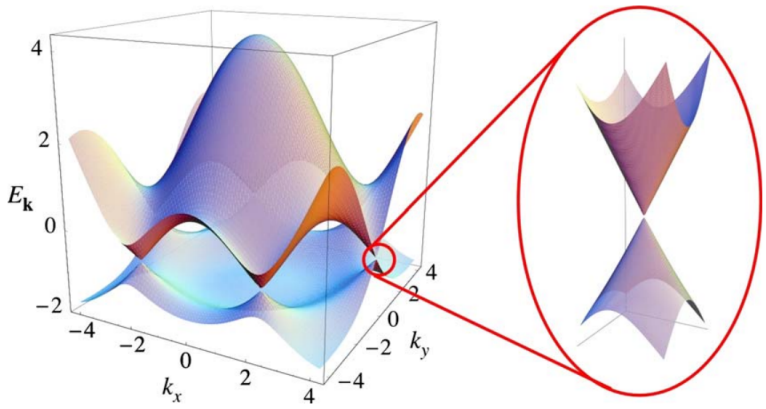

Figure 2.2: The electronic energy dispersion of monolayer graphene from Equation 2.7. It can be seen here that the π and π^* bands touch at the K and K' points. The zoomed image shows energy bands at one of these Dirac points. Reproduced with permission.[10]

valence band $E < 0, \pi$ and $E > 0, \pi^*$ for the conduction band. These bands intersect at the K and K' points of the reciprocal lattice to give E = 0. The free p_z electrons completely fill the π-band and leave the π^*-band completely empty. This results in the Fermi energy, E_F, of pristine graphene being exactly at these intersection points. This leaves us to conclude that graphene is a zero-gap semiconductor, or a semi-metal. It also allows us to predict the transport properties of experimentally doped graphene by evaluating Equation 2.7. In SLG the bands at the K points are linear, as seen in Figure 2.2. In FLG the band structure is parabolic, as the layers increase the bands continue to change, 3 and 5 layer have a combination of linear and parabolic bands, 4 layer has several parabolic bands.[11;12] This multi-layer graphene is no longer a zero-gap semiconductor. This is important because there is an obvious distinction between SLG and FLG. When FLG is intercalated, the layers separate and the band structure goes back to that of SLG, this indicates the decoupling of the graphene layers. This will be seen later in the Raman 2D peak of graphene (Figure 3.10), which reflects the band structure. In FLG there is a multi-Lorentzian which becomes a single Lorentzian when the layers are decoupled.[13;14] We show this later in Figure 3.11 (c).

2.1.2.3 *Optical absorption of graphene*

Graphene can absorb light via direct ($\Delta k = 0$) or indirect ($\Delta k \neq 0$) excitation of a π electron by a photon of appropriate energy. Figure 2.2 shows that the direct absorption of photons can occur (for photons of energies up to 3.96 eV[15]) by exciting electrons from the π band to the π^* band. Looking at the measured optical transmittance of graphene in the visible region of the spectrum it is flat for SLG, but also FLG. In fact, SLG is known to absorb approximately 2.3% of white light per graphene sheet. Each sheet results in another 2.3 percentage points of absorption. This however has been recently challenged by new research suggesting this number may be substrate dependant.[16] When n-doped graphene is considered, the Pauli Exclusion Principle prevents excited electrons from entering the conduction band from the valence band by photons which have energy $hv < 2|E_F|$. The same is true for p-doped graphene due to the absence of available ground state electrons.

2.1.3 *Production methods*

2.1.3.1 *Micromechanical cleavage*

As previously mentioned, graphene was discovered in 2004 by the successful use of the micromechanical cleavage method.[3] This method makes use of the fact that graphite is essentially just sheets of graphene, loosely bound to one another. As mentioned, the inter-sheet forces are two orders of magnitudes less than the inter-atomic forces. This means it should be possible to mechanically separate sheets without damaging each individual sheet. This method involves putting graphite on adhesive tape, folding the tape onto itself and the graphite and peeling apart. Done repeatedly this can result in graphite being exfoliated to SLG. The SLG can then be transferred onto a substrate such as SiO_2 for characterisation.

While this technique was pivotal in graphene's initial discovery and characterisation, it is not scalable. The graphene flakes produced by this method are high-quality, single-crystalline, however they are on the order of microns in size and are very few in number, most flakes produced are some kinds of FLG.[3] These are not commercially viable sizes or yields.

2.1.3.2 *Liquid-phase exfoliation of graphite*

One method developed to address the yield, is known as liquid-phase exfoliation (LPE). LPE results in a suspension of SLG and FLG flakes in liquid. Graphite powder is typically dispersed in a liquid such as deionised (DI) water with soap or n-methyl-2-pyrrolidone (NMP). Because graphite is hydrophobic, dispersion in DI water requires a surfactant. NMP is often used as it is non-polar and has a surface tension that prevents the exfoliated graphene from reaggregation. The suspended graphite is exfoliated by exposing to high frequency sonic waves (known as ultrasonication), typically using a horn-tip sonicator. Another method involves using a blender and is known as shear exfoliation. The SLG and FLG can be separated through centrifuging after sonication and the properties of the suspended graphene inferred by ultraviolet-visible (UV-Vis) spectroscopy. This production method is scalable and has been used commercially before.[17–19] The issue with this method is the quality and size of graphene produced. The flakes are sub-micron sized and often contaminated with oxidants. They can be made into conductive inks; however any such ink cannot be transparent.[20;21]

2.1.3.3 *CVD*

For high quality material production at a large scale chemical vapour deposition (CVD) is the production technique developed and used in research and industry. Modern techniques allow CVD graphene to be as good as that obtained by micromechanical cleavage, although on a macro-scale.[22] These CVD methods allow for graphene to be grown in SLG or FLG form on a range of metal substrates.

The process was first developed for graphene production in 2008[23;24] and can broadly described as follows: A metal substrate in a vacuum furnace is heated. A small carbon containing compound (such as methane), known as the carbon precursor, in gaseous form is pumped into the furnace. In the case of nickel, the substrate catalyses the decomposition of the carbon compound, and the carbon atoms are absorbed into the metal. The furnace is quickly quenched resulting in carbon being adsorbed onto the metals surface to form graphene. The remaining gasses are pumped out. In the case of copper carbon does not dissolve into the substrate, it forms nucleation sites on the surface, more carbon atoms join and graphene is formed on the surface. Both of these processes can be seen in Figure 2.3.

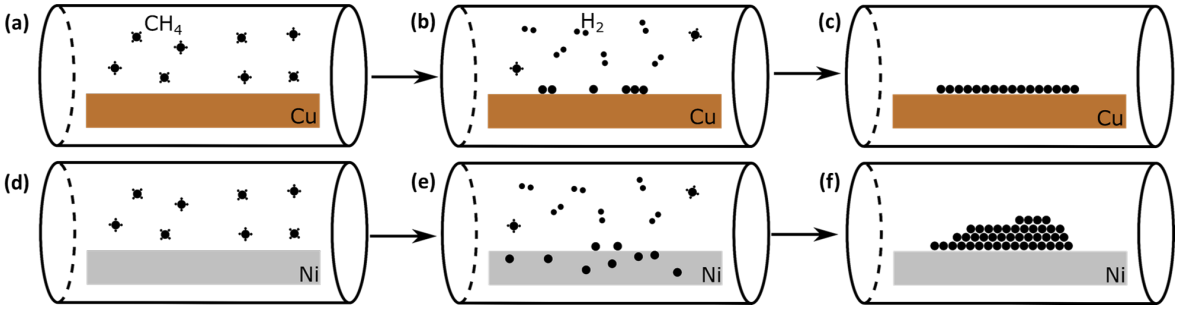

Figure 2.3: The chemical vapour deposition process for copper and nickel. Performed in vacuum, a carbon precursor is pumped into the furnace **(a & d)**, in this case CH_4. The furnace is heated, and the carbon atoms are adsorbed/absorbed onto/into the surface of the copper or nickel respectively **(b & e)**. Upon quenching the carbon forms SLG or FLG on the substrate for copper or nickel, respectively **(c & f)**.

This method allows for the tuning of the number of graphene layers by selecting the quenching rate, metal substrate, gas pressure, choice of carbon precursor and initial furnace pressure. Most commonly, copper substrates allow for the growth of large-area pristine single-crystalline SLG. On copper the surface coverage of SLG can be as high as 98%.[25] Nickel is often used to grow a patchwork of FLG domains.[26;27] This sounds like a technique that would not be useful, however it can allow for much more successful doping and tuning of the material properties of graphene and will be discussed in Section 2.2.3.1 and Section 2.3.3.3. Recently metal-free CVD graphene growth has been demonstrated; this could result in higher quality graphene with larger domains in future.[28]

2.2 FUNCTIONALISED GRAPHENE

2.2.1 *Introduction*

Even though graphene is the strongest known material, the best known electrical and thermal conductor, and is also flexible and transparent, its properties do not always fit the criteria required for certain applications. As a zero band gap, highly conductive material, graphene cannot be used as a gated transistor without doping to open up a band gap. Its conductivity is simultaneously not high enough to outperform conductivities currently seen in other transparent conductor materials. To overcome some

of these issues, graphene must be functionalised to tune its properties, particularity conductivity. The conductivity of pristine graphene is of the order of 1 $k\Omega/\square$, this needs to be brought down to the order of 1 - 10 $\Omega/\square$.

A range of different functionalisation methods have been demonstrated before with varying success.[29] Graphene has been functionalised and it has been shown that through intercalation of FLG with $FeCl_3$ graphene can be the best-known transparent conductor, outperforming the 150 *nm* thick industry leader indium tin oxide (ITO) in transmittance and conductivity, while also adding flexibility.[13]

2.2.2 *Monolayer graphene doped with physisorbed species*

As previously discussed, graphene is a zero-gap semi-metal.[10] This lack of an energy gap is due to the energetic equivalence of the sublattices which make up the unit cell of graphene. With chemical doping we can tune the Fermi level of graphene, making it a better electron or hole conductor. This can be done by either substituting a carbon atom for some dopant atom, or by covalently bonding at atom to the graphene lattice. Substitutional doping can be advantageous from a stability point of view, however charge carrier mobility often decreases due to defects and disorders that have been introduced.[30] Covalent functionalisation is any functionalisation which involves bonding a molecule, and oxide or fluorine or hydrogen to graphene. This kind of graphene has been reported many times in the case of $AuCl_3$ doping,[31] Au doping,[32], and HNO_3 doping.[33]

2.2.3 *Graphite intercalation compounds*

Intercalation is another effective way of functionalising graphene. GICs have been studied intensively for decades for bulk graphite. Intercalation has long been a method used to functionalise bulk graphite to change its properties. A vast number of unique and novel properties were discovered in graphite, such as an intrinsic superconducting state and magnetic properties.[34]

Adapting this method of functionalisation for FLG has also been very successful. Initially this success came in the form of two-dimensional graphene film (2DGF). These films are intercalated on their growth substrates, usually metallic, insulating or carbidic substrates. As a result, they are electronically coupled to the substrate.

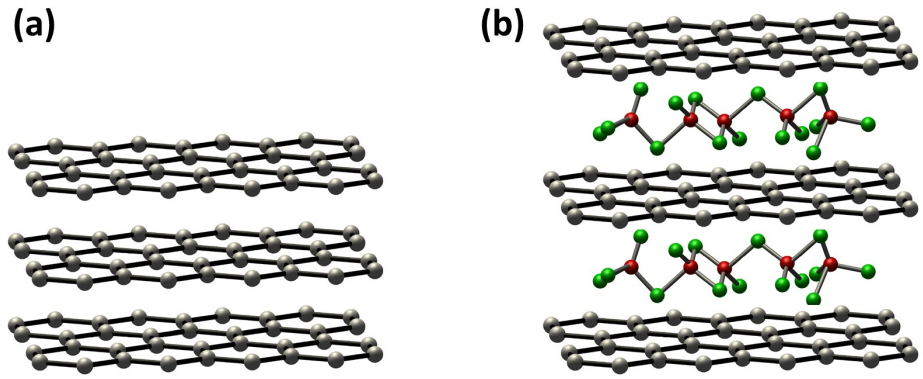

Figure 2.4: **(a)** A stack of FLG. **(b)** Intercalated FLG, known as $FeCl_3$ intercalated FLG ($FeCl_3$-FLG).

The electronic spectrum of these materials is heavily influenced by the substrate, only graphene deposited on SiO_2, Si_3N_4, glass, quartz or graphene in a liquid suspension has a pristine electronic spectrum.[29] Graphene on these substrates is commonly referred to as quasi-free, SLG and FLG. Quasi-free FLG has been successfully intercalated with several intercalates. Using the vapour-phase intercalation method K[35;36], Rb[36], ICl, IBr[37] and $FeCl_3$[13] were successfully intercalated. The intercalation for these occurred in a two-zone furnace at temperatures ranging from 35°C for IBr to 350°C for $FeCl_3$. The result of this intercalation on the FLG is the G peak, seen in Raman spectra of graphene, is upshifted. This shows that a large charge transfer between the graphene and the intercalate is occurring. Intercalation is one of the most promising doping methods as it is highly uniform and highly scalable.

2.2.3.1 *$FeCl_3$-intercalated few-layer graphene*

$FeCl_3$-intercalated few-layer graphene, sometimes dubbed GraphExeter, and referred to in this thesis as $FeCl_3$-FLG was discovered in 2012 at the University of Exeter.[13] A form of p-doped graphene, composed of 2 - 10 graphene layers intercalated with $FeCl_3$ (seen in Figure 2.4), it is the best-known flexible, transparent conductor. The few-layer graphene structure can be seen in Figure 2.4 (a) and the $FeCl_3$-FLG can be seen in Figure 2.4 (b). The effect of the $FeCl_3$ is to p-dope the FLG by increasing the charge carrier density of the material. The Fermi level of the FLG is raised and an upshift the G peak of the Raman spectrum of FLG from 1580 cm^{-1} to 1625 cm^{-1} is

observed. The transmittance of FLG is largely unaffected by the intercalation (approx. 85% for 5-layer) whereas the sheet resistance of the two-dimensional (2D) material is reduced from 1 $k\Omega/\square$ to 8.8 $\Omega/\square$. Charge carrier densities in $FeCl_3$-FLG too have been reported to be extremely high, up to 9×10^{14} cm^{-2}. Alongside a charge carrier mobility of 1000 $cm^2V^{-1}s^{-1}$ the mean free path of $FeCl_3$-FLG is almost 1 μm at room temperature.[29] This extremely large mean free path present is also not dependant on substrate as is the case for pristine graphene. This very large mean free path has been observed on SiO_2/Si, as well as on glass. It is believed that the high charge densities in $FeCl_3$-FLG screen the charge defects of the substrate material, this makes the electrical properties of $FeCl_3$-FLG extremely consistent and not dependant on the quality of the supporting substrate. When $FeCl_3$-FLG is analysed under Raman and magneto-electric experiments done, it can be seen that the charge carriers in each graphene layer are effectively decoupled. This can be seen in the Raman spectrum when looking at the 2D-band.[13] In FLG, and graphite, this band is a convolution of 2D peaks from each graphene layer, in $FeCl_3$-FLG however this peak is seen as a single Lorentzian. In magneto-electric experiments, the temperature dependence clearly shows that the charge carriers of the intercalated species are still Dirac fermions.[13] Finally the stability of $FeCl_3$-FLG is also highly impressive. Many GICs and intercalated FLG species are highly unstable in both oxygen and a high humidity environment. This renders these materials inviable for practical day-to-day applications. $FeCl_3$-FLG by contrast is highly stable. It is resistant to oxygen environments; high temperature environments and high humidity environments.[38] All of this means $FeCl_3$-FLG is an ideal material for a wide range of manufacturing techniques. Being able to transfer the material between substrates is especially important if a material is to be commercially viable.

2.3 TRANSPARENT CONDUCTIVE ELECTRODES

2.3.1 *Introduction*

A hugely important material category in the modern world are that of transparent conductive electrodes (TCEs). TCEs are used in a wide variety of modern technologies. Almost every screen in the world today has a TCE just under the glass. TCEs are used to detect your finger in touchscreen devices, and as electrodes in liquid-crystal display (LCD) and organic light-emitting diode (OLED) screen technologies. They are also

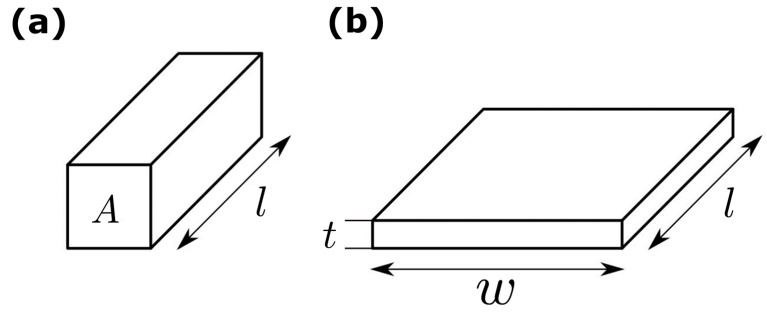

Figure 2.5: **(a)** A 3-dimensional object with length, l and face with area, A. **(b)** A thin film of length, l, width w and negligible thickness, t.

used as electrodes in photovoltaic (PV) devices. In PV devices efficiency is of extreme importance. In screen technologies, cost, environmental impact and now flexibility and physical robustness are most important. In OLED and PV devices, work function too is especially important. Mismatched work functions between layers will result in reduced device efficiency.

In this thesis I will look at a number of properties to evaluate the usefulness of materials for flexible transparent electrode applications. When discussing optical transmittance, I will quote and compare optical transmittance at 550 nm. In some cases, I will mention how the transmittance is uniform over the visible spectrum (400 nm to 800 nm), this just means that the transmittance in the visible range is approximately the same at all wavelengths. I will also compare the conductivity of materials. For thin films the best way to do this is to look at the sheet resistance, R_S:

$$R = \rho\frac{l}{A} = \frac{\rho}{t}\frac{l}{w} = R_S\frac{l}{w} \tag{2.8}$$

Where R is the conventional electrical resistance, ρ is the resistivity, A is the area of the thin film and l, w and t are the length width and thickness of the film respectively. Because thickness is meaningless in a negligibly thin film the sheet resistance, R_S, is defined as $\frac{\rho}{t}$. $R_S = R$ only when an arbitrary square of the thin film is taken into consideration. This can be visualised in Figure 2.5, where a bulk three-dimensional (3D) conductor can be seen in Figure 2.5 (a) and a 2D conductor with negligible thickness can be seen in Figure 2.5 (b).

2.3.2 *Figure of merit*

Figure of merit (FoM) proposed by De et al.[39] will be used to compare materials which have differing levels of transmittance and sheet resistance. This figure is the direct current (DC) to optical conductivity ratio and is expressed as σ_{DC}/σ_{Op}. This figure is used as optical transmittance and sheet resistance are linked, and therefore can be expressed together as a single figure. The sheet resistance can be expressed as follows:

$$R_S = (\sigma_{DC} t)^{-1} \tag{2.9}$$

where t is the thickness of a thin film. The optical transmittance can be expressed as

$$T = \left(1 + \frac{Z_0}{2}\sigma_{Op} t\right)^{-2} \tag{2.10}$$

where Z_0 is the impedance of free space (377 Ω). This equation arises from the fact that optical conductivity is related to the Lambert-Beer absorption coefficient, α, by $\sigma_{Op} \approx 2\alpha/Z_0$. The equations for T and R_S above combine to give the following:

$$FoM = \frac{\sigma_{DC}}{\sigma_{Op}} = \frac{Z_0}{2R_S(T^{-0.5} - 1)} \tag{2.11}$$

This equation shows that T and R_S are related by σ_{DC}/σ_{Op} which is the FoM.

What this means for materials with various properties can be seen by plotting sheet resistance as a function of transmittance for various FoMs. This can be seen in Figure 2.6. The black line in Figure 2.6 (a) roughly indicates where the slope is greater than 1, and so where this is the case improving the transmittance will result in the largest increase in FoM, where the slope is less than 1 improving the sheet resistance will result in the largest increase in FoM. All the graphene-based TCEs presented in this work are in the region seen in Figure 2.6 (b), here changes in transmittance will have a much larger effect on the FoM. The goal being to increase the FoM by as much as possible, with higher FoM materials having more appropriate properties as TCE.

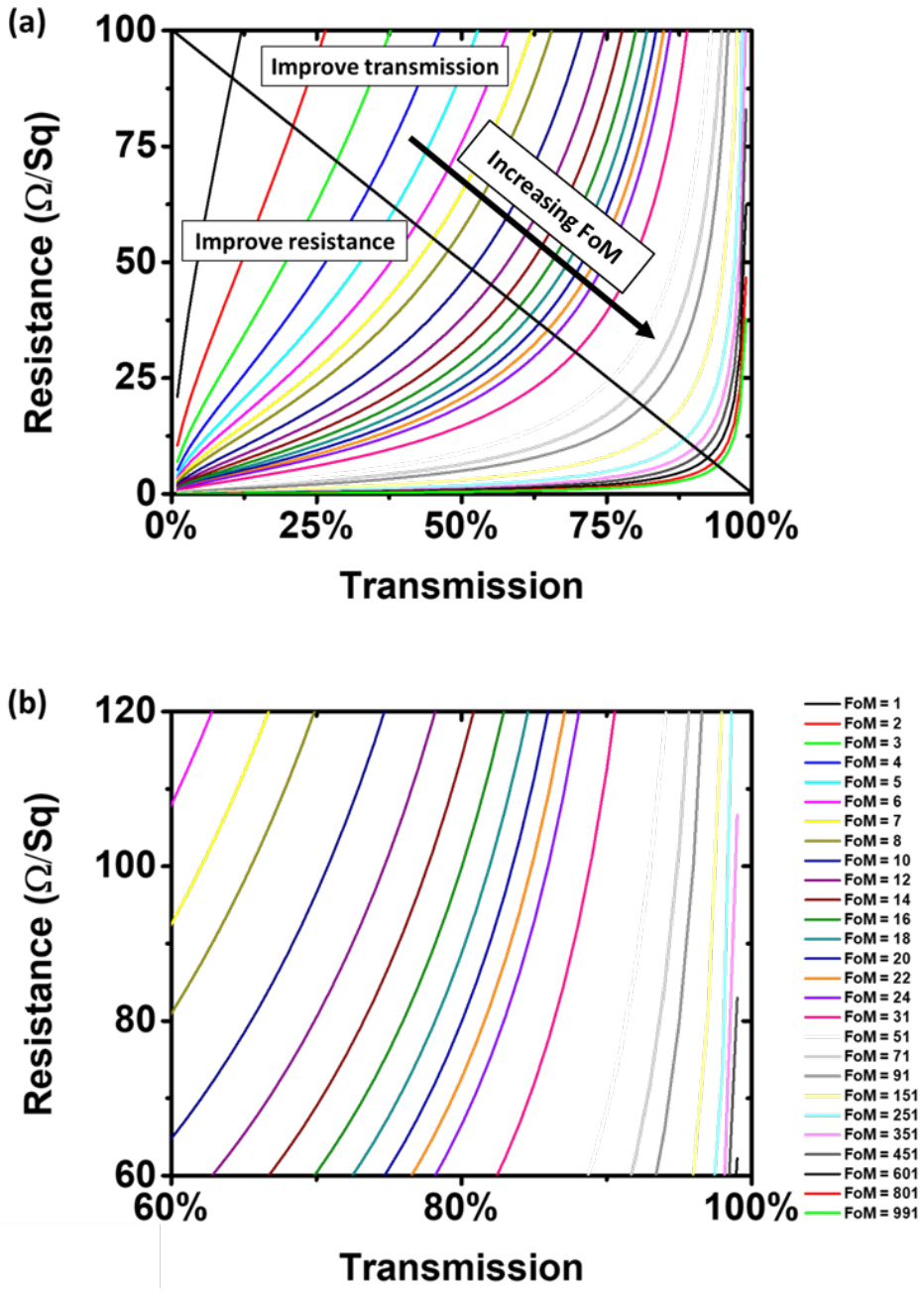

Figure 2.6: **(a)** Sheet resistance vs optical transmittance for various FoMs, the FoMs used were 1 - 25 (interval of 1), 31 - 101 (interval of 10), 151 - 451 (interval of 50), 501 - 1001 (interval of 100). The black line indicates which properties should be improved. **(b)** The same, zoomed in on the region of interest for this work. Improving transmittance is always preferable here.

2.3.3 *Current examples*

2.3.3.1 *Indium tin oxide*

The current industry leading TCE material of choice is ITO.[40] It is the best of materials extensively researched so far. ITO is sputter coated onto a transparent substrate to give a uniformly transparent (approx. 90% for visible light) film, approx. 150 nm thick. The transmittance of ITO is virtually constant across the visible spectrum and there is no optical hazing in the transmittance. When sputtered in this form it can be extremely smooth, with a root mean squared (RMS) roughness of < 1 nm. This, along with its relatively low sheet resistance of between 10 and 100 $\Omega/\square$ at room temperature, makes it an ideal TCE. This also means that it has a σ_{DC}/σ_{Op} figure of 348. Because ITO is sputter coated onto the desired substrate, substrate adhesion is not a concern for manufacturing. ITO is compatible with modern industrial manufacturing techniques such as roll-to-roll for OLED and PV devices.[41]

ITO is not a perfect material, however. Its thickness is not compatible with anything in the 2D material field. At 150 nm thick it is orders of magnitude thicker than a single atom or few-layer sheet. The atomic composition of ITO, with indium and tin, is not environmentally friendly. Both elements must be mined in an expensive and environmentally destructive process. This along with the sputter coat method of fabrication means ITO makes up most of the cost of fabrication of an OLED or PV device. Getting this cost down is critical to making OLED and PV technologies more accessible. Finally for the future of electronic devices academics and industry are looking towards flexible electronics. ITO is not compatible with this vision. Sputter coated ITO on any substrate is highly brittle. It has been extensively shown that ITO cracks and resistance increases significantly when flexed.[42] These issues must be addressed in ITO or it must be replaced by a flexible material if future electronics are to be flexible as envisaged.

2.3.3.2 *Single-Layer Graphene*

When graphene was first discovered many believed it would be the obvious alternative to ITO in modern devices. Its astonishingly high transmittance, low resistance, environmental sustainability and abundance, lack of toxicity, chemical resistance, strength, adhesion to substrates, smoothness, work function, flexibility, and low-cost nature

meant it would replace ITO very fast. When studied closer however, graphene was discovered to have a sheet resistance of between 100 Ω/□ and 1000 Ω/□, or σ_{DC}/σ_{Op} of 161 to 16.1. This sheet resistance is much higher than the 10 Ω/□ seen in commercially available ITO. Its low raw material cost was and still is unattainable. Extremely low yields from mechanical exfoliation, zero transmittance from LPE graphene and high energy cost from CVD are all still issues that need to be overcome, either by reducing cost or enhancing the materials properties to outweigh the cost.

The chemical functionalisation of graphene has seen its sheet resistance and transmittance altered to 30 Ω/□ with 90% transmittance and 125 Ω/□ with 97.7% transmittance, respectively. This means these materials have a $\sigma_{DC}/\sigma_{Op} = 116$ and 129, respectively. Well below the $\sigma_{DC}/\sigma_{Op} = 348$ of ITO. These materials in themselves are not a panacea for flexible applications, however. Neither are stable in air or in many common laboratory solvents required for further processing and device integration. They also do not outperform ITO on sheet resistance. This is particularly important as this figure will affect the overall device efficiency. With most of these materials being designated for portable, low-power devices, low power consumption is of critical importance.

Intercalation of FLG has seen some promise too. FLG has been intercalated with a range of dopants with varying levels of success. Li, K, Rb, Ca and Br have all been used an intercalates in the past. Li has shown extremely low sheet resistance of 3.0 Ω/□. It is also extremely transparent with transmittance of up to 91.7%, giving it a σ_{DC}/σ_{Op} value of 1419.[43] It is extremely unstable in ambient environments, however. It is known to de-intercalate within 48 hours. This makes it inviable for practical applications. Other intercalates have shown similar levels of promise, but with one critical property missing. The exception to all of these is $FeCl_3$ intercalated FLG.

2.3.3.3 *$FeCl_3$-intercalated few-layer graphene*

$FeCl_3$ intercalated FLG, sometimes dubbed GraphExeter and referred to in this thesis as $FeCl_3$-FLG is one of best-known transparent conductors. This is demonstrated clearly in Figure 2.10 when it is compared to other forms of doped graphene mentioned in this work. In this figure, closer to the bottom right corner is better with as low conductivity and as high transmittance as possible. In mechanically exfoliated flakes

$FeCl_3$-FLG has shown sheet resistances as low as 8.8 $\Omega/\square$ with uniform transmittance of 84%.[13] I should note here that no optical hazing has ever been observed in $FeCl_3$-FLG either, whereas other systems such as nanowire based TCEs do suffer from this phenomena.

All of this gives it a $\sigma_{DC}/\sigma_{Op} = 235$. This is on the same order of ITO. In large area Ni grown form it has shown sheet resistances as low as 20 $\Omega/\square$. The stability of $FeCl_3$-FLG is also important for TCE applications if a material is to be useful, in $FeCl_3$-FLG this has been extensively studied. $FeCl_3$-FLG can withstand relative humidity of up to 100% for 25 days, temperatures of up to 150°C in air and 620°C in vacuum.[38] Unlike metallic transparent electrodes no carbon migration has been reported for graphene electrodes in any PV or OLED devices.[41;44]

$FeCl_3$-FLG has been shown once before as a TCE in a fully flexible alternating current electroluminescent (ACEL) device on PET substrate. When compared directly to graphene electrodes the device saw a 49% increase in brightness. This paper also confirmed that $FeCl_3$-FLG is flexible and remains working when flexed.[45]

All of these properties of $FeCl_3$-FLG make it one of the best reported transparent conductors and of huge interest for future device applications. Examining how the material performs in modern OLED and PV devices is important for future technologies. The assessment of $FeCl_3$-FLG in as TCE in PVs has recently taken place, in which I contributed to the material fabrication using the methods developed in this thesis.[46] This thesis will therefore focus on how $FeCl_3$-FLG performs as TCE in OLED devices and how it can be better integrated and understood.

2.4 ORGANIC LIGHT-EMITTING DIODES

2.4.1 *Introduction*

First introduced in 1987 by Tang et al.[47] at Eastman Kodak, an OLED is an light-emitting diode (LED) made up of multiple thin films sandwiched together, this can be visualised in Figure 2.7. Typically, a metal cathode allows for electrons to be injected into an emissive electroluminescent layer. At the same time holes are injected into the device via a transparent anode. When the electron-hole pair recombine in the emissive electroluminescent layer a photon is emitted. This photon leaves the device directly via the transparent anode or is reflected off the metal cathode and leaves the device

via the transparent anode. This device architecture is extremely simple and with the right electroluminescent layer a photon of any wavelength could be emitted.

Having now been developed commercially, OLEDs are now available in mass market devices such as TVs, computer monitors, smartphones, tablets, wearables, handheld games consoles and solid-state lighting. OLED has only just reached this stage and is still very much an emerging technology. It still has fundamental issues such as cost to overcome. It is however one of the best and most likely future dominant display technology for displays of all sizes and use applications. In displays OLED outperforms the industry leading technology, LCD in almost every aspect.[48;49] Because OLEDs are self-illuminating they do not require a thick, expensive, and inefficient always-on backlight. This allows for massive energy savings, with all parts of a display showing black using no power. This also allows for theoretically infinite contrast ratios. For high performance displays too, OLED outperforms LCD. OLED can have a much higher response time and therefore refresh rate than any other modern display technology. This is of significant importance in the lucrative world of media production and gaming. Addressing longer term concerns too, OLED is much more environmentally sustainable, apart from the electrodes, the materials used in OLEDs can all be chosen to be safe for humans and the environment. At this point in time, it looks as if OLED will be the display technology of choice well into the future. Its main potential competitors today are emissive quantum dots, which still haven't left the lab, and microLED, which has yet to be commercialised. The highest efficiency OLED devices demonstrated to date are evaporated in vacuum and are manipulated within an inert atmosphere until they are encapsulated.[50;51] This means the costs of fabrication are still high, and there is much room for improvement.

2.4.2 *Structure*

There are two widely used OLED architectures. The first, where holes are injected through a transparent anode and electrons are injected through a metal cathode is known as a conventional device, with conventional OLED architecture. The second, with the opposite structure, i.e. transparent cathode and metal anode is known as an inverted structure and inverted OLED device. This terminology is important and will be used throughout this thesis.

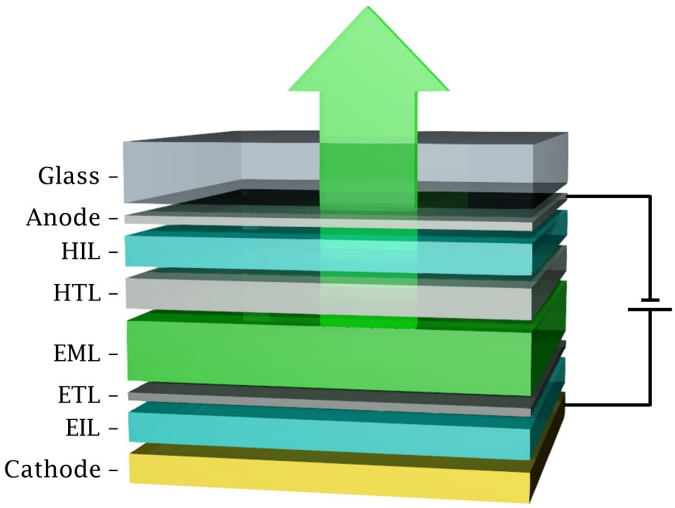

Figure 2.7: The structure of a typical OLED device with hole and electron injection layers (HIL, EIL), and hole and electron transport layers (HTL and ETL), and emissive layer (EML). This device is in its conventional configuration, with transparent anode. Commercially available devices now also contain charge generation layers and interlayers to aid transport. A typical device would be $< 1\mu m$ thick on the substrate.

Because the structure of an OLED device is such that layers of differing materials are sandwiched together it is important that the materials in question are compatible with each other. This means in the fabrication process the deposition of one material cannot destroy the layer below, also one material cannot chemically react with the one directly adjacent. They must also be electrically compatible. This means that electrons or holes from the cathode or anode must be able to seamlessly move into the electroluminescent layer. If either hole transfer or electron transfer is overly preferred recombination my not happen in the electroluminescent layer, leading to zero light output. An ideal device would allow electrons and holes into the electroluminescent layer with no energy barrier to doing so, this can be visualised in Figure 2.8 (a).

Figure 2.8 (b) shows a more realistic device structure. Here a hole transport layer (HTL) or electron blocking layer (EBL) and a electron transport layer (ETL) or hole blocking layer (HBL) has been added. These layers serve to aid the transport of holes and electrons, while blocking electrons and holes, respectively. Looking at the HTL for example, the energy of its lowest unoccupied molecular orbital (LUMO) is higher than that of the emissive layer (EML). This creates an energy barrier to electrons coming

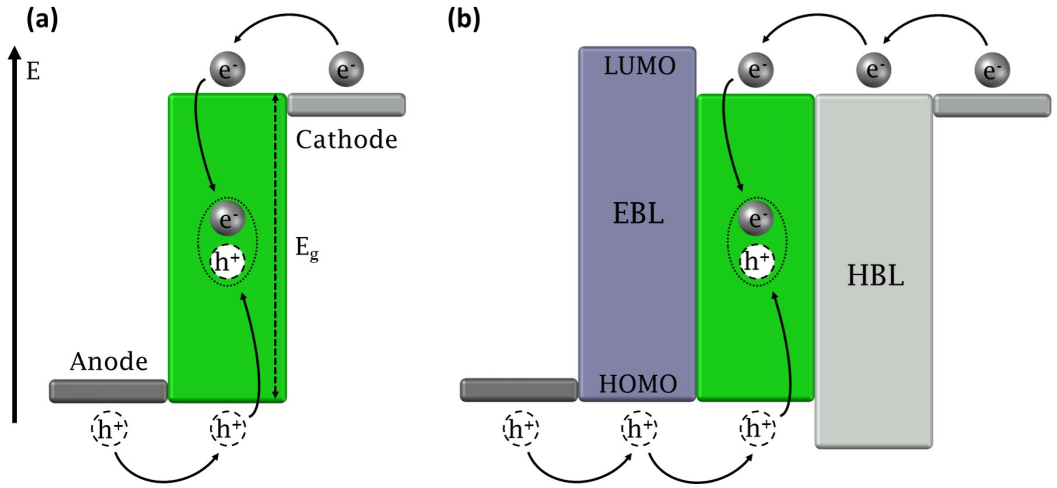

Figure 2.8: **(a)** An ideal OLED band structure. Electrons and holes recombine in the emissive layer (EML) to give out light at the band gap energy E_g. **(b)** A real OLED band structure with hole transport layer (HTL) and electron transport layer (ETL). Here electrons and holes are unable to go from the EML directly to the anode and cathode due to the energy barrier.

from the cathode and prevents them from going directly to the anode, it is energetically more favourable for them to lower their energy by recombining with a hole in the EML. The HTL also can aid transport of holes. If the transport of electrons into the device is low due to mismatched work functions between cathode and EML or electron mobility is low in the cathode the mobility of holes could be seduced to a similar level, this will mean electrons and holes arrive in the EML at the same rate and recombination by radiative decay can be maximised. A similar case can be made for the introduction of the ETL. An ideal device there are no barriers to the injection of holes or electrons, or any difference in mobility of holes or electrons, this is required to achieve a charge balanced device. This can be seen in Figure 2.8 (a).

2.4.3 *OLED operation*

2.4.3.1 *Charge injection*

In an OLED device charges (electrons and holes) are injected via the cathode and anode, respectively. Under an applied voltage bias, they are swept into the LUMO

and highest occupied molecular orbital (HOMO) of the EML. As mentioned before there should be no injection barrier between the electrons and the device to maximise efficiency, nor should there be any difference in charge mobility between charges to ensure a charge balanced device. With this in mind I will look at the work function of electrodes and their adjacent layers in the device.

Considering a conventional device structure throughout, the cathode used in a device should have the highest work function of the materials used. Alkaline earth metals such as calcium with a work function of -2.7 eV - -2.9 eV are often chosen.[52] This can then be encapsulated with an aluminium contact. The high work function is required to match the LUMO of the ETL or electron injection layer (EIL) and allow for efficient electron injection.

In the case of the anode the work function should be as low as possible to match as close as possible the HOMO of the HTL or hole injection layer (HIL). In a conventional device the anode is usually the transparent electrode and so ITO is used almost universally. It has a low work function, which after O_2 plasma treatment can be reduced further to -4.7 eV.[53;54] This work function is generally not low enough however and this why HILs become a necessity for an efficient device. ITO could easily be replaced with another transparent conductor in conventional devices if an alternative with lower sheet resistance, better transmittance and lower work function was found. $FeCl_3$-FLG is a great candidate for this as it has all these properties (a work function of -5.0 - 5.5 eV), with the advantage of having mechanical flexibility.

The reasons for replacing metallic electrodes with graphene in OLED devices are extensive. As described in the previous sections graphene has low resistivity, high optical transmittance, is bendable and stretchable, and has high chemical stability and robustness. An important property of graphene is that its Fermi energy can be shifted, and its work function engineered through chemical doping[55]. Thus, using graphene electrodes the electrode work function can be tuned according to the type of carrier needed to minimise the contact resistance, to reduce the operating voltages and, most importantly, to achieve efficient injection of both charge carriers, necessary for high efficiency light emission. The attractiveness of graphene arises also from its low fabrication cost. Currently, precious metals like gold are needed to achieve the injection of holes into the transistor channel because the HOMO level of many organic semiconductors is in the range of 4.8 to 5.3 eV, which aligns well with the work function

of gold (4.8-5.1 eV). However, such metals are expensive, and their deposition processes require high-cost equipment. Graphene can be fabricated on wafer scale by lower-cost methods using solution-processing[17] or chemical vapour deposition[23]. Furthermore, graphene can be grown at temperatures as low as 60°C[56], which are ideal for growing it directly on flexible substrates.

It has recently been shown however that work function matching is less important than previously thought. With clever layer structures in the form of charge generation layers, it has been shown that efficient OLED devices can be fabricated regardless of electrode work function. This may allow for more materials to be used as electrodes as, conductivity and transmittance and not work function will be the driving parameters.[57]

2.4.3.2 *Charge transport*

When charges have been injected into a device they must then be transported to the EML and towards an opposite charge to form an exciton. For the most efficient device charge transport must be as easy as possible, and ideally matched on the cathode and anode sides of the device. The charge transport in the device is controlled by the charge mobility. The devices I will study are all polymer OLEDs and as such the charge mobilities will be several orders of magnitude lower than inorganic semiconducting crystals. These polymers have very high degrees of structural and energetic disorders. These disorders arise naturally from the orientation and position of long polymer chains, differing conjugation lengths and variations of the dielectric environment throughout the material. These disorders result in a much lower charge carrier mobility than what would be seen in a crystalline lattice. All of these disorders mean that the charge transport mechanism is extremely complex but can be said to be dominated by incoherent and thermally activated charge carrier hopping between molecules and between segments of the same molecule. As a result, models to describe charge transport in these polymers are all related to the trapping and detrapping mechanisms that occur. These mechanisms are all temperature and electric field dependant.

It is possible to obtain the charge carrier mobility from the current-voltage curve of single-carrier devices. Semiconducting polymers should have a low carrier mobility. The highest reported are only 0.01 cm^2/Vs, typical inorganic semiconductors have charge carrier mobilities commonly around 10^5 cm^2/Vs.[58;59] When a suitably high elec-

tric field is applied to a device the charge injection will become Ohmic. This happens if there is no energy barrier in the device or the field is high enough to overwhelm it. In this regime the current will be limited only by the charge carrier mobility. If the carrier mobilities are low this will indicate that charges are accumulating inside the polymer. This accumulation will induce an internal electric field which can cancel out the external electric field at the injection point. Now the regime has changed, current is now limited by the space charge in the polymer, this effect is known as space charge limited current (SCLC) which can be described by the following:

$$J_{SCL} = \frac{9}{8}\epsilon_r\epsilon_0\mu\frac{V^2}{t^3} \tag{2.12}$$

where J_{SCL} is the SCLC, ϵ_r is the dielectric permittivity of the polymer, ϵ_0 is the permittivity of free space, μ is the charge carrier mobility, V is the voltage applied to the device and t is the thickness of the polymer film. This is known as the Mott Gurney law. This is a simple model that doesn't take charge traps or bipolar current into consideration, however it has been used before in various studies to good effect and allows for a good experimental approximation of the charge carrier mobility.[60–62]

2.4.3.3 *Charge recombination*

In order to emit light, the electron-hole pair, bound as an exciton must relax to emit a photon. This must happen in the EML. According to spin statistics, every fourth exciton is a singlet, the rest are triplets. Only singlet excitons decay radiatively, they emit light at a wavelength defined by the band gap of the EML. It should be noted that for conjugated polymer chains the fraction of singlet excitons can be higher than one fourth ($> 50\%$) meaning theoretically >25% internal device efficiency is possible.[63;64] Several mechanisms for achieving this have been proposed, most focus on taking advantage of the 75% triplet states. These are triplet-triplet annihilation (TTA), this mechanism increases the efficiency by converting triplet excitons into singlets,[65] thermally activated delayed fluorescence (TADF) materials where triplets can be exchanged to singlets,[66] and more traditionally phosphorescent dopants from heavy-metal complexes to extract both the singlet and triplet excitons as light.[67] It should also be noted that singlet excitons do not have to decay radiatively, they can decay non-radiatively as well.

An exciton can be created in the EML of an OLED device via the absorption of

a photon or the capture of a pair of oppositely charged charges. This results in the formation of a Coulombically bound electron-hole pair. Because of a strong electron-phonon coupling in the organic polymer there is a strong carrier localisation, this means the excited electron cannot escape the attraction between itself and the hole and so an exciton is formed. The exciton can relax back to the ground state in one of three ways: 1. radiative decay (light emitting), 2. internal conversion, where the singlet state converts to a triplet and decays, possibly via phosphorescence and 3. non-radiative decay. The ideal device would only decay radiatively via the singlet state.

Organic polymers like the ones I have been describing have a low mobility and as such the electron-hole recombination can be described by the Langevin recombination model, here the recombination rate is dominated by charge diffusion. Very simply, for recombination to occur, the Coulombic attraction between the electron-hole pair must be larger than the thermal energy driving them apart. This is expressed as follows

$$kT = \frac{e^2}{4\pi\epsilon_r\epsilon_0 r_c} \tag{2.13}$$

where e is the unit of charge and r_c is the capture radius. At room temperature this equation shows $r_c \approx 14\ nm$. This is much larger than the mean hopping distance of 1 nm and so it is assumed that this theory can adequately describe the system.[68] This now means that, the recombination rate is given by Langevin theory and can be expressed as

$$R = \frac{e(\mu_e + \mu_h)}{\epsilon_r\epsilon_0} n_e n_h \tag{2.14}$$

where R is the recombination rate of electron-hole pairs, μ_e and μ_h are the electron and hole mobilities, and n_e and n_h are the electron and hole densities.[52] This equation shows that the recombination rates are governed by the electron-hole mobilities and densities. For maximum efficiency there must be the same number and mobility of electrons and holes. If the charge mobilities are very different it is clear that, the luminance efficiency will be limited by the charge with lower mobility and the current will be limited by the charge with the higher mobility.[52] This will result in recombination occurring closer to the side of the device with lower mobility.[69] This can then lead to exciton quenching at the EML surface. Therefore, recombination is required to occur as much as possible in the middle of the EML.

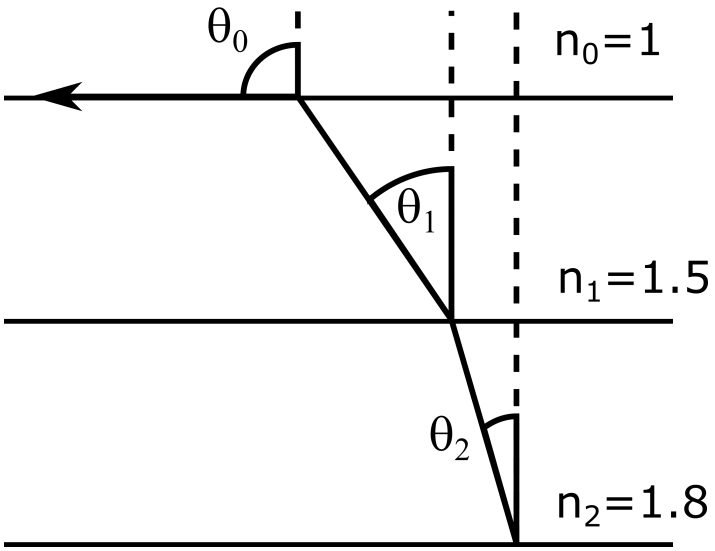

Figure 2.9: Materials of reducing refractive index can mean not all light can escape an OLED. An EML with refractive index of 1.8 will only allow light emitted at $< 34°$ out of the device.

2.4.3.4 *Outcoupling*

The last step in the process of light emission requires us to examine how effectively light will escape the device. The device described so far will be composed of multiple layers. The photon emitted from the EML must travel out of the EML, through the HTL and or HIL, through the transparent electrode and finally through the substrate. If any of these layers block the photon the device will not emit light, it is important to ensure any gains made by adding charge transport layers are not offset by the reduced ability of the photon to exit the device. When considering transparent materials, the biggest loss mechanism is going to be the mismatch of refractive indices between layers resulting a large number of photons undergoing total internal reflection (TIR). The materials which require photons to escape from are the EML polymer which has a refractive index in the range 1.6-2.0, ITO in a similar range and glass with an index of 1.5. Considering the polymer in direct contact with the air where it is assumed that the polymer has a refractive index of ≈ 1.8 then the critical angle is equal to 34°. This is derived from Snell's law Equation 2.15 and implies that only light emitted within

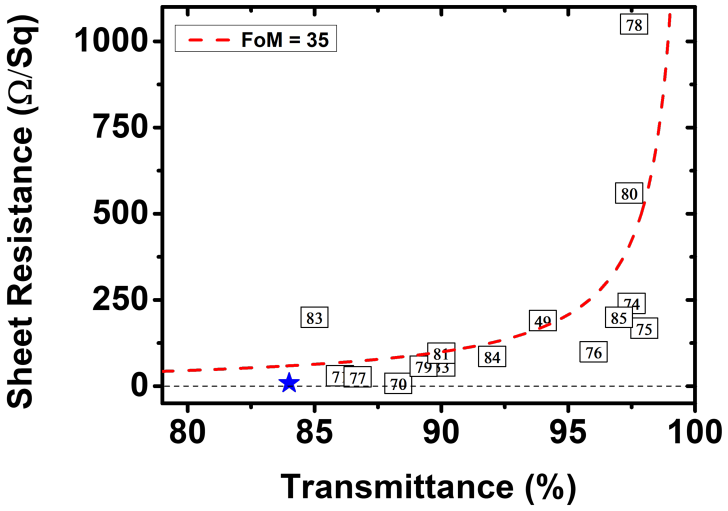

Figure 2.10: Sheet resistance vs transmittance at 550 nm for a number of different transparent electrode candidates. $FeCl_3$-FLG is highlighted with a blue star. Materials with higher FoM are closer to the bottom right corner. The FoM = 35 line is calculated from Equation 2.11

34° of the normal will be emitted. This can be visualised in Figure 2.9.

$$\Theta_c = sin^{-1}\left(\frac{n_0}{n_1}\right) \tag{2.15}$$

Assuming the light emission is in a Lambertian profile, by limiting light out to only that which is in the 34°, the total emission is limited to just 56%, and assuming just singlet emission this limits overall external quantum efficiency (EQE) to a maximum of just 14%. This demonstrates the importance of using polymers with low refractive index and ensuring no material with high refractive index is introduced into the device.

2.5 RECENT DEVELOPMENTS OF GRAPHENE-BASED TCES IN OLEDS

This work investigates $FeCl_3$-FLG, its properties as they relate to OLEDs, how and if the material can be integrated into them, and what is the resulting performance compared to ITO for a range of substrates, both rigid and flexible.

It is important when conducting any investigation to know what has been done

before. This section will look at all forms of graphene-based TCEs that have been integrated into OLED devices. I will assess their material properties as well as the device properties with the material integrated. I will also look at the drawbacks associated with them and discuss why have they have not progressed onto commercialisation.

In Table 2.1 I have put together a non-exhaustive list of some of the materials that have been used as TCE in OLEDs before. Here I have attempted to summarise their material properties, and device properties as reported. One important factor to note is that not all OLEDs use the same device architecture, so these properties are not necessarily comparable. This table has been converted into Figure 2.10 which shows the line where FoM = 35, the minimum properties a TCE requires to be considered viable.

Looking at the FoM values for the TCEs presented in Table 2.1 and comparing them to some of the key metrics for OLED performance, what is striking is that there is no clear correlation. It is expected that there should be a direct correlation between electrode performance and overall device performance. Having discussed FoM previously, this is a good metric for electrode performance. When looking at assessing device performance focus should be on current efficiency (CE) and EQE. There is no correlation between the reported FoMs and the reported CEs and EQEs. This does not indicate that TCE properties play no role in device performance, rather there are many factors at play, all of which can be chosen to gain additional properties while sacrificing efficiency. In the case of this work the objectives are to fabricate an OLED which is solution processed, at low temperature, using low-cost laboratory techniques, which result in a flexible, indium-free device.

Looking at the material properties of graphene-based TCEs it is clear that Ag-NWs rise to the top in terms of FoM. The highest FoM here is that reported by Dong at al[70]. They achieve an FoM of 364, which is well able to compete with that of ITO. Their reported R_S and T are both in the range typically seen for ITO. What is particularly notable is that these results were based on a polyethylene terephthalate (PET) substrate. When these devices were compared to the same with ITO anodes, the graphene-based devices showed a 5% increase in power efficiency (PE). It should be noted that superior performance was expected with roughness and encapsulation optimisation of the electrode. One significant drawback with using any nanowire electrode is the introduction of optical haze, which cannot be removed. The slight increase in

PE means this material will need to show significantly better performance compared to ITO to be a viable replacement.

Another viable and impressive candidate is that reported by Han et al.[33] Here 4-layer graphene was modified by chemical doping with HNO_3, before a polymetric gradient HIL was put on top. This creates a gradiented work function, effectively moving the work function of the anode to 6 eV. The devices fabricated using this electrode showed remarkable efficiency, a single device showed an EQE of 32.7%, while a tandem device, with hemispherical lens showed 87.3% EQE. The same devices on PET showed similar numbers and were able to maintain constant current after 1000 bending cycles around a 7.5 mm radius. This work represents some of the best performing graphene-based OLEDs demonstrated to date. There are significant problems with this approach however in terms of stability. The stability of the HNO_3 doped material is a problem, along with the long-term stability of the polymer blend based on poly(3,4-ethylenedioxythiophene) polystyrene sulfonate (PEDOT:PSS).

One of the materials used in this thesis, MoO_3, has also been used to p-dope graphene.[71] The doped graphene produced showed a sheet resistance of 30 $\Omega/\square$ at 86% transmittance, giving a FoM of 80. This is high, and within the minimum threshold for OLEDs.[39] Despite similar turn-on voltages these electrodes when compared in devices to ITO showed higher CE for SLG and 3-layer based devices. At 1000 cd/m^2 the 3-layer graphene-based OLED showed a CE of 67 cd/A. One of the primary issues with this electrode is its stability in air. MoO_3 is highly unstable in the presence of oxygen, all processing is done in inert environments, this is a significant added cost in processing and encapsulation, and without significant performance improvements over ITO it will not be commercially viable.

Another material worth mentioning, although it is not graphene-based is the thin film material known as MXene. MXenes are 2D transition metal carbides with the formula $M_{n+1}X_n$, where M is a transition mental and X is carbon or nitrogen.[72] Recently an OLED was fabricated with the MXexe Ti_3C_2 as the TCE.[73] It had a sheet resistance of 108 $\Omega/\square$, transmittance of 85% (FoM = 21), work function of 5.1 eV, and could withstand 5000 bending cycles with no change in resistance. When integrated into an OLED it showed an EQE of 28.5%, very close to that of ITO. This MXene is not stable in ambient conditions, but this is the first MXene to be integrated into an OLED. In that context these results are impressive, and MXexes will be a TCE to

watch in the near future.

One material class with great future potential is that of transfer-free graphene. Recently work has been done showing CVD graphene grown on sapphire, without the need for a metal growth substrate. This also eliminates the need for transfer, cutting out a significant contamination step. The graphene grown showed a sheet resistance of 2.2 $K\Omega/\square$ (450 $\Omega/\square$ when HNO_3 doped) and transmittance of 97%.[28] This study shows the possibility of transfer-free graphene, cutting cost and contaminants, while the sheet resistance is currently very high, it could be significantly reduced in future with a more refined process. This could allow for a graphene-based OLED with a significant performance advantage over transferred graphene.

Finally, I will look at flexible boron-doped graphene.[74] Despite higher than usual sheet resistance at 240 $\Omega/\square$, the FoM of this material is very high, at 62. This is due to the single-layer nature of the material, giving it transmittance of 97.9%. Significantly the work function is also deepened to -5.0 eV. This boron-doped material has also shown its ability to bend around a 0.75 mm radius over 3000 times with little change in resistance. In a working OLED the material helped devices achieve up to 24.6% EQE along with a CE of 99.7 lm/W. This slightly outperformed the reference ITO electrode at 22.8% and 89.1 lm/W. The stability of this material is not reported, however bulk boron has good stability. This likely represents the best form of graphene for TCE applications seen to date.

The final highly stable,[38] low resistance[13] form of functionalised graphene that needs to be investigated is $FeCl_3$-FLG. That is the subject of this work.

Table 2.1: Recent developments of graphene-based TCEs in OLEDs, a selection of 20 are shown here. All of the graphene here is CVD grown. Devices are all single-unit without out-coupling structures unless stated. The graphene is used as transparent cathode in all devices.

TCE	Substrate	R_S ($\Omega/\square$)	T (%)	FoM	Φ (eV)	L (cd/m^2)	CE (cd/A)	PE (lm/W)	EQE (%)	Ref
SLG HTB doped	PET	168	98	111	5.3		111.4 (max)	124.9 (max)	29.7	[75]
SLG/CNT /AuNP	Glass	100	96	91		650	2.1			[76]
SLG/AgNWs	PET	27	86.7	94	5.1	15000 at 9 V				[77]
SLG	Glass	1050	97.6	15		39100	74.5	26.6	20.7	[78]
3LG/AuNP	Glass	57.96	89.3	56		10000 at 8.4 V	56.42		16.4	[79]
2LG MoO_3 doped	SU-8/NOA63	190	94	32		5000	31.4		20	[49]
SLG boron doped	PET	240	97.5	62	5		95.4 (max)	99.7 (max)	24.6 (max)	[74]
SLG	PET	560	97.4	25		10000	89.7 (max)	102.6		[80]
SLG/AgNWs/PC	PET	8.06	88.3	364		4297 at 13 V	2.11 (max)			[70]
4LG HNO_3 doped	Glass	81.3	90	43		10000	120.8 (max)		32.7 (max)	[33]
4LG HNO_3 doped (tandem)	PET	58.3	90	60			205.9 (max)		45.2 (max)	[33]
TiO_2/SLG/GraHIL	Glass	95.5	90	36		500 at 5 V	168.4	160.3	40.8	[81]
SLG WO_3 doped	Glass	300			4.6	1000		62		[82]
SLG-fluoropolymer	Glass	200	85	11	4.7		7.91			[83]
SLG MoO_3 doped	Glass	30	86	80		1000	55 (SLG)	34		[71]
SLG/TiO_x/PEDOT:PSS	Glass	86	92	51	5.12	1000	10.11	5.41		[84]
SLG OA doped	PET	200	97	61		10000 at 5 V	80		9.4	[85]
4LG $AuCl_3$ doped	PET	30			5.95		27.4 (max)	28.1 (max)	15.6	[86]
4LG NHO_3 doped	PET	54			4.6		30.2 (max)	37.2 (max)		[86]
$FeCl_3$-FLG	**Glass**	**110**	**76**	**12**	**5.0 - 5.5**	**1256 at 7.5 V**	**0.31**	**0.15**	**0.09**	**This work**

R_S, sheet resistance; T, transmittance at 550 nm; FoM, figure of merit; Φ, work function; L, luminance; CE, current efficiency; PE, power efficiency; EQE, external quantum efficiency

CNT, carbon nanotube; NP, nanoparticle; NW, nanowire; PC, polycarbonate; GraHIL, polymer blend [33]; OA, triethyloxonium hexachloroantimonate/dichloroethene

BIBLIOGRAPHY

[1] H. P. Boehm, R. Setton, and E. Stumpp. Nomenclature and terminology of graphite intercalation compounds. *Carbon*, 24(2):241–245, 1 1986.

[2] P. R. Wallace. The band theory of graphite. *Physical Review*, 71(9):622–634, 5 1947.

[3] K S Novoselov, A K Geim, S V Morozov, D Jiang, Y Zhang, S V Dubonos, I V Grigorieva, and A A Firsov. Electric field in atomically thin carbon films. *Science*, 306(5696):666–669, 10 2004.

[4] L. D. Landau. Zur Th eorie der phasenumwandlungen II. *Phys. Z. Sowjetunion*, 11:26–35, 1937.

[5] R. Peierls. Quelques propriétés typiques des corps solides. *Annales de l'I.H.P.*, 5(3):177–222, 1935.

[6] J. Krumhansl and H. Brooks. The lattice vibration specific heat of graphite. *The Journal of Chemical Physics*, 21(10):1663–1669, 10 1953.

[7] J. C. Bowman and J. A. Krumhansl. The low-temperature specific heat of graphite. *Journal of Physics and Chemistry of Solids*, 6(4):367–379, 9 1958.

[8] Xuekun Lu, Minfeng Yu, Hui Huang, and Rodney S Ruoff. Tailoring graphite with the goal of achieving single sheets. *Nanotechnology*, 10(3):269–272, 9 1999.

[9] Yuanbo Zhang, Joshua P. Small, William V. Pontius, and Philip Kim. Fabrication and electric-field-dependent transport measurements of mesoscopic graphite devices. *Applied Physics Letters*, 86(7):1–3, 2 2005.

[10] A. H. Castro Neto, F. Guinea, N. M.R. Peres, K. S. Novoselov, and A. K. Geim. The electronic properties of graphene. *Reviews of Modern Physics*, 81(1):109–162, 1 2009.

[11] Kin Fai Mak, Matthew Y. Sfeir, James A. Misewich, and Tony F. Heinza. The evolution of electronic structure in few-layer graphene revealed by optical spectroscopy. In *Proceedings of the National Academy of Sciences of the United States of America*, volume 107, pages 14999–15004, 8 2010.

[12] Mikito Koshino and Tsuneya Ando. Orbital diamagnetism in multilayer graphenes: Systematic study with the effective mass approximation. *Physical Review B - Condensed Matter and Materials Physics*, 76(8):085425, 8 2007.

[13] Ivan Khrapach, Freddie Withers, Thomas H. Bointon, Dmitry K. Polyushkin, William L. Barnes, Saverio Russo, and Monica F. Craciun. Novel highly conductive and transparent graphene-based conductors. *Advanced Materials*, 24(21):2844–2849, 6 2012.

[14] Weijie Zhao, Ping Heng Tan, Jian Liu, and Andrea C Ferrari. Intercalation of few-layer graphite flakes with FeCl3: Raman determination of Fermi level, layer by layer decoupling, and stability. *Journal of the American Chemical Society*, 133(15):5941–5946, 2011.

[15] Mikhail I Katsnelson. Graphene: carbon in two dimensions. *Materials Today*, 10(1-2):20–27, 1 2007.

[16] Laura Barrutia, Efraín Ochoa-Martínez, Mercedes Gabás, Alba Centeno, Amaia Zurutuza, Ignacio Rey-Stolle, and Carlos Algora. Evidence of Decreased Optical Absorption of Chemical Vapor Deposition Graphene Multilayers Deposited on Semiconductor Structures. *ACS Photonics*, page acsphotonics.1c01551, 2 2022.

[17] Yenny Hernandez, Valeria Nicolosi, Mustafa Lotya, Fiona M. Blighe, Zhenyu Sun, Sukanta De, I. T. McGovern, Brendan Holland, Michele Byrne, Yurii K. Gun'ko, John J. Boland, Peter Niraj, Georg Duesberg, Satheesh Krishnamurthy, Robbie Goodhue, John Hutchison, Vittorio Scardaci, Andrea C. Ferrari, and Jonathan N. Coleman. High-yield production of graphene by liquid-phase exfoliation of graphite. *Nature Nanotechnology*, 3(9):563–568, 9 2008.

[18] Jonathan N Coleman. Liquid exfoliation of defect-free graphene. *Accounts of Chemical Research*, 46(1):14–22, 1 2013.

[19] Keith R. Paton, Eswaraiah Varrla, Claudia Backes, Ronan J. Smith, Umar Khan, Arlene O'Neill, Conor Boland, Mustafa Lotya, Oana M. Istrate, Paul King, Tom Higgins, Sebastian Barwich, Peter May, Pawel Puczkarski, Iftikhar Ahmed, Matthias Moebius, Henrik Pettersson, Edmund Long, João Coelho, Sean E. O'Brien, Eva K. McGuire, Beatriz Mendoza Sanchez, Georg S. Duesberg, Niall McEvoy, Timothy J. Pennycook, Clive Downing, Alison Crossley, Valeria Nicolosi, and Jonathan N. Coleman. Scalable production of large quantities of defect-free few-layer graphene by shear exfoliation in liquids. *Nature Materials*, 13(6):624–630, 6 2014.

[20] Jonathan N Coleman, Mustafa Lotya, Arlene O'Neill, Shane D Bergin, Paul J King, Umar Khan, Karen Young, Alexandre Gaucher, Sukanta De, Ronan J Smith, Igor V Shvets, Sunil K Arora, George Stanton, Hye Young Kim, Kangho Lee, Gyu Tae Kim, Georg S Duesberg, Toby Hallam, John J Boland, Jing Jing Wang, John F Donegan, Jaime C Grunlan, Gregory Moriarty, Aleksey Shmeliov, Rebecca J Nicholls, James M Perkins, Eleanor M Grieveson, Koenraad Theuwissen, David W. McComb, Peter D Nellist, and Valeria Nicolosi. Two-dimensional nanosheets produced by liquid exfoliation of layered materials. *Science*, 331(6017):568–571, 2011.

[21] Valeria Nicolosi, Manish Chhowalla, Mercouri G. Kanatzidis, Michael S. Strano, and Jonathan N. Coleman. Liquid exfoliation of layered materials. *Science*, 340(6139):1226419–1226419, 6 2013.

[22] Luca Banszerus, Michael Schmitz, Stephan Engels, Jan Dauber, Martin Oellers, Federica Haupt, Kenji Watanabe, Takashi Taniguchi, Bernd Beschoten, and Christoph Stampfer. Ultrahigh-mobility graphene devices from chemical vapor deposition on reusable copper. *Science Advances*, 1(6):e1500222, 7 2015.

[23] Xuesong Li, Weiwei Cai, Jinho An, Seyoung Kim, Junghyo Nah, Dongxing Yang, Richard Piner, Aruna Velamakanni, Inhwa Jung, Emanuel Tutuc, Sanjay K Banerjee, Luigi Colombo, and Rodney S Ruoff. Large-area synthesis of high-quality and uniform graphene films on copper foils. *Science*, 324(5932):1312–1314, 6 2009.

[24] Alfonso Reina, Xiaoting Jia, John Ho, Daniel Nezich, Hyungbin Son, Vladimir Bulovic, Mildred S Dresselhaus, and Kong Jing. Large area, few-layer graphene films on arbitrary substrates by chemical vapor deposition. *Nano Letters*, 9(1):30–35, 2009.

[25] Maria Losurdo, Maria Michela Giangregorio, Pio Capezzuto, and Giovanni Bruno. Graphene CVD growth on copper and nickel: Role of hydrogen in kinetics and structure. *Physical Chemistry Chemical Physics*, 13(46):20836–20843, 11 2011.

[26] Yi Zhang, Luyao Zhang, and Chongwu Zhou. Review of Chemical Vapor Deposition of Graphene and Related Applications. *Accounts of Chemical Research*, 46(10):2329–2339, 2013.

[27] Roberto Muñoz and Cristina Gómez-Aleixandre. Review of CVD synthesis of graphene. *Chemical Vapor Deposition*, 19(10-12):297–322, 12 2013.

[28] Zhichao Weng, Sebastian C. Dixon, Lok Yi Lee, Colin J. Humphreys, Ivor Guiney, Oliver Fenwick, and William P. Gillin. Wafer-Scale Graphene Anodes Replace Indium Tin Oxide in Organic Light-Emitting Diodes. *Advanced Optical Materials*, 10(3):2101675, 2 2022.

[29] M F Craciun, I Khrapach, M D Barnes, and S Russo. Properties and applications of chemically functionalized graphene. *Journal of Physics Condensed Matter*, 25(42):423201, 10 2013.

[30] Hoik Lee, Keewook Paeng, and Ick Soo Kim. A review of doping modulation in graphene. *Synthetic Metals*, 244:36–47, 10 2018.

[31] Mohamed S.A. Abdou and Steven Holdcroft. Oxidation of π-conjugated polymers with gold trichloride: enhanced stability of the electronically conducting state and electroless deposition of Au0. *Synthetic Metals*, 60(2):93–96, 9 1993.

[32] Ki Kang Kim, Alfonso Reina, Yumeng Shi, Hyesung Park, Lain Jong Li, Young Hee Lee, and Jing Kong. Enhancing the conductivity of transparent graphene films via doping. *Nanotechnology*, 21(28):285205, 7 2010.

[33] Tae Hee Han, Min Ho Park, Sung Joo Kwon, Sang Hoon Bae, Hong Kyu Seo, Himchan Cho, Jong Hyun Ahn, and Tae Woo Lee. Approaching ultimate flexible organic light-emitting diodes using a graphene anode. *NPG Asia Materials*, 8(9), 2016.

[34] M. S. Dresselhaus and G. Dresselhaus. Intercalation compounds of graphite. *Advances in Physics*, 51(1):1–186, 1 2002.

[35] C. A. Howard, M. P.M. Dean, and F. Withers. Phonons in potassium-doped graphene: The effects of electron-phonon interactions, dimensionality, and adatom ordering. *Physical Review B - Condensed Matter and Materials Physics*, 84(24):241404, 12 2011.

[36] Naeyoung Jung, Bumjung Kim, Andrew C. Crowther, Namdong Kim, Colin Nuckolls, and Louis Brus. Optical reflectivity and Raman scattering in few-layer-thick graphene highly doped by K and Rb. In *ACS Nano*, volume 5, pages 5708–5716. American Chemical Society, 7 2011.

[37] Priyamvada Jadaun, Hema C.P. Movva, Leonard F. Register, and Sanjay K. Banerjee. Theory and synthesis of bilayer graphene intercalated with ICl and IBr for low power device applications. *Journal of Applied Physics*, 114(6):063702, 8 2013.

[38] Dominique Joseph Wehenkel, Thomas Hardisty Bointon, Tim Booth, Peter Bøggild, Monica Felicia Craciun, and Saverio Russo. Unforeseen high temperature and humidity stability of FeCl3 intercalated few layer graphene. *Scientific Reports*, 5(1):7609, 7 2015.

[39] Sukanta De and Jonathan N. Coleman. Are there fundamental limitations on the sheet resistance and transmittance of thin graphene films? *ACS Nano*, 4(5):2713–2720, 5 2010.

[40] Michael Hengge, Konstantin Livanov, Natalia Zamoshchik, Felix Hermerschmidt, and Emil J.W. List-Kratochvil. ITO-free OLEDs utilizing inkjet-printed and low temperature plasma-sintered Ag electrodes. *Flexible and Printed Electronics*, 6(1):015009, 2 2021.

[41] Khalid Alzoubi, Mohammad M. Hamasha, Susan Lu, and Bahgat Sammakia. Bending fa-

tigue study of sputtered ITO on flexible substrate. *IEEE/OSA Journal of Display Technology*, 7(11):593–600, 11 2011.

[42] Zhong Chen, Brian Cotterell, and Wei Wang. The fracture of brittle thin films on compliant substrates in flexible displays. *Engineering Fracture Mechanics*, 69(5):597–603, 3 2002.

[43] Wenzhong Bao, Jiayu Wan, Xiaogang Han, Xinghan Cai, Hongli Zhu, Dohun Kim, Dakang Ma, Yunlu Xu, Jeremy N Munday, H Dennis Drew, Michael S Fuhrer, and Liangbing Hu. Approaching the limits of transparency and conductivity in graphitic materials through lithium intercalation. *Nature Communications*, 5(1):4224, 2014.

[44] S. T. Lee, Z. Q. Gao, and L. S. Hung. Metal diffusion from electrodes in organic light-emitting diodes. *Applied Physics Letters*, 75(10):1404–1406, 8 1999.

[45] Elias Torres Alonso, George Karkera, Gareth F Jones, Monica F Craciun, and Saverio Russo. Homogeneously Bright, Flexible, and Foldable Lighting Devices with Functionalized Graphene Electrodes. *ACS Applied Materials and Interfaces*, 8(26):16541–16545, 2016.

[46] Kieran K. Walsh, Conor Murphy, Saverio Russo, and Monica F. Craciun. Improved Stability of Organic Photovotlaic Devices With FeCl3 Intercalated Graphene Electrodes. *Frontiers in Electronics*, 2:2, 4 2021.

[47] C. W. Tang and S. A. Vanslyke. Organic electroluminescent diodes. *Applied Physics Letters*, 51(12):913–915, 9 1987.

[48] David Barnes. LCD or OLED: Who wins? *Digest of Technical Papers - SID International Symposium*, 44(1):26–27, 6 2013.

[49] Hai Wei Chen, Jiun Haw Lee, Bo Yen Lin, Stanley Chen, and Shin Tson Wu. Liquid crystal display and organic light-emitting diode display: present status and future perspectives. *Light: Science and Applications*, 7(3):17168, 2018.

[50] Organic light emitting diode (OLED) - Materize.

[51] Bhrijesh N Patel and Mrugesh M Prajapati. OLED: A Modern Display Technology. *International Journal of Scientific and Research Publications*, 4(1):2250–3153, 2014.

[52] N. K. Patel, S. Ciná, and J. H. Burroughes. High-efficiency organic light-emitting diodes. *IEEE Journal on Selected Topics in Quantum Electronics*, 8(2):346–361, 2002.

[53] C. C. Wu, C. I. Wu, J. C. Sturm, and A. Kahn. Surface modification of indium tin oxide by plasma treatment: An effective method to improve the efficiency, brightness, and reliability of organic light emitting devices. *Applied Physics Letters*, 70(11):1348–1350, 6 1997.

[54] D. J. Milliron, I. G. Hill, C. Shen, A. Kahn, and J. Schwartz. Surface oxidation activates indium tin oxide for hole injection. *Journal of Applied Physics*, 87(1):572–576, 12 2000.

[55] Yumeng Shi, Ki Kang Kim, Alfonso Reina, Mario Hofmann, Lain Jong Li, and Jing Kong. Work function engineering of graphene electrode via chemical doping. *ACS Nano*, 4(5):2689–2694, 5 2010.

[56] Jinsung Kwak, Jae Hwan Chu, Jae Kyung Choi, Soon Dong Park, Heungseok Go, Sung Youb Kim, Kibog Park, Sung Dae Kim, Young Woon Kim, Euijoon Yoon, Suneel Kodambaka, and

Soon Yong Kwon. Near room-temperature synthesis of transfer-free graphene films. *Nature Communications*, 3(1):645, 1 2012.

[57] Yong Hua Chen, Dong Ge Ma, Heng Da Sun, Jiang Shan Chen, Qing Xun Guo, Qiang Wang, and Yong Biao Zhao. Organic semiconductor heterojunctions: Electrode-independent charge injectors for high-performance organic light-emitting diodes. *Light: Science and Applications*, 5(3):e16042–e16042, 3 2016.

[58] Zhenan Bao, Ananth Dodabalapur, and Andrew J. Lovinger. Soluble and processable regioregular poly(3-hexylthiophene) for thin film field-effect transistor applications with high mobility. *Applied Physics Letters*, 69(26):4108–4110, 8 1996.

[59] Sze. *Physics of Semiconductor Devices Physics of Semiconductor Devices*, volume 10. 1995.

[60] C. Tanase, E. J. Meijer, P. W.M. Blom, and D. M. de Leeuw. Unification of the hole transport in polymeric field-effect transistors and light-emitting diodes. *Physical Review Letters*, 91(21):216601, 11 2003.

[61] H. C.F. Martens, J. N. Huiberts, and P. W.M. Blom. Simultaneous measurement of electron and hole mobilities in polymer light-emitting diodes. *Applied Physics Letters*, 77(12):1852–1854, 9 2000.

[62] H. Martens and P. Blom. Comparative study of hole transport in poly(p-phenylene vinylene) derivatives. *Physical Review B - Condensed Matter and Materials Physics*, 61(11):7489–7493, 3 2000.

[63] J. S. Wilson, A. S. Dhoot, A. J.A.B. Seeley, M. S. Khan, A. Köhler, and R. H. Friend. Spin-dependent exciton formation in π-conjugated compounds. *Nature*, 413(6858):828–831, 10 2001.

[64] M. Wohlgenannt, Kunj Tandon, S. Mazumdar, S. Ramasesha, and Z. V. Vardeny. Formation cross-sections of singlet and triplet excitons in π-conjugated polymers. *Nature*, 409(6819):494–497, 1 2001.

[65] D. Y. Kondakov, T. D. Pawlik, T. K. Hatwar, and J. P. Spindler. Triplet annihilation exceeding spin statistical limit in highly efficient fluorescent organic light-emitting diodes. *Journal of Applied Physics*, 106(12):124510, 12 2009.

[66] Ayataka Endo, Mai Ogasawara, Atsushi Takahashi, Daisuke Yokoyama, Yoshimine Kato, and Chihaya Adachi. Thermally activated delayed fluorescence from Sn4+-porphyrin complexes and their application to organic light-emitting diodes -A novel mechanism for electroluminescence. *Advanced Materials*, 21(47):4802–4806, 12 2009.

[67] M. A. Baldo, D. F. O'Brien, Y. You, A. Shoustikov, S. Sibley, M. E. Thompson, and S. R. Forrest. Highly efficient phosphorescent emission from organic electroluminescent devices. *Nature*, 395(6698):151–154, 1998.

[68] S. Nepurek and J. Sworakowski. Use of space-charge-limited current measurements to determine the properties of energetic distributions of bulk traps. *Journal of Applied Physics*, 51(4):2098–2102, 1980.

[69] G. G. Malliaras and J. C. Scott. The roles of injection and mobility in organic light emitting diodes. *Journal of Applied Physics*, 83(10):5399–5403, 4 1998.

[70] Hua Dong, Zhaoxin Wu, Yaqiu Jiang, Weihua Liu, Xin Li, Bo Jiao, Waseem Abbas, and Xun Hou. A Flexible and Thin Graphene/Silver Nanowires/Polymer Hybrid Transparent Electrode for Optoelectronic Devices. *ACS Applied Materials and Interfaces*, 8(45):31212–31221, 11 2016.

[71] Jens Meyer, Piran R. Kidambi, Bernhard C. Bayer, Christ Weijtens, Anton Kuhn, Alba Centeno, Amaia Pesquera, Amaia Zurutuza, John Robertson, and Stephan Hofmann. Metal oxide induced charge transfer doping and band alignment of graphene electrodes for efficient organic light emitting diodes. *Scientific Reports*, 4(1):1–7, 6 2014.

[72] Michael Naguib, Murat Kurtoglu, Volker Presser, Jun Lu, Junjie Niu, Min Heon, Lars Hultman, Yury Gogotsi, and Michel W. Barsoum. Two-dimensional nanocrystals produced by exfoliation of Ti 3AlC 2. *Advanced Materials*, 23(37):4248–4253, 10 2011.

[73] Soyeong Ahn, Tae Hee Han, Kathleen Maleski, Jinouk Song, Young Hoon Kim, Min Ho Park, Huanyu Zhou, Seunghyup Yoo, Yury Gogotsi, and Tae Woo Lee. A 2D Titanium Carbide MXene Flexible Electrode for High-Efficiency Light-Emitting Diodes. *Advanced Materials*, 32(23):2000919, 6 2020.

[74] Tien Lin Wu, Chao Hui Yeh, Wen Ting Hsiao, Pei Yun Huang, Min Jie Huang, Yen Hsin Chiang, Chien Hong Cheng, Rai Shung Liu, and Po Wen Chiu. High-Performance Organic Light-Emitting Diode with Substitutionally Boron-Doped Graphene Anode. *ACS Applied Materials and Interfaces*, 9(17):14998–15004, 5 2017.

[75] Lai Peng Ma, Zhongbin Wu, Lichang Yin, Dingdong Zhang, Shichao Dong, Qing Zhang, Mao Lin Chen, Wei Ma, Zhibin Zhang, Jinhong Du, Dong Ming Sun, Kaihui Liu, Xiangfeng Duan, Dongge Ma, Hui Ming Cheng, and Wencai Ren. Pushing the conductance and transparency limit of monolayer graphene electrodes for flexible organic light-emitting diodes. *Proceedings of the National Academy of Sciences of the United States of America*, 117(42):25991–25998, 10 2020.

[76] Pradeep Kumar, Kai Lin Woon, Wah Seng Wong, Mohamed Shuaib Mohamed Saheed, and Zainal Arif Burhanudin. Hybrid film of single-layer graphene and carbon nanotube as transparent conductive electrode for organic light emitting diode. *Synthetic Metals*, 257:116186, 11 2019.

[77] Huiying Li, Yunfei Liu, Anyang Su, Jintao Wang, and Yu Duan. Promising Hybrid Graphene-Silver Nanowire Composite Electrode for Flexible Organic Light-Emitting Diodes. *Scientific Reports*, 9(1):1–10, 11 2019.

[78] Lihui Liu, Wenjuan Shang, Chao Han, Qing Zhang, Yao Yao, Xiaoqian Ma, Minghao Wang, Hongtao Yu, Yu Duan, Jie Sun, Shufen Chen, and Wei Huang. Two-In-One Method for Graphene Transfer: Simplified Fabrication Process for Organic Light-Emitting Diodes. *ACS Applied Materials and Interfaces*, 10(8):7289–7295, 2 2018.

[79] Ick Joon Park, Tae In Kim, Taeshik Yoon, Sumin Kang, Hyunsu Cho, Nam Sung Cho, Jeong Ik Lee, Taek Soo Kim, and Sung Yool Choi. Flexible and Transparent Graphene Electrode Architecture with Selective Defect Decoration for Organic Light-Emitting Diodes. *Advanced Functional Materials*, 28(10):1704435, 3 2018.

[80] Zhikun Zhang, Jinhong Du, Dingdong Zhang, Hengda Sun, Lichang Yin, Laipeng Ma, Jiangshan Chen, Dongge Ma, Hui Ming Cheng, and Wencai Ren. Rosin-enabled ultraclean and damage-free

transfer of graphene for large-area flexible organic light-emitting diodes. *Nature Communications*, 8:14560, 2017.

[81] Jaeho Lee, Tae Hee Han, Min Ho Park, Dae Yool Jung, Jeongmin Seo, Hong Kyu Seo, Hyunsu Cho, Eunhye Kim, Jin Chung, Sung Yool Choi, Taek Soo Kim, Tae Woo Lee, and Seunghyup Yoo. Synergetic electrode architecture for efficient graphene-based flexible organic light-emitting diodes. *Nature Communications*, 7(1):1–9, 6 2016.

[82] Piran R. Kidambi, Christ Weijtens, John Robertson, Stephan Hofmann, and Jens Meyer. Multifunctional oxides for integrated manufacturing of efficient graphene electrodes for organic electronics. *Applied Physics Letters*, 106(6):063304, 2 2015.

[83] Ki Chang Kwon, Sungjun Kim, Cheolmin Kim, Jong Lam Lee, and Soo Young Kim. Fluoropolymer-assisted graphene electrode for organic light-emitting diodes. *Organic Electronics*, 15(11):3154–3161, 11 2014.

[84] Xiao Zhao Zhu, Yuan Yuan Han, Yuan Liu, Kai Qun Ruan, Mei Feng Xu, Zhao Kui Wang, Jian Sheng Jie, and Liang Sheng Liao. The application of single-layer graphene modified with solution-processed TiOx and PEDOT:PSS as a transparent conductive anode in organic light-emitting diodes. *Organic Electronics*, 14(12):3348–3354, 12 2013.

[85] Ning Li, Satoshi Oida, George S. Tulevski, Shu Jen Han, James B. Hannon, Devendra K. Sadana, and Tze Chiang Chen. Efficient and bright organic light-emitting diodes on single-layer graphene electrodes. *Nature Communications*, 4(1):1–7, 8 2013.

[86] Tae Hee Han, Youngbin Lee, Mi Ri Choi, Seong Hoon Woo, Sang Hoon Bae, Byung Hee Hong, Jong Hyun Ahn, and Tae Woo Lee. Extremely efficient flexible organic light-emitting diodes with modified graphene anode. *Nature Photonics*, 6(2):105–110, 2 2012.

3

EXPERIMENTAL BACKGROUND

3.1 INTRODUCTION

The purpose of this chapter is to set out the experimental background. These are the experimental techniques and methods used in this work which were developed by others investigating $FeCl_3$ intercalated FLG ($FeCl_3$-FLG) or other materials in the literature. The techniques and methods used in this chapter here are not novel, and not attributable to me. They are nonetheless very important for presenting this work fully. This chapter is divided into two sections, fabrication, and characterisation. I will first discuss experimental fabrication.

3.2 EXPERIMENTAL FABRICATION

3.2.1 *$FeCl_3$-FLG fabrication*

3.2.1.1 *Fishing transfer*

The primary material being studied in this work is $FeCl_3$-FLG, therefore I will look at its fabrication first. Few-layer graphene (FLG) is purchased from Graphene Supermarket. This is a multilayer graphene film grown on a nickel/SiO_2/Si substrate by chemical vapour deposition (CVD). This product is between 1 and 7 layers thick with an average of 4 monolayer thickness. The sample is cut to size, usually $12 \times 12\ mm$. To intercalate this FLG it is transferred from its Si/SiO_2/Ni growth substrate to glass. To achieve this the nickel is etched away to allow the FLG to float free on the surface of the etchant solution. First a poly(methyl 2-methylpropenoate) (PMMA) support

layer is spin-coated on top, this layer is a 495K A6 PMMA solution, spun at 5000 RPM for 1 minute to give a layer approximately 300 nm thick. The sample is then baked on a hot plate at 150°C for 10 minutes. To ensure the nickel can be etched the edges of the sample are scratched with a scalpel, this removes the PMMA and allows the etchant in. The etchant in this case is $FeCl_3 \cdot 6H_2O$, diluted in deionised (DI) water to 1M.[1;2] When all the nickel is etched, the SiO_2/Si substrate sinks, while the FLG with PMMA support remains floating. The floating sample can now be "fished" out of the etchant using a glass spatula and placed in DI water. Three DI water baths are used to remove any remaining etchant from the sample. The floating sample can now be "fished" again onto a cleaned glass substrate. The sample is allowed to dry in air for several hours, before being placed in a desiccator to remove any remaining water. Finally, the PMMA is removed by placing the sample in an acetone bath at 60°C for several hours, with the acetone being refreshed twice. The sample is finally rinsed in propan-2-ol (IPA) and blow dried with nitrogen.

3.2.1.2 *Intercalation*

With FLG successfully transferred to glass the final step in making $FeCl_3$-FLG is intercalation with $FeCl_3$. Intercalation of graphite intercalation compounds (GICs) traditionally involves the use of a two or three-zone furnace.[3] A three-zone furnace was used in this work (as shown in Figure 3.1). First the intercalate and sample are loaded into zones 1 and 2, respectively. The furnace is then sealed and evacuated to high vacuum ($\approx 10^{-9}$ $mbar$). It is pumped at vacuum for 30 minutes to ensure any moisture is removed; it is then sealed from the pump. In zone 1, $FeCl_3$ is heated to just above its sublimation temperature of 315°C. This causes $FeCl_3$ vapour to fill the furnace. The sample in zone 2 is heated to 360°C, this high temperature allows the intercalate to diffuse in between the graphene layers and causing an expansion due to the charge transfer between the intercalate and the graphene. This intercalation method is called the vapour-transport, in this method the amount of the intercalate depends on the temperature difference between the zone 1 and 2.[3] To draw the vapour from zone 1 though zone 2, zone 3 is kept at 300°C, here the vapour recrystallises. The furnace can be seen in Figure 3.1 (a). Zone 1 is kept at high temperature for 11.5 hours, while zones 2 and 3 are kept hot for 12 hours. This is done to ensure the

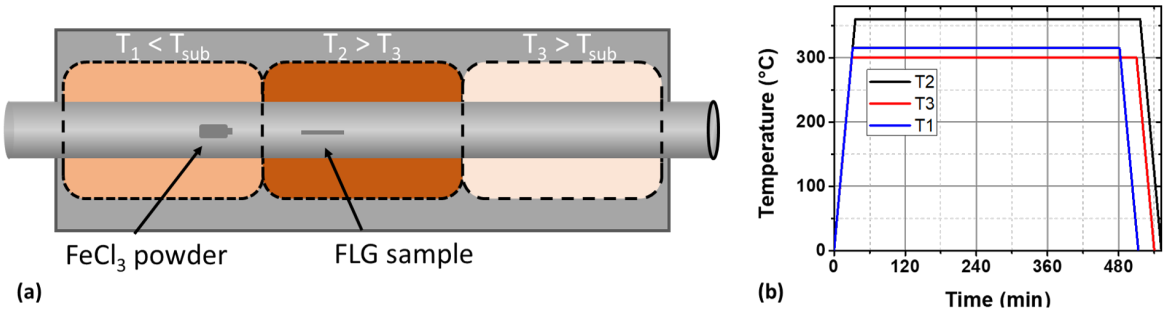

Figure 3.1: **(a)** Diagram of the three-zone furnace used to intercalate FLG into $FeCl_3$. **(b)** Graph showing the temperature of each zone of the furnace throughout the procedure.

vapour crystallises away from the sample. If $FeCl_3$ crystallises on the sample, it will surface dope the sample and increase the surface roughness of the $FeCl_3$-FLG. When the furnace programme completes it is allowed to cool naturally. The furnace is once again pumped down to $\approx 10^{-9}$ *mbar* for 30 minutes to remove any remaining vapours. The new $FeCl_3$-FLG sample is now removed and immediately put into a warm IPA bath for 10 minutes. This bath can physically remove any loose contaminants. The sample is blow dried with nitrogen and stored in a desiccator to ensure it is kept clean. $FeCl_3$-FLG has shown extremely high ambient stability in the past.[4]

3.2.1.3 *Thermal transfer to flexible substrate*

The intercalation process takes place at 360°C, therefore if a flexible substrate is desired for $FeCl_3$-FLG it must be transferred after intercalation. The most common flexible substrate used is polyethylene terephthalate (PET), which has a melting point of 260°C.[5] The fabrication process therefore for $FeCl_3$-FLG on PET is fishing transfer to glass, intercalation on glass, thermal transfer to PET.

Thermal transfer involves the use of a thermally deactivated adhesive to peel the $FeCl_3$-FLG from glass, then release it onto PET. The thermal transfer tape used in this work is a one-sided tape from Graphene Supermarket (SKU - GTT) with a 100°C release temperature. The whole process is visualised in Figure 3.2.

The first step in the thermal transfer process is to spin-coat 300 *nm* of PMMA 495K as a support layer. Before spinning this PMMA support, the edges of the substrate are masked with 75 μm thick PVC dicing tape with an acrylic adhesive substrate

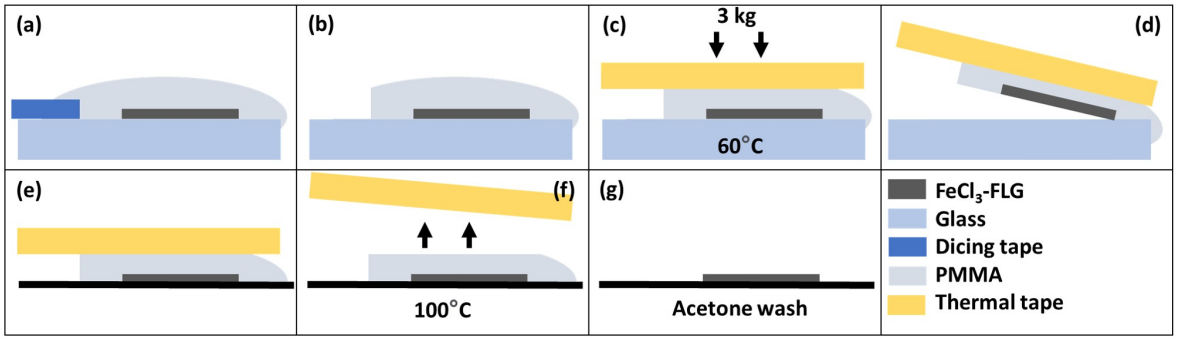

Figure 3.2: **(a)** PMMA coated $FeCl_3$-FLG sample on glass, dicing tape masks off the edge. **(b)** Dicing tape is peeled away to reveal a clean PMMA edge. **(c)** Thermal tape is applied, and the sample is heated under weight. **(d)** All layers are peeled off the glass. **(e)** Layers are transferred to PET. **(f)** Sample is heated to release temperature and thermal tape removed. **(g)** Sample is washed in acetone to remove PMMA.

(Loadpoint 6033/6034). This is to ensure when peeled off there is a PMMA edge on the glass substrate. The thermal tape will peel the PMMA from this point. Once the PMMA is spun, the sample, with dicing tape still attached, is baked on a hot plate at 150°C for 10 minutes.

The samples are removed from the hot plate and the dicing tape is peeled off, to leave a clean PMMA edge on the glass substrate. Thermal transfer tape is now applied to the sample, ensuring the PMMA edges are covered. This is firmly pressed in place. A 3 kg lead weight is pre-heated to 60°C and placed on top of the sample on the 60°C hot plate. This is allowed to settle for 10 minutes.

The sample is removed from the hot plate, blown with nitrogen to quickly cool to room temperature, then using a scalpel the thermal tape is peeled up from the corner with the PMMA edge. The $FeCl_3$-FLG should be lifted with it.

The thermal tape now has $FeCl_3$-FLG on the underside. At this stage inverted $FeCl_3$-FLG (discussed in more detail later, and seen in Figure 7.5 (b)) is created. The thermal tape, with $FeCl_3$-FLG attached, is now applied to a clean PET substrate. The PET substrate is placed onto a hot plate at 80°C and the temperature incremented up by 1°C every 30 seconds. Once the tape releases it visibly changes colour. The $FeCl_3$-FLG on PET can now be removed from the hot plate. Finally, the sample is rinsed in warm (50°C) acetone for 5 minutes to remove the PMMA, before being rinsed

with IPA and dried with nitrogen.[6]

3.2.2 *OLED fabrication*

While the properties of $FeCl_3$-FLG appear comparable, if not better than indium tin oxide (ITO) for use as transparent conductive electrode (TCE) in organic light-emitting diodes (OLEDs) on paper (Table 5.3), the only sufficient way to test the material properly, taking all properties into account simultaneously, is to test the material in a working device.

OLEDs have been fabricated successfully since the 90s, by using solution processing and evaporation.[7] Evaporation has become the dominant form of OLED manufacture and has allowed the technology to be commercialised.[8] One of the main drawbacks of this technique is that it is extremely costly to set up.[9] In my group, no OLEDs had ever been fabricated before, so the skills or equipment were not present and needed to be developed.

The simplest way to fabricate an OLED is through solution processing.[10] One of the cheapest and most controlled lab technique is spin-coating.[10] Many organic materials can readily be dissolved in solvent and spin-coated to give a very thin, highly uniform film. This is the basis for all OLEDs presented in this thesis.

Evaporation is a high purity, clean, scalable way of material deposition.[9;10] Evaporating organics is possible, but it is complex. When organics are evaporated, they coat all surfaces within the evaporation chamber, when the chamber is opened to ambient, they can quickly oxidise and hydrolyse.[11;12] This means evaporators need to be operated within an inert, dry environment. To maintain a low-cost, and scalable solution I decided to use a solution processed technique, namely spin-coating. I will however evaporate metals. Metals are much cleaner to evaporate, often inert, and can be exposed to ambient conditions without issue. I therefore chose to evaporate gold and aluminium as required while maintaining low-cost and scalability.

The first step in OLED fabrication is choosing the device structure and materials. Two different device structures are presented in this thesis; conventional and inverted, the chosen structures can be seen in Figure 3.3.

3.2.2.1 *Inverted OLED structure*

The recipe chosen has been shown previously to be efficient and reliable.[13;14] Critically all the materials used can be taken in solution form or replaced with similar solution substitutes. The recipe is based on the use of poly(9,9-dioctylfluorene-alt-benzo-thiadiazole) (F8BT) as the emission layer. F8BT is a green emitting polymer commonly used in OLEDs for research.[15] It has deep highest occupied molecular orbital (HOMO) and lowest unoccupied molecular orbital (LUMO) levels, at -5.9 eV and -3.3 eV respectively, these make it more air stable than many other emission layers.[16] It can be readily dissolved in p-xylene or toluene and withstand temperatures up to 200°C.[13;17]

The other layers must now be chosen to match the energy levels of F8BT and be solution processable. A common hole transport layer (HTL) used in conjunction with F8BT is MoO_3.[13;14;18] This is used because of its very deep LUMO level (-6.9 eV) which can function as a hole source.[19;20] MoO_3 has several drawbacks, however. It must be processed in an inert atmosphere to prevent it from oxidising, and it is usually evaporated. One way of overcoming the latter issue is to dissolve MoO_3 in poly(3,4-ethylenedioxythiophene) polystyrene sulfonate (PEDOT:PSS).[21] This allows the mixture to be spin coated, the PEDOT:PSS also protects against some oxidation.[21] To further protect against oxidation this deposition was to be done in a nitrogen glovebox. The addition of PEDOT:PSS will raise the LUMO energy, however it is expected that the mixture will remain a good hole source, as PEDOT:PSS is widely used as a HTL on its own.[22]

For the anode, a low work function material is required for the device. Gold was chosen due to its stability, low work function (5.1 eV), ease of deposition using thermal evaporation, and its reflectively.[23] A relatively thick 100 nm layer is used to protect the device structure below when metal contacts are attached.

On the cathode side of the emission layer, a thin hole-blocking layer is used. This layer has been shown in previous studies to increase device efficiency and prevents holes moving beyond the emission layer.[24] This material is polyethylenimine ethoxylated (PEIE), with HOMO/LUMO levels at -6.5 eV and -2.9 eV.[24] This material is dissolved in IPA and spin-coated onto the device.

Furthermore, an electron transport layer (ETL) is needed to overcome the 1.5 eV

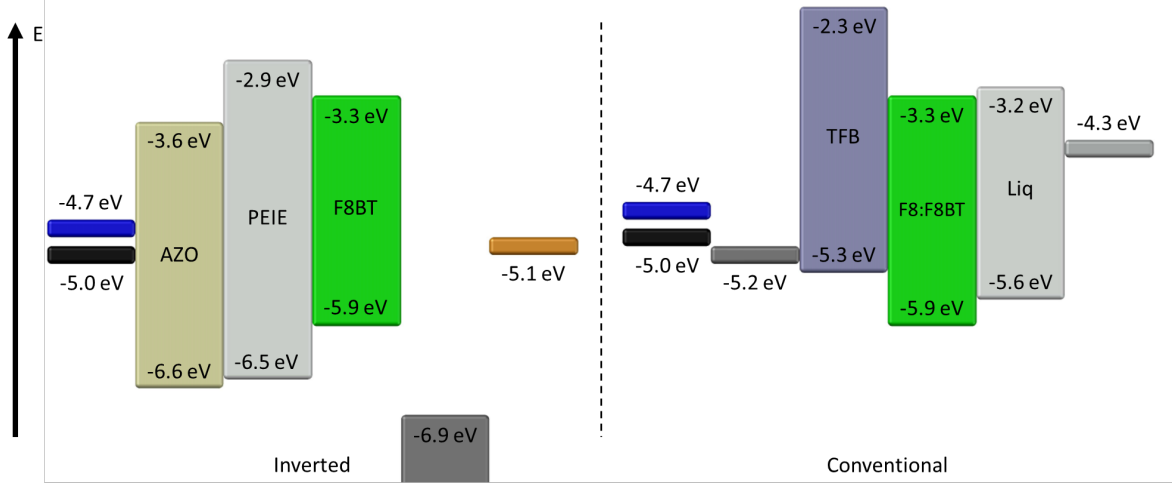

Figure 3.3: Left: Energy level diagram of the inverted OLED. The materials from left to right are: $FeCl_3$-FLG (black) or ITO (blue), AZO, PEIE, F8BT, MoO_3:PEDOT:PSS and gold. **Right:** Energy level diagram of the conventional OLED. The materials from left to right are: $FeCl_3$-FLG (black) or ITO (blue), PEDOT:PSS, TFB, F8:F8BT, Liq, and aluminium.

difference in energy levels between ITO at -4.7 eV and F8BT at -3.2 eV. To do this, a common ETL in the form of aluminium doped zinc oxide (AZO) was used. AZO (Avantama N21-X) is a solution of aluminium doped zinc oxide nanoparticles dispersed in a mixture of IPA and ethanol. It has a LUMO level at -3.6 eV, which is about halfway between that of ITO and F8BT.[25] It should be noted that the work function of $FeCl_3$-FLG is thought to be between -5.0 eV and -5.5 eV, meaning it is expected that there will be a larger electron injection barrier for the $FeCl_3$-FLG device, and therefore a higher turn-on voltage.[26;27]

Finally, the TCE will be $FeCl_3$-FLG, the material being investigated, and ITO, the near universal industry standard.[28]

3.2.2.2 *Conventional OLED structure*

The second device architecture used in this thesis is the conventional structure. This architecture was chosen to attempt to improve device performance in $FeCl_3$-FLG based devices. Stability and lifetime are particularly important properties when it comes to consistent measurements of electrode performance. The stability issue is acute when the devices are subject to bending, the whole device, needs to be able to outperform

the electrode to assess the electrode flexibility as the point of failure.

The F8BT is chosen again for the same reasons described in the previous section. F8BT is a common research material and is easy to reference with literature. To further increase efficiency and stability during deposition F8BT was mixed with poly(9,9-di-n-octylfluorenyl-2,7-diyl) (F8) (also known as PFO) in a 1:19 ratio.[29–31] This is a technique not done in the previous section and is done here to aid device performance.

To bring electrons into the emission layer an electron injection layer (EIL) is required. For this LiF or Ca is most commonly used.[31;32] These materials can be easily thermally evaporated, however, to maintain the solution processability of the device, and hence scalability, it was substituted for a less common material in 8-hydroxyquinolinolato-lithium (Liq). A very thin (1 - 2 nm) layer, when coupled with aluminium is known to be an effective EIL.[33] It is also known to help improve the stability of light-emitting diodes (LEDs).[33] Liq has a HOMO/LUMO of -5.6 / -3.2 eV.[34]

As mentioned, aluminium is used as the cathode metal. Aluminium is a common cathode material due to its relative ease of evaporation, stability, high work function of -4.3 eV, and its high reflectively.[35;36]

To ensure sufficient hole transport into the emission layer a HTL of poly(9,9-dioctylfluorene-alt-N-(4-sec-butylphenyl)-diphenylamine) (TFB) is used. This material has a HOMO/LUMO of -5.3/-2.3 eV, meaning it also acts as an electron blocking layer (EBL). The use of this material is intended to increase charge carrier recombination in the active layer and increase overall efficiency.[37;38]

Finally, one of the most widely used HTL polymers in OLEDs and photovoltaics (PVs) alike is PEDOT:PSS.[22;39] PEDOT:PSS does not coat well on ITO,[40] however through use of ultraviolet (UV) ozone treatment it can be coated very well on $FeCl_3$-FLG.[41–43] The work function of PEDOT:PSS is -5.2 eV, this will match that of $FeCl_3$-FLG well and help reduce the energy barrier for ITO.

3.2.2.3 *Inverted fabrication process*

Fabrication for both architectures can be summarised as follows: first the cleaned substrate is taken, this will be either patterned ITO on glass, etched ITO on PET, patterned $FeCl_3$-FLG on glass, or patterned $FeCl_3$-FLG on PET. For all these sub-

strates and electrodes, the device structure is the same and the patterning is the same. The OLEDs made are 12 × 12 mm, the TCE is a 7 mm strip down the centre, this can be seen in Figure 3.4 (a).

More specifically, the first part of fabrication is to prepare the surface of ITO. ITO (LumTek 15Ω/□) is exposed to oxygen plasma to make the surface hydrophilic.[44;45] This has the dual benefit of cleaning the sample, and changing the surface chemistry to allow for better wettability and smoother AZO layer.[44;45] $FeCl_3$-FLG samples are not exposed to the plasma as it was found that will damage the graphene.

The samples are then coated with AZO (Avantama N-21X). This solution is briefly sonicated (60 seconds) to break up any aggregates that may have formed. It is filtered into a clean vial through a 0.45 μm syringe filter. The solution is dropped onto the stationary sample in the spin-coater, this is to ensure uniform coverage. The sample is spun at 2500 RPM (discussed in Section 4.4). The sample is then baked at 200°C or 120°C for glass or PET substrate, for 10 minutes.

PEIE (Sigma Aldrich - 306185) is then prepared, 0.4% by volume in IPA. The PEIE is filtered into a clean vial through a 0.45 μm syringe filter. The solution is dropped onto the stationary sample on the spin-coater before being spun at 5000 RPM for 60 seconds. The sample is then baked on a hot plate at 105°C for 10 minutes to remove the IPA.

F8BT is prepared and deposited in a nitrogen glovebox. The glovebox maintains < 1 ppm oxygen and moisture and is shielded from external UV. The F8BT (Cambridge Display Technology) is weighed out on a chemical balance and mixed with p-xylene for a 20 mg/ml concentration. This solution is heated to 80°C for 10 minutes to ensure the solid F8BT is dissolved fully. The solution is then filtered using a glass syringe and a 0.45 μm poly(1,1,2,2-tetrafluoroethylene) (PTFE) syringe filter into a clean vial. The solution is dropped onto the stationary sample on the spin coater, before being spun to 2500 RPM for 60 seconds. The sample is then baked at 155°C for 45 minutes.

MoO_3:PEDOT:PSS must also be used in the glovebox. PEDOT:PSS is not usually used in glovebox environments as it is usually dissolved in water. In this case the mixture is dissolved in ethanol and can be used in the glovebox without raising the moisture content. The MoO_3:PEDOT:PSS is briefly sonicated for 60 seconds to break up any aggregates. It is then filtered into a vial using a 0.45 μm syringe filter. The solution is dropped onto the stationary sample and spun at 2500 RPM (discussed in

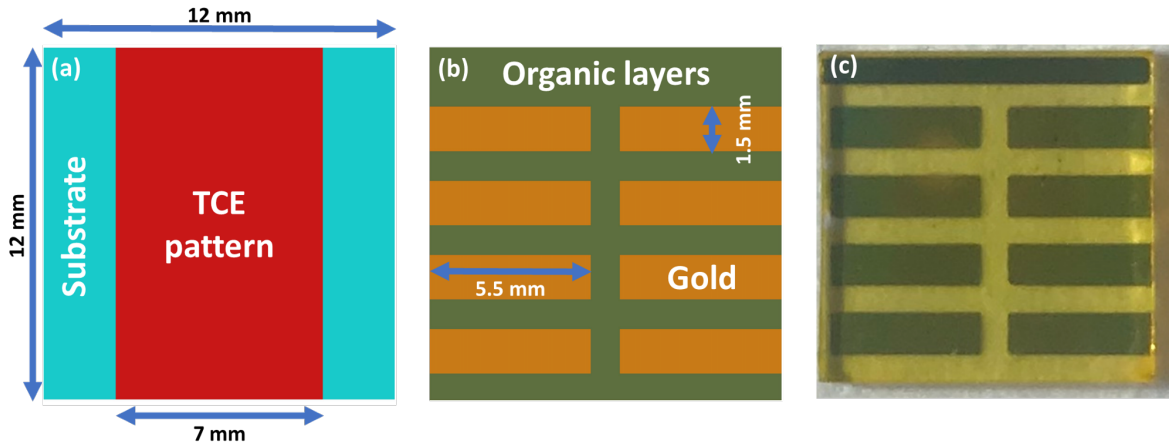

Figure 3.4: **(a)** The pattern of the TCE shown on the substrate. The pattern is a 7 × 12 mm rectangle centred on a 12 × 12 mm substrate. **(b)** The pattern of the metal electrode evaporated on the organic layers. There are 8 pixels, which are 5.5 × 1.5 mm, giving an active area of 3 × 1.5 mm (4.5 mm^2). **(c)** Photograph of a fabricated OLED device. A gold bar was evaporated directly onto the ITO to ensure good electrical contact.

Section 4.4). The sample is then baked on the hot plate at 160°C for 10 minutes. The sample is sealed into a moisture barrier bag before being removed from the glovebox.

Gold evaporation takes place using a HVV thermal evaporator in an ISO 6 clean room environment. The sample is removed from the sealed bag, quickly fitted to a shadow mask, and loaded to the evaporator, which is pumped to vacuum as quickly as possible to reduce time in ambient conditions. The mask is a metal shadow mask with the pattern shown in Figure 3.4 (b) to give 8 pixels. The evaporator is pumped to $< 1 \times 10^{-6}$ $Torr$ before evaporation begins. The gold is thermally evaporated at a rate of 0.1 nm/s. The sample holder is rotated at all times during evaporation to ensure uniform results. 60 nm of gold is evaporated (measured by a 6 MHz quartz crystal). After evaporation, the chamber is filled with nitrogen, opened, and the sample is placed into a desiccator, where it is held in the dark, until it is measured. The resulting device is pictured in Figure 3.4 (c), here this device had a gold strip evaporated on top of the ITO to help with electrical contact. This practice was dropped when it was found to have no/negligible effect.

3.2.2.4 *Conventional fabrication process*

As with the inverted devices, the first fabrication step is to treat the surface of the TCE on the substrate. The TCE is placed in a UV ozone cleaner (Ossila) and exposed to the ozone for 9 minutes. This increases the hydrophobicity of both $FeCl_3$-FLG and ITO, crucial for spinning PEDOT:PSS.[43]

PEDOT:PSS (Ossila - M121) is filtered into a vial using a 0.45 μm hydrophobic PTFE syringe filter. The PEDOT:PSS is in solution in water, so it must be processed outside the glovebox. The PEDOT:PSS is dropped onto a stationary sample, before being spun at 5000 RPM for 30 seconds to give a layer 30 - 40 nm thick. The sample is then loaded into the glovebox and baked on a hot plate at 150°C for 5 minutes.

TFB (Ossila - M0981A1) is prepared in advance, it is dissolved in p-xylene (Sigma Aldrich) to 7 mg/ml and stored on a hot plate at 50°C for 24 hours. It is then filtered using a glass syringe and 0.45 μm PTFE syringe filter into a clean vial. The solution is dropped onto the stationary sample, before being spun at 4000 RPM for 30 seconds. The sample is then annealed on a hot plate at 180°C for 10 minutes.

F8:F8BT (Ossila M0161A2:M0231A4) is next made up in a 19:1 ratio by weight. It is dissolved in toluene to 15 mg/ml. The solution is placed on a hot plate at 80°C for 10 minutes to allow it to fully dissolve. The cool solution is then filtered into a clean vial using a glass syringe and a 0.45 μm PTFE syringe filter. The solution is dropped onto the stationary sample, before being spun at 2000 RPM for 30 seconds to give a layer 80 nm thick. The sample is then annealed on a hot plate at 80°C for 10 minutes.

Liq is next dissolved in 2-ethoxyethanol to 1 mg/ml. The solution is then filtered into a clean vial using a glass syringe and a 0.45 μm PTFE syringe filter. The solution is dropped onto the spinning sample, before being spun at 2000 RPM for 60 seconds to give a layer 1 - 5 nm thick. The sample is then annealed on a hot plate at 80°C for 10 minutes. The sample is placed into a sealed moisture barrier bag before being removed from the glovebox.

Aluminium evaporation takes place using a HVV thermal evaporator in a similar procedure to the one discussed for gold evaporation in the previous section. In this case the parameters are rate: 0.1-5 nm/s, thickness: 100 nm.

3.3 CHARACTERISATION

3.3.1 *Electrical characterisation of graphene*

The primary electrical property sought for any TCE is its sheet resistance, defined in Equation 2.8. This value is absolute and allows comparisons between our material and others of differing scales and disregarding layer thickness i.e., assuming it is negligible. It can also be useful however to talk about resistance on its own.

3.3.1.1 *Two-point measurements*

Two-point measurements are used to measure the resistance. Here the resistance of the probes is measured and assumed to be constant. The length and width of the sample also contribute significantly to the reported value, as resistance can be defined as:

$$R = \rho \frac{l}{A} \tag{3.1}$$

where ρ is the resistivity of a conductor, l is the length of the conductor, and A is the area of the cross section. When taking two-point measurements they are only useful if the test apparatus is the same, and the samples have the same dimensions. This is sometimes the case and is used in this work when calculating values of R/R_0 as it simplifies the measurements.

3.3.1.2 *Four-point measurements*

A more rigorous way of measuring the electrical properties of samples is using a four-point method. This method eliminates any contact resistance that may be in the measurement setup, giving a value of resistance only attributable to the sample.[46] It also allows sheet resistance R_S to be calculated, which is dimensionless, and this allows comparisons of samples of various sizes. This is what is described in Equation 2.8.

The four-point setup used is a Signatone S-302-4/SP4 four-point probe system. This is connected to a Keithley 2400 source measurement unit operating in four-point mode to simultaneously source voltage and measure current and calculate resistance. The working principle of this type of measurement can be visualised in Figure 3.5 (a) & (b). In Figure 3.5 (a) only the voltage across the inner probes is measured, this is

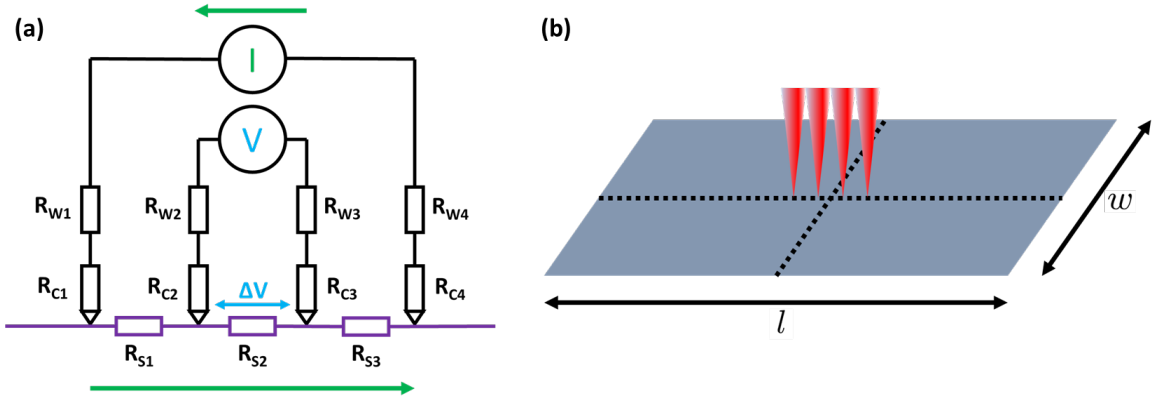

Figure 3.5: **(a)** The circuit diagram of the four-point probe. The probes are numbered 1 - 4, left to right. R_W refers to the wire resistance, R_C refers to the contact resistance, and R_S refers to the sample resistance. The green arrows indicate the direction of current flow. **(b)** The four points contacting a sample of width w and length l. Here $l > w$.

because voltmeters have high electrical impedance, so negligible current will flow here, this means that the contact resistances (R_{C2} and R_{C2}), and the wire resistances (R_{W2} and R_{W2}) will not be measured. The measured decrease in voltage will be entirely from R_{S2}.

The sheet resistance is calculated from the resistance multiplied by a correction factor, $C.F.$. In the case where the sample is infinitely larger (or approx. 40 times) the correction factor goes to 1.[46] The value of the correction factor is heavily dependent on the sample geometry.

$$R_S = \frac{\pi}{\ln(2)} \frac{\Delta V}{I} \cdot C.F. = 4.53236 \frac{\Delta V}{I} \cdot C.F. \tag{3.2}$$

When the sample is smaller than 40 times the distance between the probes the correction factor will be significantly different. This is because the current paths become limited by the edges of the sample. Square or rectangular samples were used throughout this work. In this case the correction factor cannot be derived. Instead, they have been empirically determined. The correction factors used were obtained from Haldor Topsoe, Geometric Factors in Four Point Resistivity Measurement, 1966.[46] In the case of the 12 $\times$ 7 mm device, a correction factor of 0.9345 was used, in the case of 10 $\times$ 10 mm samples 0.9313 was used.

3.3.1.3 *Van der Pauw measurements*

Sometimes using a four-point probe is not appropriate, in the case where a sample may be too small for the probes, or where the sample is fragile, or offers poor electrical contact to probes. In this case the Van der Pauw method was used.[47] The Van der Pauw method relies on placing four probes on the perimeter of the sample, this allows the average resistance of the entire sample to me measured in all directions, rather than just in the sensing direction as with the linear four-point probe. For a square sample Ohmic contacts were placed on the corners. These are usually a small drop of silver paint, the smaller the better, right on the edge. The error resulting from the size of the contacts is of the order D/l, where D is the diameter of the contact, and l is the distance between contacts. In this case $D/l \approx 1/10 = 10\%$.The contacts on the sample were labelled 1 - 4, anti-clockwise from the top left. To start, $R_{12,34} = \frac{V_{34}}{I_{12}}$ was measured, followed by $R_{23,41} = \frac{V_{41}}{I_{23}}$. These measurements are related to the sheet resistance, R_S, by the Van der Pauw formula:

$$e^{-\pi \frac{R_{12,34}}{R_S}} + e^{-\pi \frac{R_{23,41}}{R_S}} = 1 \tag{3.3}$$

For a square sample, where $R_{12,34} = R_{23,41}$, then the Van der Pauw formula can be solved for R_S:

$$R_S = \frac{\pi R}{\ln(2)} \tag{3.4}$$

This is also seen in Equation 3.2. The Van der Pauw measurement can be made more accurate by doing reciprocal measurements. Here $R_{AB,CD} = R_{CD,AB}$. This leads to two more measurements, and the results can be averaged. Reversed polarity measurements can also be done by taking all the measurements again in the opposite polarity and averaging the results. This will give two final measured R values of:

$$R_{\text{vertical}} = \frac{R_{12,34} + R_{34,12} + R_{21,43} + R_{43,21}}{4} \tag{3.5}$$

$$R_{\text{horizontal}} = \frac{R_{23,41} + R_{41,23} + R_{32,14} + R_{14,32}}{4} \tag{3.6}$$

These can be plugged into Equation 3.3 for a final value. By doing this extra measurement, any thermoelectric potentials due to the Seebeck effect are cancelled

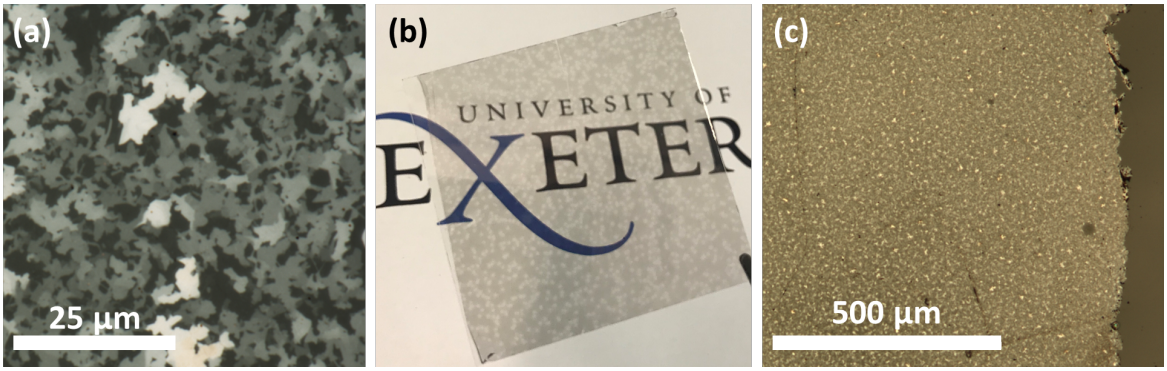

Figure 3.6: Optical images showing holes, debris, wrinkles, and domains. **(a)** Microscope image showing domains. **(b)** Optical image showing holes on a 5×5 *cm* sample of $FeCl_3$-FLG. **(c)** Microscope image showing wrinkles, and the debris at the edge of an $FeCl_3$-FLG sample.

out.[47]

3.3.2 *Optical characterisation*

3.3.2.1 *Microscopy*

There are three ways in which TCE materials are optically characterised. The simplest is using an optical microscope, here holes, debris, wrinkles, and domains can be seen (Figure 3.6), this can give an indication about the overall quality of the material very quickly.

3.3.2.2 *Raman spectroscopy of graphene*

3.3.2.2.1 *Introduction*

Raman spectroscopy is an invaluable characterisation technique for crystalline materials. It is widely used in chemistry to identify materials' unique vibrational fingerprint.[49;50] Raman can determine the vibrational modes of molecules in the crystal. These modes are inferred from the inelastic scattering of photons in the crystal. Raman works by having a monochromatic laser light shine on a sample. The laser light interacts with the vibrations in the crystal structure. This interaction results in a shift in the energy of the laser photons up or down. This shift is what is measured and what

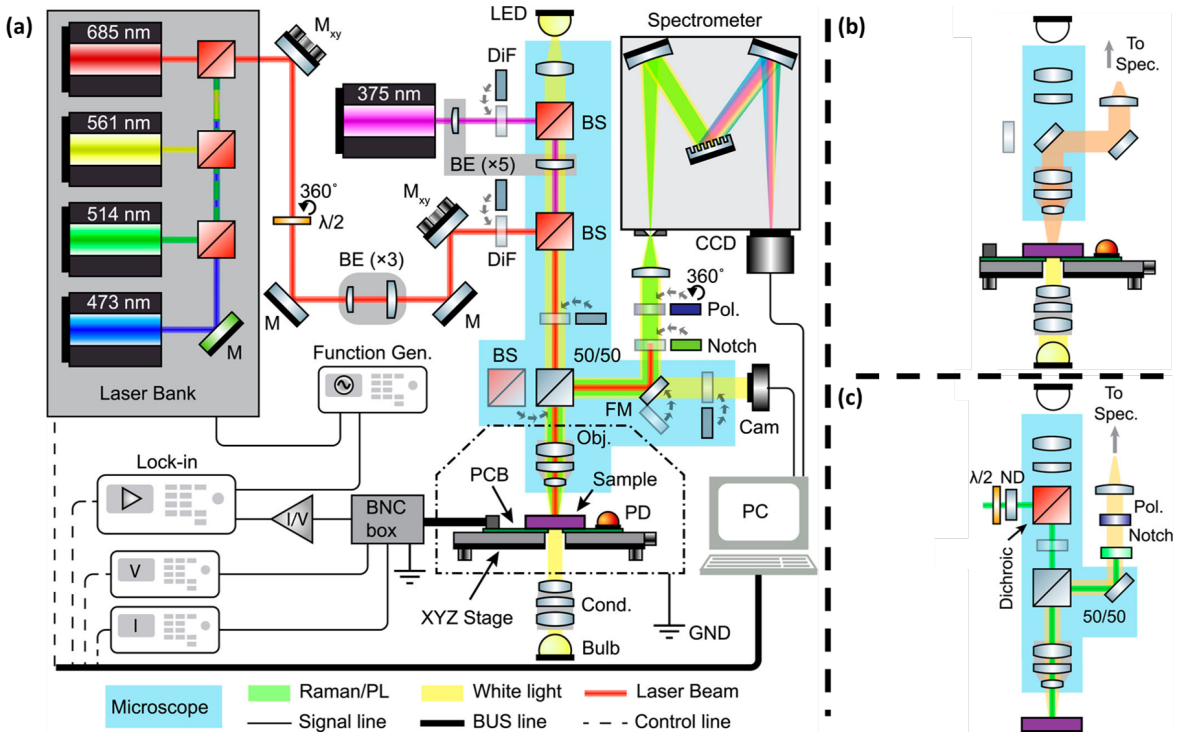

Figure 3.7: **(a)** Schematic of the microscope. Laser light is used for Raman and photoluminescence spectroscopy. An XYZ motorized microscope stage allows precise control of the sample position. The dashed-dotted line represents the electrically screened light-tight enclosure of the sample stage. Signal lines carry electric/data signals to be measured, control lines carry the signals to configure the instruments, the lasers, and the other sources, BUS line comprises USB and GPIB. Abbreviations: mirror (M), kinematic mirror (M_xy), half-wavelength plate ($\lambda/2$), beam expander (BE, followed by magnification), drop-in filter (DiF), beam splitter (BS, dichroic in red), Polariser/Analyser (Pol.), white light (WL), voltage (V) or current (I) sources/meters, flip mirror (FM), sample holder (PCB), photodetector (PD), condenser (Cond), microscope objective (Obj), imaging camera (Cam), spectroscopy camera (CCD), ground line (GND). **(b)** The optical path configuration used during transmittance measurements using white light and **(c)** Raman spectroscopy. Figure reproduced with permission.[48]

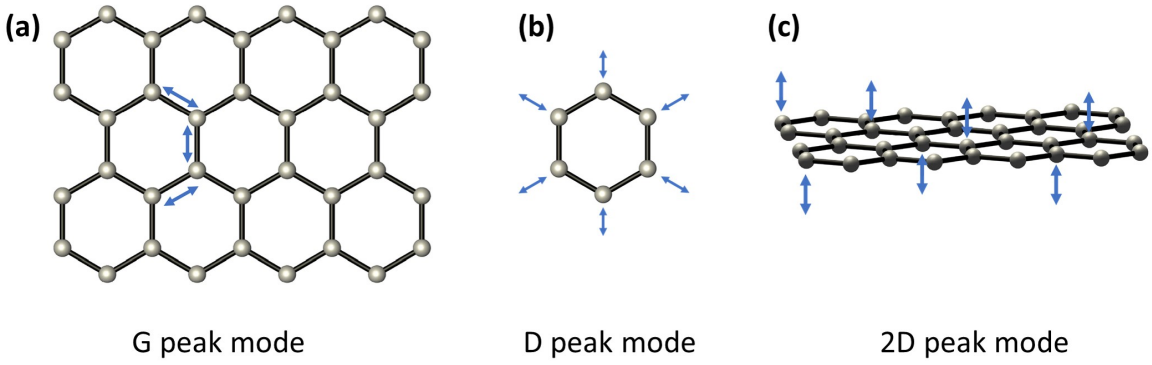

Figure 3.8: The three primary vibrational modes of graphene are shown. The G peak corresponds to the E_{2g} vibrational mode **(a)**, the D peak corresponds to the breathing mode which occurs when defects are present **(b)**, and the 2D peak corresponds to the out-of-plane A_{1g} mode which can be used to infer the number of layers present **(c)**.

gives information about the vibrational modes in the crystal. When the laser light is returned to the detector the Rayleigh scattered light must be filtered out. This is typically done by using a notch filter, or band pass filter. The remaining light should be exclusively the Raman shifted light. Raman shifted light, red-shifted (Stokes), or blue-shifted (anti-Stokes), accounts for just 1 ppm of scattered light, with the vast majority being Rayleigh shifted. Throughout this work Raman spectroscopy is carried out using the system seen in Figure 3.7.

3.3.2.2.2 *Raman on single-layer graphene*

For analysing the crystal structure of graphene and functionalised graphene Raman spectroscopy is one of the most important tools. Raman spectroscopy is a fast, easy, and non-destructive way of assessing the crystal structure of graphene.[51;52] Many properties can be inferred from Raman spectroscopy including, defects, doping, disorder, strain, number of layers, and charge carrier density.[52–55]

Looking at the Raman spectrum of graphene, there are typically 3 main peaks. These are the D peak at 1350 cm^{-1}, the G peak at 1580 cm^{-1}, and the 2D peak at 2750 cm^{-1}.[52]

The most important peak for the work conducted in this thesis is the G peak. This peak arises because of the E_{2g} vibrational mode. This is the mode associated with the

stretching of the sp^2 bonds in the lattice.[55] As this peak is a result of sp^2 bonding, it is always present in graphene and graphite compounds. This peak can be examined as an indicator of strain in graphene, as strain will change the resonant frequency of these bonds.[56] Strain is not the only property that can change the G peak position. Importantly for this work, the G position can also indicate doping of graphene.[55] When the charge density of the graphene changes so does the screening of the ionic potential created by the nuclei. This effect is enhanced due to a Kohn anomaly.[57] Lazzeri et al.[57] have been able to calculate the G peak shift theoretically due to doping, therefore these calculations can be used to work out charge density directly from the G peak position.[57] Since the shift in G peak can be caused by strain or doping, the two effects can be distinguished by looking at the change in the 2D peak shift as a function of the G peak shift.[58]

Finally, the intensity of the G peak is linked to the number of graphene layers present.[59] A higher number of layers will give a more intense signal. The G peak intensity is usually compared to the intensity of the 2D peak to infer the number of layers.[60] However this does not always apply due to the doping induced change in the 2D peak. This can be controlled for by comparing to the Si peak when the sample is on Si.[61]

The D peak occurs only when a defect, i.e., missing atom, is present.[62] This peak is a result of the breathing mode when the C atoms move in and out as seen in Figure 3.8 (b). The presence of this peak is a good indicator of poor-quality graphene. Usually the D/G ratio is examined for this, with D/G ≤ 0.5 considered good.

Finally, the 2D peak corresponds to the A_{1g}, out-of-plane, vibrational mode.[52] This peak is useful in layer number determination. In single layer graphene (SLG) only one transition is possible, therefore there is a single 2D peak present. In bilayer graphene (2LG) there is a double dispersion band, so 4 transitions are possible, giving a 2D peak which is a convolution of 4 peaks. After 5 layers the 2D peak is stable and does not significantly change with layer number.[60] To determine layer numbers Lorentzians can be fitted to the 2D peak, this is accurate up to 3 layers, beyond this the ratio of G/2D intensity needs to be examined. Typically, in SLG the G/2D ratio is 0.5, in 2LG it is 1.0, and in tri-layer graphene it is 1.5. As mentioned previously, this can be affected by doping.

The mechanism behind these three characteristic peaks can be seen in Figure 3.9.

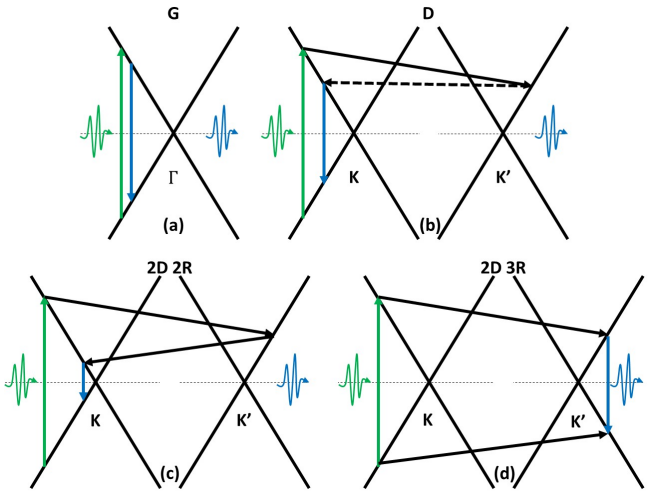

Figure 3.9: **(a)** The scattering process which results in the G peak in graphene and the **(b)** D peak, **(c)** 2D double resonance, and **(d)** triple resonance. The green lines represent the incident photons, blue is the scattered photons, black is an inelastic scatter, and dashed black is a defect enabled elastic scatter.

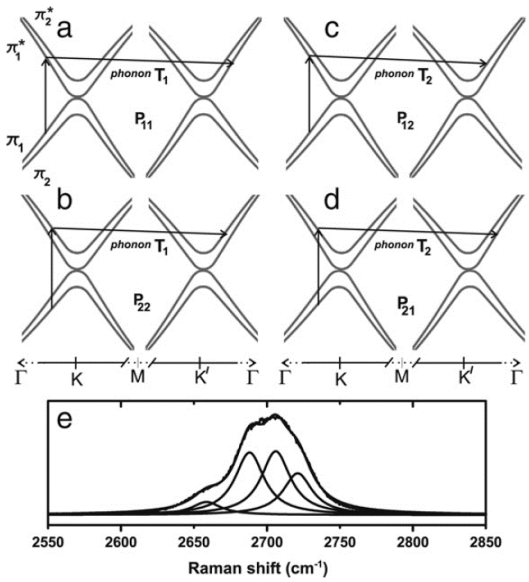

Figure 3.10: The bands in bilayer graphene are now multiple and parabolic in shape. **(a - d)** The four scattering processes which result in the 2D multipeak structure. There are now four possible transitions. **(e)** The four transitions result in four Lorentzians which are fit to a 2LG 2D peak. Reproduced with permission.[63]

The characteristic graphite G peak results because of a transition within the Dirac cone at the Λ point (Figure 3.9 (a)).[63] When a photon is absorbed, an electron is scattered by the stretching of the E_{2g} phonon mode. Once scattered the electron and hole pair will recombine at a slightly different level. The difference in energy is the Raman shift which results in the 1580 cm^{-1} G peak. When $FeCl_3$-FLG is made, the p-doping has the effect of decreasing the Fermi level. Transitions between valence and conduction bands require higher energy, and therefore higher energy photons are emitted, resulting in a blue-shift of the G peak.

The D peak arises due to a double resonance second order process. In order to happen at all a defect must be present to allow for elastic scattering. The incident photon promotes an electron once again, the electron is now scattered a second time off a transverse optical (TO) phonon to near the K' point. The electron scatters elastically off a defect, back to the K point, where it recombines with a hole, emitting the scattered photon. This is seen in Figure 3.9 (b).

The 2D peak also arises due to a second order process, but in either a double or triple resonance. An incoming photon scatters an electron to the conduction band near the K point. A TO phonon then scatters it to the K' point. In the double resonance case the electron scatters off another TO phonon, back to the K point, where it recombines with a hole, emitting the scattered photon. In the triple resonance case rather than scattering off a second TO phonon at the K' point, the hole scatters off a TO phonon, to the K' point. The electron and hole now combine here. This is visualised in Figure 3.9 (c).

The 2D peak is of particular interest because of how it changes with the number of graphene layers. In the 2LG and 3LG cases the number of levels can be quickly inferred. For 2LG (Figure 3.10) there are 4 possible transitions which can be fitted to the peak. In 3LG there are 6. As more layers are added the peak moves towards the 2 peak structure of graphite.

3.3.2.2.3 *Raman on $FeCl_3$-FLG*

The primary reason for using Raman on $FeCl_3$-FLG is to measure the level of doping. This is done by analysing the G peak. In pristine FLG the G peak is at 1580 cm^{-1}, when $FeCl_3$ doped this G peak is blue-shifted as far as 1625 cm^{-1}.[65] This blue-

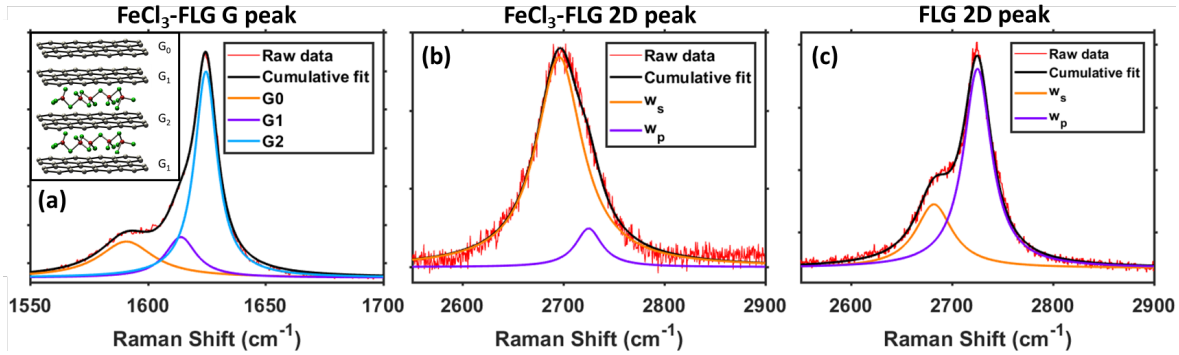

Figure 3.11: **(a)** Raman spectra of $FeCl_3$-FLG. The cumulative fit is the convolution of G peaks which arise from each stage. Staging refers to the number of SLG layers between each intercalate layer. When the there is no $FeCl_3$ present, a G_0 peak is observed. In stage 2, where there are 2 SLG layers between each $FeCl_3$ layer, the G_1 peak is observed. In stage 1, where there is 1 SLG layer between each $FeCl_3$ layer, the G_2 peak is observed. **(b)** 2D peak of $FeCl_3$-FLG showing the single peak structure associated with SLG. **(c)** 2D peak of FLG showing a 2 peak structure more associated with bulk graphite. w_s, w_p refer to the characteristic graphite 2D peak, and its shoulder, respectively.[64]

shifting happens in stages, reaching 1625 cm^{-1} only when full stage 2 intercalation is achieved. Intercalations which do not result in full stage 2 doping result in a convolution of peaks.[3;65]

Staging in $FeCl_3$-FLG refers to the number of graphene layers between each layer of intercalate.[3] When there is no $FeCl_3$ present, the G peak, known as G_0, occurs at 1580 cm^{-1}. In stage 2 there are two graphene layers between each $FeCl_3$ layer, the graphene layer is interacting with the $FeCl_3$ on only one side, the G peak, now the G_1, occurs at 1612 cm^{-1}. In stage 1 there is one graphene layer between each $FeCl_3$ layer, the graphene layer is interacting with the $FeCl_3$ on both sides, the G peak, now the G_2, occurs at 1625 cm^{-1}. The staging and resultant peaks are shown in Figure 3.11 (a). Knowing the staging is important for knowing the charge carrier density, and hence doping. To achieve maximum doping, maximum $FeCl_3$ intercalation is required, this is achieved when stage 1 is dominant. This means the G peak blue-shift can be used as a proxy for doping level.[65]

The 2D peak is also affected in $FeCl_3$-FLG. When $FeCl_3$ gets between the graphene layers the interaction between layers is decoupled. This results in the 2D peak reverting

back to that of SLG. As $FeCl_3$-FLG typically starts with 5 - 10 layer FLG, the shift in this peak has been seen before and after intercalation in mechanically exfoliated samples.[61] This is another useful way of characterising $FeCl_3$-FLG doping level.[60;65;66] I observed this effect also in nickel grown CVD FLG for the first time. Because of a combination of small multi-layer domains, and the staging effect where some parts of the graphene may be stage 1 or 2, this will result in a 2D peak which does not fully match that of pristine mechanically exfoliated graphene, unless full stage 1 intercalation is achieved. The 2D peak will usually have multiple contributions from SLG to 10LG. However with majority decoupling, the peak will migrate towards that of SLG (Figure 3.11 (b)). In the unintercalated FLG the peak remains more like graphite, as expected (Figure 3.11 (c)).

3.3.2.3 *Transmittance*

The third way in which TCE materials are optically characterised is to measure the materials transmittance properties. transmittance measurements are taking using a custom-build multi-purpose microscope,[48] the same one that is used to take Raman measurements, this can be seen in Figure 3.7 (a) & (b). White light from an LED light source is collimated and transmitted through the sample, and this is sent to the spectrometer. The spectrometer measures the intensity of light from 420 nm to 900 nm. The measurement itself starts by taking a calibration measurement, this is on the clean material substrate. The intensity of this is $I_{substrate}(\lambda)$. The sample is then measured, the value recorded is $I_{sample}(\lambda)$. The transmittance of the sample, $T_{sample}(\lambda)$ can be simply calculated:

$$T_{sample}(\lambda) = \frac{I_{sample}(\lambda)}{I_{substrate}(\lambda)} \tag{3.7}$$

The reported figure in literature is most commonly $T(\lambda)$ where $\lambda = 550\ nm$.[67]

3.3.3 *Surface characterisation*

Surface characterisation is extremely important when dealing with materials for thin film devices like OLEDs. These devices are comprised of several stacked layers, 5 - 200 nm thick. Any surface contaminants, or large surface roughness can be enough to puncture through multiple layers and short circuit the device. While contaminants can

be reduced through rigorous cleaning, the inherent material properties such as surface roughness are more difficult to control.

3.3.3.1 *Profiler measurements*

The first surface characterisation technique used is profilometry. Here a sharp probe tip is touched down onto the sample. A laser shines on the top of the probe and reflects onto a sensor. The sample is moved along a single axis and the probe tip drags over the sample surface as it goes. The laser light is deflected by the probe as it undulates over the samples surface. A KLA Tencor Alpha D-100 Profilometer was used for measurements taken in this work. Profilometry works only in 2D, the sample is moved along the x-axis, while the probe tip is displaced in the y-axis. The resulting profile is that of a single line of the sample. This is a very effective way of measuring step height. The profilometer is calibrated using a reference before every use. Here a step of 1 μm is used as reference. When the samples thickness is measured, a material is first coated onto a cleaned glass slide using the typical procedure for that material. The material is scratched away in the centre to leave a clean step. The sample is placed under the probe tip and measured multiple times. The step height is averaged to ensure accuracy of the result. This technique allows reliable measurements on materials which are > 20 nm in thickness. The surface roughness of the line could also be calculated, but in this work, it is not as more accurate roughness values are calculated exclusively from atomic force microscopy (AFM) measurements.

3.3.3.2 *Atomic force microscopy*

The general principle of AFM is like that of profilometry. In the case of AFM an atomically sharp probe tip is brought close or into contact with the sample. The probe is raster scanned in lines over the sample and is displaced due to the samples surface. Many lines are drawn on the sample to make up an image. The samples used usually draw 256 lines. The probe has a laser pointed at its back side, this laser reflects and points at a charge-coupled device (CCD) sensor. The sensor can measure the displacement in both x and y. This can be seen in Figure 3.12. A suite of feedback electronics adjusts the probe to ensure the laser remains pointed at the CCD. The two primary modes of operation for AFM are tapping mode and contact mode, contact

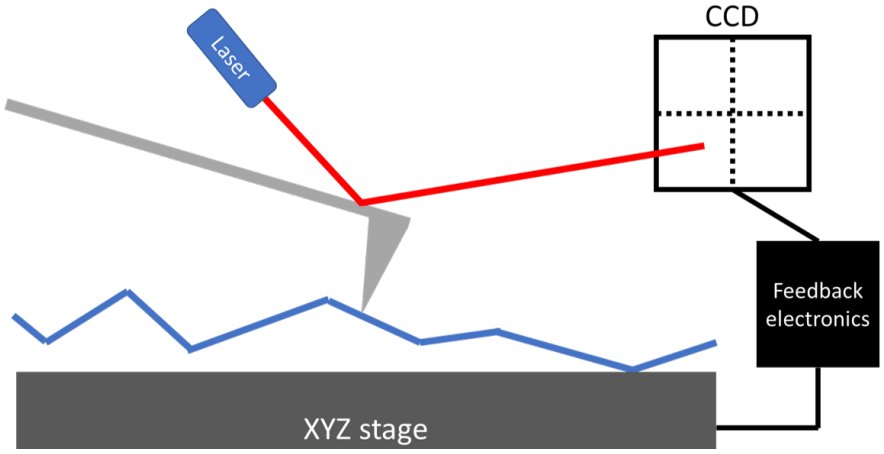

Figure 3.12: The working principle of an AFM. A probe tip is rastered across a sample, this causes the reflected laser light to move around on the CCD. The stage is adjusted to ensure the laser remains on the CCD. An image is built up from rastering lines.

mode has just been described. In tapping mode, the cantilevered probe tip is set oscillating at its resonant frequency. As the tip comes close to the sample surface it is attracted by Van der Walls interactions. The oscillation frequency is distorted by this and image can be built up by rastering using this process. One of the main attractions of tapping mode is that it reduces contact with the sample, preventing damage in fragile samples.

BIBLIOGRAPHY

[1] Xuelei Liang, Brent A. Sperling, Irene Calizo, Guangjun Cheng, Christina Ann Hacker, Qin Zhang, Yaw Obeng, Kai Yan, Hailin Peng, Qiliang Li, Xiaoxiao Zhu, Hui Yuan, Angela R. Hight Walker, Zhongfan Liu, Lian Mao Peng, and Curt A. Richter. Toward clean and crackless transfer of graphene. *ACS Nano*, 5(11):9144–9153, 11 2011.

[2] D. Kireev, D. Sarik, T. Wu, X. Xie, B. Wolfrum, and A. Offenhäusser. High throughput transfer technique: Save your graphene. *Carbon*, 107:319–324, 10 2016.

[3] M. S. Dresselhaus and G. Dresselhaus. Intercalation compounds of graphite. *Advances in Physics*, 51(1):1–186, 1 2002.

[4] Dominique Joseph Wehenkel, Thomas Hardisty Bointon, Tim Booth, Peter Bøggild, Monica Felicia Craciun, and Saverio Russo. Unforeseen high temperature and humidity stability of FeCl3 intercalated few layer graphene. *Scientific Reports*, 5(1):7609, 7 2015.

[5] A.K. van der Vegt & L.E. Govaert. van keten tot kunstof. *Uniwersytet śląski*, 2003.

[6] Sukang Bae, Hyeongkeun Kim, Youngbin Lee, Xiangfan Xu, Jae Sung Park, Yi Zheng, Jayakumar Balakrishnan, Tian Lei, Hye Ri Kim, Young Il Song, Young Jin Kim, Kwang S. Kim, Barbaros Özyilmaz, Jong Hyun Ahn, Byung Hee Hong, and Sumio Iijima. Roll-to-roll production of 30-inch graphene films for transparent electrodes. *Nature Nanotechnology*, 5(8):574–578, 8 2010.

[7] C. W. Tang and S. A. Vanslyke. Organic electroluminescent diodes. *Applied Physics Letters*, 51(12):913–915, 9 1987.

[8] Alastair Buckley. *Organic Light-Emitting Diodes (OLEDs): Materials, Devices and Applications*. 2013.

[9] Bernard Geffroy, Philippe le Roy, and Christophe Prat. Organic light-emitting diode (OLED) technology: Materials, devices and display technologies. *Polymer International*, 55(6):572–582, 6 2006.

[10] Jayanta Bauri, Ram Bilash Choudhary, and Gobind Mandal. Recent advances in efficient emissive materials-based OLED applications: a review. *Journal of Materials Science*, 56(34):18837–18866, 9 2021.

[11] Seunghwan Lee, Ju Hwan Han, Seong Hyeon Lee, Geon Ho Baek, and Jin Seong Park. Review of Organic/Inorganic Thin Film Encapsulation by Atomic Layer Deposition for a Flexible OLED Display. *JOM*, 71(1):197–211, 1 2019.

[12] P. E. Burrows, V. Bulovic, S. R. Forrest, L. S. Sapochak, D. M. McCarty, and M. E. Thompson. Reliability and degradation of organic light emitting devices. *Applied Physics Letters*, 65(23):2922–2924, 6 1994.

[13] Li Ping Lu, Dinesh Kabra, and Richard H. Friend. Barium hydroxide as an interlayer between zinc oxide and a luminescent conjugated polymer for light-emitting diodes. *Advanced Functional Materials*, 22(19):4165–4171, 10 2012.

[14] M. S. Zaini, M. A.Mohd Sarjidan, and W. H.Abd Majid. Determination of Traps' Density of State in OLEDs from Current-Voltage Analysis. *Chinese Physics Letters*, 33(1):018101, 1 2016.

[15] Christopher R. McNeill and Neil C. Greenham. Conjugated-polymer blends for optoelectronics. *Advanced Materials*, 21(38-39):3840–3850, 10 2009.

[16] Yuan Zhang and Paul W.M. Blom. Electron and hole transport in poly(fluorene-benzothiadiazole). *Applied Physics Letters*, 98(14):143504, 4 2011.

[17] OPV and OLED Fabrication — How to Make Organic Solar Cells — Ossila.

[18] Bo Ram Lee, Eui Dae Jung, Ji Sun Park, Yun Seok Nam, Sa Hoon Min, Byeong Su Kim, Kyung Min Lee, Jong Ryul Jeong, Richard H. Friend, Ji Seon Kim, Sang Ouk Kim, and Myoung Hoon Song. Highly efficient inverted polymer light-emitting diodes using surface modifications of ZnO layer. *Nature Communications*, 5(1):1–8, 9 2014.

[19] Yasuo Nakayama, Katsuyuki Morii, Yuuichirou Suzuki, Hiroyuki Machida, Satoshi Kera, Nobuo Ueno, Hiroshi Kitagawa, Yutaka Noguchi, and Hisao Ishii. Origins of improved hole-injection efficiency by the deposition of MoO 3 on the polymeric semiconductor poly(dioctyifluorene-alt-benzothiadiazole). *Advanced Functional Materials*, 19(23):3746–3752, 12 2009.

[20] M. Kröger, S. Hamwi, J. Meyer, T. Riedl, W. Kowalsky, and A. Kahn. Role of the deep-lying electronic states of MoO3 in the enhancement of hole-injection in organic thin films. *Applied Physics Letters*, 95(12):123301, 9 2009.

[21] Yiling Wang, Qun Luo, Na Wu, Qiankun Wang, Hongfei Zhu, Liwei Chen, Yan Qing Li, Liqiang Luo, and Chang Qi Ma. Solution-processed MoO3:PEDOT:PSS hybrid hole transporting layer for inverted polymer solar cells. *ACS Applied Materials and Interfaces*, 7(13):7170–7179, 2015.

[22] Yijie Xia and Shuyang Dai. Review on applications of PEDOTs and PEDOT:PSS in perovskite solar cells. *Journal of Materials Science: Materials in Electronics*, 32(10):12746–12757, 5 2021.

[23] W. M.H. Sachtler, G. J.H. Dorgelo, and A. A. Holscher. The work function of gold. *Surface Science*, 5(2):221–229, 10 1966.

[24] Young Hoon Kim, Tae Hee Han, Himchan Cho, Sung Yong Min, Chang Lyoul Lee, and Tae Woo Lee. Polyethylene imine as an ideal interlayer for highly efficient inverted polymer light-emitting diodes. *Advanced Functional Materials*, 24(24):3808–3814, 6 2014.

[25] Electron Transport Material — High Performance — Supplier.

[26] Yulong Shen, Ahmad R. Hosseini, Man Hoi Wong, and George G. Malliaras. How to make ohmic contacts to organic semiconductors. *ChemPhysChem*, 5(1):16–25, 1 2004.

[27] G. G. Malliaras and J. C. Scott. The roles of injection and mobility in organic light emitting diodes. *Journal of Applied Physics*, 83(10):5399–5403, 4 1998.

[28] Michael Hengge, Konstantin Livanov, Natalia Zamoshchik, Felix Hermerschmidt, and Emil J.W. List-Kratochvil. ITO-free OLEDs utilizing inkjet-printed and low temperature plasma-sintered Ag electrodes. *Flexible and Printed Electronics*, 6(1):015009, 2 2021.

[29] PFO Polymer F8 for Organic Electronics — 19456-48-5 — Ossila.

[30] Bruno G.A.L. Borges, Amanda G. Veiga, Maria Gioti, Argiris Laskarakis, Lazaros Tzounis, Stergios Logothetidis, and Maria Luiza M. Rocco. Surface, interface and electronic properties of F8:F8BT polymeric thin films used for organic light-emitting diode applications. *Polymer International*, 67(6):691–699, 6 2018.

[31] M. Gioti. Optical, photophysical, and electrooptical studies on slot-die polyfluorene-based flexible OLED devices. *Optical Materials Express*, 11(5):1442, 5 2021.

[32] Ayse Turak. On the Role of LiF in Organic Optoelectronics. *Electronic Materials*, 2(2):198–221, 6 2021.

[33] Daniel Ping Kuen Tsang and Chihaya Adachi. Operational stability enhancement in organic light-emitting diodes with ultrathin Liq interlayers. *Scientific Reports*, 6(1):1–10, 3 2016.

[34] C. Schmitz, H. W. Schmidt, and M. Thelakkat. Lithiumr-quinolate complexes as emitter interface materials in organic light-emitting diodes. *Chemistry of Materials*, 12(10):3012–3019, 2000.

[35] Buwen Xiao, Bing Yao, Chunsheng Ma, Shiyong Liu, Zhiyuan Xie, and Lixiang Wang. Highly efficient top-emitting organic light-emitting devices with aluminium electrodes. *Semiconductor Science and Technology*, 20(9):952–955, 8 2005.

[36] Edgar William John Mitchell and John Wesley Mitchell. The work functions of copper, silver and aluminium. In *Proceedings of the Royal Society of London. Series A. Mathematical and Physical Sciences*, volume 210, pages 70–84. The Royal Society London, 12 1951.

[37] TFB Polymer for OLEDs & Devices — 220797-16-0 — Ossila.

[38] Shugo Sato, Satoru Ohisa, Yukihiro Hayashi, Ryo Sato, Daisuke Yokoyama, Tetsuya Kato, Michinori Suzuki, Takayuki Chiba, Yong Jin Pu, and Junji Kido. Air-Stable and High-Performance Solution-Processed Organic Light-Emitting Devices Based on Hydrophobic Polymeric Ionic Liquid Carrier-Injection Layers. *Advanced Materials*, 30(18), 5 2018.

[39] Hui Shi, Congcong Liu, Qinglin Jiang, and Jingkun Xu. Effective Approaches to Improve the Electrical Conductivity of PEDOT:PSS: A Review. *Advanced Electronic Materials*, 1(4):1500017, 4 2015.

[40] Taegeon Kim, Ali Canlier, Geun Hong Kim, Jaeho Choi, Minkyu Park, and Seung Min Han. Electrostatic spray deposition of highly transparent silver nanowire electrode on flexible substrate. *ACS Applied Materials and Interfaces*, 5(3):788–794, 2 2013.

[41] J. Duch, P. Kubisiak, K. H. Adolfsson, M. Hakkarainen, M. Golda-Cepa, and A. Kotarba. Work function modifications of graphite surface via oxygen plasma treatment. *Applied Surface Science*, 419:439–446, 10 2017.

[42] Ki Chang Kwon, Wan Jae Dong, Gwan Ho Jung, Juyoung Ham, Jong Lam Lee, and Soo Young Kim. Extension of stability in organic photovoltaic cells using UV/ozone-treated graphene sheets. *Solar Energy Materials and Solar Cells*, 109:148–154, 2 2013.

[43] Kieran Kane Walsh. *Ultra-Lightweight Energy Harvesting Devices Based on FeCl 3 Intercalated Few Layer Graphene Electrodes*. PhD thesis, 11 2021.

[44] Yong Seob Park, Eungkwon Kim, Byungyou Hong, and Jaehyoeng Lee. Characteristics of ITO films with oxygen plasma treatment for thin film solar cell applications. *Materials Research Bulletin*, 48(12):5115–5120, 12 2013.

[45] Zhong Zhi You and Jiang Ya Dong. Oxygen plasma treatment effects of indium-tin oxide in organic light-emitting devices. *Vacuum*, 81(7):819–825, 2 2007.

[46] Haldor Topsoe Semiconductor Division. Geometric factors in four point resistivity measurement. Bulletin No. 472-13. Technical Report 13, Haldor Topsoe Semiconductor Devision, 1966.

[47] L. J. van der Pauw. A method of measuring specific resistivity and Hall effect of disks of arbitrary shape. In *Semiconductor Devices: Pioneering Papers*, pages 174–182. WORLD SCIENTIFIC, 3 1958.

[48] Adolfo De Sanctis, Gareth F Jones, Nicola J Townsend, Monica F Craciun, and Saverio Russo. An integrated and multi-purpose microscope for the characterization of atomically thin optoelectronic devices. *Review of Scientific Instruments*, 88(5), 2017.

[49] Derek. J Gardinder and Pierre. R Graves. *Practical Raman Spectroscopy*. Springer Berlin Heidelberg, 1989.

[50] Fernando Cerdeira and Manuel Cardona. Effect of carrier concentration on the raman frequencies of Si and Ge. *Physical Review B*, 5(4):1440–1454, 2 1972.

[51] C. V. Raman and K. S. Krishnan. A new type of secondary radiation [11]. *Nature*, 121(3048):501–502, 1928.

[52] Andrea C Ferrari and Denis M Basko. Raman spectroscopy as a versatile tool for studying the properties of graphene. *Nature Nanotechnology*, 8(4):235–246, 2013.

[53] L. G. Cançado, A. Jorio, E. H.Martins Ferreira, F. Stavale, C. A. Achete, R. B. Capaz, M. V.O. Moutinho, A. Lombardo, T. S. Kulmala, and A. C. Ferrari. Quantifying defects in graphene via Raman spectroscopy at different excitation energies. *Nano Letters*, 11(8):3190–3196, 8 2011.

[54] Ying Ying Wang, Zhen Hua Ni, Ting Yu, Ze Xiang Shen, Hao Min Wang, Yi Hong Wu, Wei Chen, and Andrew Thye Shen Wee. Raman studies of monolayer graphene: The substrate effect. *Journal of Physical Chemistry C*, 112(29):10637–10640, 7 2008.

[55] Ryan Beams, Luiz Gustavo Cançado, and Lukas Novotny. Raman characterization of defects and dopants in graphene. *Journal of Physics Condensed Matter*, 27(8):083002, 1 2015.

[56] T. M.G. Mohiuddin, A. Lombardo, R. R. Nair, A. Bonetti, G. Savini, R. Jalil, N. Bonini, D. M. Basko, C. Galiotis, N. Marzari, K. S. Novoselov, A. K. Geim, and A. C. Ferrari. Uniaxial strain in graphene by Raman spectroscopy: G peak splitting, Grüneisen parameters, and sample orientation. *Physical Review B - Condensed Matter and Materials Physics*, 79(20):205433, 5 2009.

[57] Michele Lazzeri and Francesco Mauri. Nonadiabatic Kohn anomaly in a doped graphene monolayer. *Physical Review Letters*, 97(26):266407, 12 2006.

[58] Ji Eun Lee, Gwanghyun Ahn, Jihye Shim, Young Sik Lee, and Sunmin Ryu. Optical separation of mechanical strain from charge doping in graphene. *Nature Communications*, 3, 2012.

[59] Felix Herziger, Patrick May, and Janina Maultzsch. Layer-number determination in graphene by out-of-plane phonons. *Physical Review B - Condensed Matter and Materials Physics*, 85(23):235447, 6 2012.

[60] A C Ferrari, J C Meyer, V Scardaci, C Casiraghi, M Lazzeri, F Mauri, S Piscanec, D Jiang, K S Novoselov, S Roth, and A K Geim. Raman spectrum of graphene and graphene layers. *Physical Review Letters*, 97(18), 2006.

[61] Ivan Khrapach, Freddie Withers, Thomas H. Bointon, Dmitry K. Polyushkin, William L. Barnes,

Saverio Russo, and Monica F. Craciun. Novel highly conductive and transparent graphene-based conductors. *Advanced Materials*, 24(21):2844–2849, 6 2012.

[62] Tuinstra F and Koeing JL. Raman spectrum of graphite. *Journal of Chemical Physics*, 53(3):1126–1130, 9 1970.

[63] L. M. Malard, M. A. Pimenta, G. Dresselhaus, and M. S. Dresselhaus. Raman spectroscopy in graphene. *Physics Reports*, 473(5-6):51–87, 4 2009.

[64] Keith R. Paton, Eswaraiah Varrla, Claudia Backes, Ronan J. Smith, Umar Khan, Arlene O'Neill, Conor Boland, Mustafa Lotya, Oana M. Istrate, Paul King, Tom Higgins, Sebastian Barwich, Peter May, Pawel Puczkarski, Iftikhar Ahmed, Matthias Moebius, Henrik Pettersson, Edmund Long, João Coelho, Sean E. O'Brien, Eva K. McGuire, Beatriz Mendoza Sanchez, Georg S. Duesberg, Niall McEvoy, Timothy J. Pennycook, Clive Downing, Alison Crossley, Valeria Nicolosi, and Jonathan N. Coleman. Scalable production of large quantities of defect-free few-layer graphene by shear exfoliation in liquids. *Nature Materials*, 13(6):624–630, 6 2014.

[65] Weijie Zhao, Ping Heng Tan, Jian Liu, and Andrea C Ferrari. Intercalation of few-layer graphite flakes with FeCl3: Raman determination of Fermi level, layer by layer decoupling, and stability. *Journal of the American Chemical Society*, 133(15):5941–5946, 2011.

[66] Andrea C. Ferrari. Raman spectroscopy of graphene and graphite: Disorder, electron-phonon coupling, doping and nonadiabatic effects. *Solid State Communications*, 143(1-2):47–57, 7 2007.

[67] Sukanta De and Jonathan N. Coleman. Are there fundamental limitations on the sheet resistance and transmittance of thin graphene films? *ACS Nano*, 4(5):2713–2720, 5 2010.

4

EXPERIMENTAL DEVELOPMENT

4.1 INTRODUCTION

The purpose of this chapter is to present the work I did in developing experimental methods and experimental apparatus used throughout this work. At the outset of this project organic light-emitting diodes (OLEDs) had not been fabricated or characterised in the research group before. Therefore, fabrication had to be developed, using methods from the literature, and further optimised for the equipment available.

The characterisation of OLEDs also needs to be developed. As such a luminance measurement apparatus is built to characterise the device performance, an emission angle apparatus is built to estimate device external quantum efficiency (EQE), and two different types of device/substrate benders are built to evaluate bending performance. This chapter will introduce all three of these characterisation tools.

Apart from the development of the fabrication and characterisation procedures for OLEDs, there is a significant amount of material optimisation that needs to be done. The primary areas where optimisation is required is in scaling up the $FeCl_3$ intercalated FLG ($FeCl_3$-FLG) for use in 12×12 mm devices and optimising the layer thicknesses of the OLED layers. This work is all critical to realising working OLEDs in the two structures discussed.

Finally, in relation to scaling up the $FeCl_3$-FLG, there is the need to develop appropriate Raman characterisation procedures in the form of a Raman mapping methodology.

4.2 RAMAN MAPPING DEVELOPMENT

Some data contained within this section and Section 4.3 has been subject to publication: *"Wafer scale $FeCl_3$ intercalated graphene electrodes for photovoltaic applications."* Kieran K Walsh, Conor Murphy, Gareth Jones, Matthew Barnes, Adolfo De Sanctis, Dong-Wook Shin, Saverio Russo, Monica Craciun. Proc. SPIE 10688, Photonics for Solar Energy Systems VII, 106881C (2018); DOI: 10.1117/12.2307410.

$FeCl_3$-FLG is a patchwork of few-layer domains. This can be seen in Figure 4.1 (a). These range from 1-10 layers thick. When taking a single Raman spectrum, the laser spot has a radius of 1 μm, the domains have a radius of 5 - 10 μm. This means single spectra do not provide a general overview of the large-scale sample. To get a better picture of the doping across the entire sample mapping is necessary.

Mapping typically involves taking a spectrum at every point on the sample,[1] however as the samples sometimes have holes or defects this could also result in a false impression of the doping level. To overcome this, a spectrum was taken with a 1 μm radius 514 nm laser spot every 10 μm. 10 μm ensures each laser spot only measures each domain approximately once.

When this is done the map produced is more representative of the sample as a whole. This will result in better correlation to the doping level, and therefore sheet resistance of the sample. The mapping done in this way can be seen in Figure 4.1 (a) & (b). While the map does not reproduce any film morphology features in the sample area, it gives a better picture of doping. The map can then be summarised better with the histogram shown in Figure 4.1 (c). Here it can be seen, that for this sample stage 2 doping is the dominant form of doping, with stage 1 not reached at all in this case.

When comparing samples, it is useful to have a single number that can be compared. In this case we proposed using the mean $< PosG >$.[2] $< PosG >$ is the area weighted G peak position, this gives the average G peak position by summing the position of the G_0, G_1, and G_2 peaks weighted by their area and then normalising this value to the total area of the G peak, as shown in Equation 4.1.

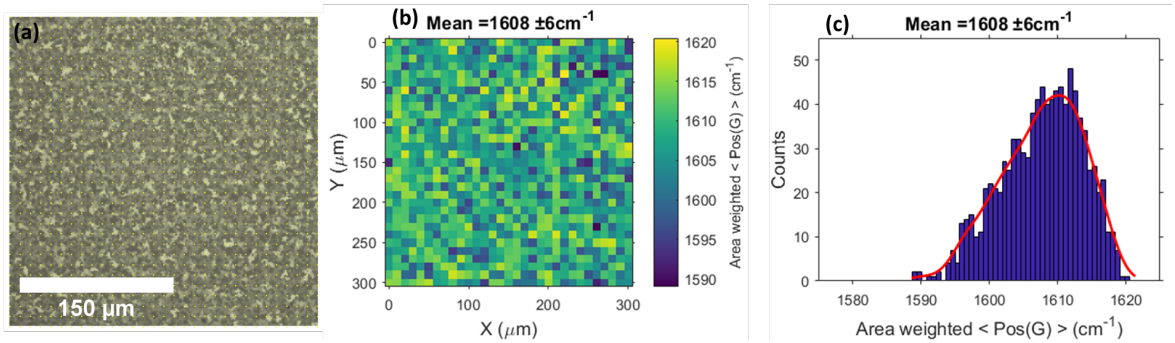

Figure 4.1: **(a)** Optical image of $FeCl_3$-FLG. The domains of FLG can be clearly seen. The lighter regions have more layers. Tiny yellow dots show where Raman spectra are taken. **(b)** Raman map of $FeCl_3$-FLG. Lighter points indicate a higher level of doping. Each point corresponds to the average peak location for each spectrum. The mean peak position is used as a proxy for doping level. **(c)** A histogram of the map. Shows clearly that most points are intercalated to stage 1.

$$< PosG >= \frac{PosG_0 \frac{AreaG_0}{2} + PosG_1 AreaG_1 + PosG_2 AreaG_2}{\frac{AreaG_0}{2} + AreaG_1 + AreaG_2} \tag{4.1}$$

Here $PosG_n$ refers to the Raman shift position in cm^{-1}, and $AreaG_n$ is the area of the peak. The factor 1/2 in the $AreaG_0$ terms arises because of the reduction in the full width at half maximum (FWHM) of the G peak by approximately 1/2 due to increasing charge carrier concentration to 3×10^{13} cm^{-2}.[3]

Traditional mapping can also be used to verify this approach. A traditional map is made when taking 1 μm spectra and stepping only 1 μm. Here features are visible, and it is possible to correlate regions of single layer graphene (SLG) or holes in the film with poor intercalation staging and low charge carrier concentration. This was done successfully in Walsh et al.[2] Here we were able to correlate a hole in the $FeCl_3$-FLG sample with poor charge carrier concentration by making use of a model developed by Lazzeri et al.[4]. This can be seen in Figure 4.2.

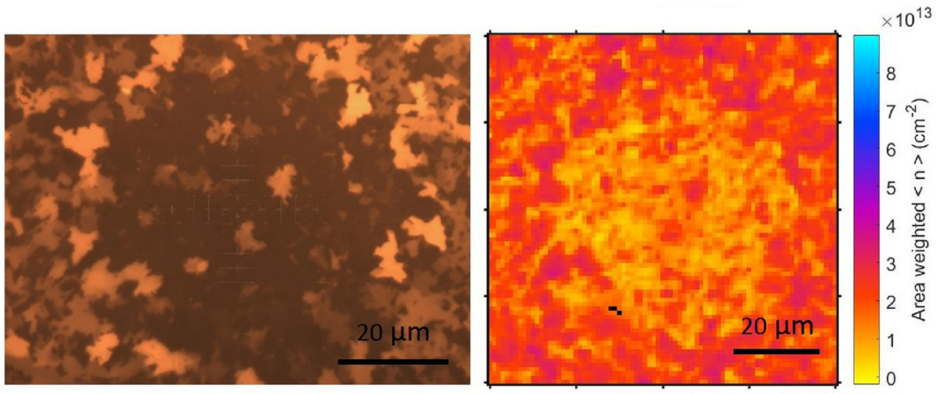

Figure 4.2: Left: Optical image of a hole in the FLG patchwork. **Right:** A map of the charge carrier concentration, derived from the Raman map $< PosG >$ data based on the model developed by Lazzeri et al.[4] The hole in the sample is clearly visible by the drop in charge carrier concentration. Reproduced with permission.[2]

4.3 LARGE AREA FECL$_3$-FLG OPTIMISATION

The $FeCl_3$-FLG used in this project is based on that discovered and fully characterised on the micron scale.[5] The $FeCl_3$-FLG used in this work, intercalated chemical vapour deposition (CVD) graphene grown on nickel, was introduced later.[1] A significant part of this project was to scale up and optimise $FeCl_3$-FLG for use in large area OLED devices, up to wafer scale. On the micron scale it was known that $FeCl_3$-FLG demonstrates its best electrical conductivity when it is 5 layers thick and fully intercalated. Sheet resistances of 8.8 $\Omega/\square$, and optical transmittance at 550 nm of 84% has been reported.[5] It is important to recreate, as close as possible, these results on a much larger scale.

4.3.1 *Large area transfer*

One of the first issues with large scale $FeCl_3$-FLG is the starting material. Few-layer graphene (FLG) was purchased from Graphene Supermarket, it is then transferred to glass and intercalated with $FeCl_3$. The quality of the material received was often low. Holes can be visible to the naked eye. Figure 4.3 (a) shows two types of holes that are often present. The larger holes are visible to the naked eye and measure ≈ 0.5 mm in diameter. These holes show some intercalated domains within them; however, they are separated from one another, meaning they will not take part in conduction across the

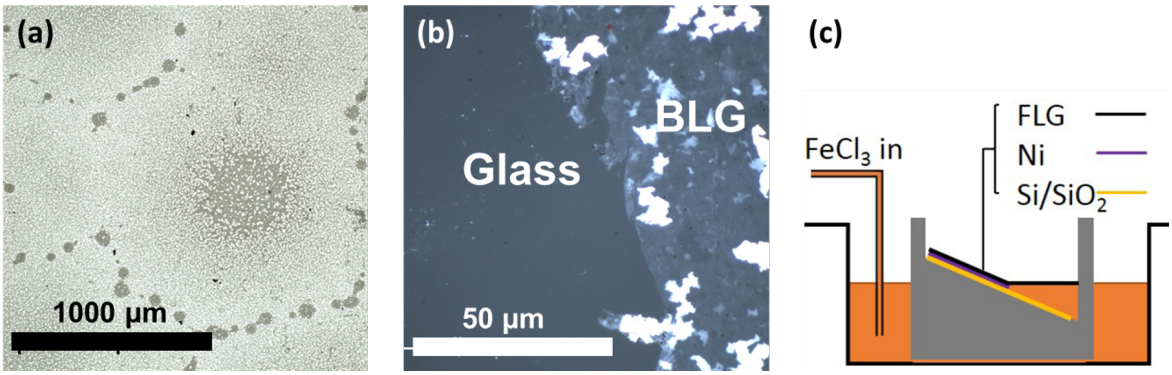

Figure 4.3: **(a)** Optical microscope image of the holes that appear in nickel grown FLG. The large hole is visible to the naked eye. **(b)** An image of the sample edge. Here the bilayer can be clearly seen alongside the bare glass substrate. This image was taken in a large hole so the bi-layer would not be obscured by few-layer domains. **(c)** A schematic of the wet transfer procedure. FLG is etched from its growth substrate, leaving it floating on the etchant surface. Reproduced with permission.[2]

film. These holes have been measured to take up as much as 18.5% of the FLG surface area. The second set of holes seen are much smaller at $\approx 50\ mm$ in diameter, these holes cannot be seen with the naked eye. These holes are devoid of any FLG domains and will therefore not conduct well. The only thing present here is the bilayer graphene (2LG) on which the few-layer graphene sheets grow in the CVD process.[6] The 2LG can be seen clearly in Figure 4.3 (b) alongside the glass substrate. Both types of holes will need to be eliminated by optimising the CVD growth procedure if $FeCl_3$-FLG is to be a viable replacement of indium tin oxide (ITO). This is not the purpose of this work; however, it is an issue that contributes to poor $FeCl_3$-FLG performance throughout. Obtaining high quality nickel grown FLG has been an issue throughout.

There are two etching methods used in this work, the manual fishing method (discussed in Section 3.2.1.1), and the automated large area method. The large area method is suited to samples which cannot float on the etchant because their weight breaks the surface tension. The large area method is significantly more stable and controlled, this prevents breakage of the FLG where the support layer is not strong enough. It also allows for a thinner support layer to be used which should reduce left over residues. The large area transfer process is visualised in Figure 4.3 (c), here a

poly(methyl 2-methylpropenoate) (PMMA) coated sample is placed on a chuck in a basin. The basin is slowly filled with etchant. The filling rate is equivalent to the etching rate. Once the FLG is floating free the etchant being pumped in is replaced with deionised (DI) water, and a drain pump in activated. These maintain the same volume of liquid, while the etchant concentration is continually reducing. Once the etchant is removed after several hours, the Si/SiO_2 is replaced with a glass substrate. The DI water is slowly pumped out, allowing the sample to settle on the glass substrate. The sample is dried in the same way as before. Finally, regardless of method the PMMA must be removed, this is done by placing the sample in an acetone bath at 60°C for several hours, with the acetone being replaced for fresh twice. The sample is finally rinsed in propan-2-ol (IPA) and blow dried with nitrogen.

4.3.2 *Large area intercalation*

The intercalation recipe (discussed in Section 3.2.1.2) also needs to be optimised for large-area samples. This intercalation recipe often resulted in samples whose sheet resistance was more than 300 $\Omega/\square$ for large area samples. Large area samples could also not be intercalated in the 3 *cm* diameter tube used previously. Therefore, the tube was replaced with a 9 *cm* diameter quartz tube, and the zone temperatures were optimised. The most important temperature to consider is the zone 1 temperature, T_1. T_1 was chosen to be 315°C as this is the known sublimation temperature of anhydrous $FeCl_3$. This temperature was not optimised for the setup in use here however, where it is likely that the temperature being read is not the true temperature at the powder, or where the temperature is even optimum. The powder temperature T_1 therefore varied to measure its effect on $FeCl_3$-FLG intercalation.

The metric used to assess intercalation is $< PosG >$, defined in Equation 4.1. This metric results from taking Raman maps of the samples and examining the G peak. T_1 was varied from 300 - 360°C to adjust the vapour pressure of the $FeCl_3$ vapour during intercalation. This is thought to influence the quality of intercalation as $FeCl_3$ molecules will be able to penetrate the graphene layers more easily at a higher pressure. The results in Figure 4.4 (a) show that the increasing T_1 from the previously used temperature of 315°C to 360°C caused an increase in the $< PosG >$ value from 1590 cm^{-1} to 1603 cm^{-1}. Although this value is lower than that quoted for $FeCl_3$-

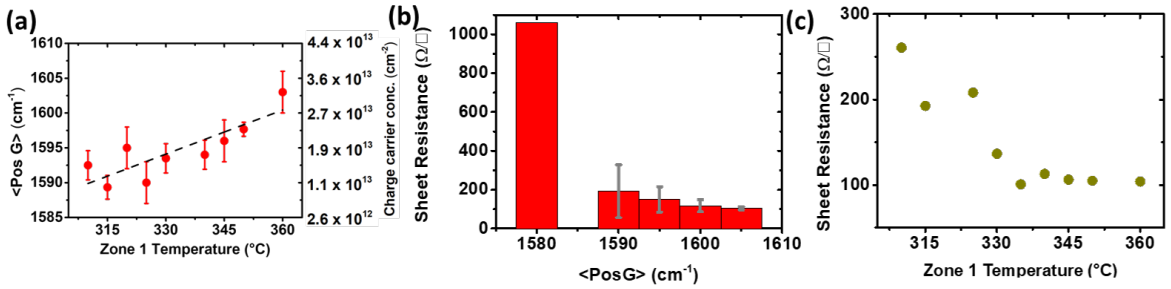

Figure 4.4: **(a)** Graph showing $< PosG >$ against powder temperature (T_1) and doping concentration. Reproduced with permission.[2] **(b)** Histogram showing sheet resistance of $FeCl_3$-FLG against $< PosG >$. Sheet resistance values are put in bins and the average is reported. **(c)** Graph showing sheet resistance of $FeCl_3$-FLG against the powder temperature, T_1.

FLG's G_1 peak because this metric considers the position of all the peaks, it can be shown that $< PosG > = 1603\ cm^{-1}$ relates to a G peak with all G_0, G_1, and G_2 sub-peaks present. This shows that some of the flakes present in the graphene film fully intercalate, while others do not.

Figure 4.4 (b) shows the relation between sheet resistance and $< PosG >$. Here all sheet resistances are put in bins according to their $< PosG >$ and averaged. Each bin is 5 cm^{-1} wide centred at every integer multiple of 5. The average sheet resistance of $FeCl_3$-FLG is significantly reduced for all stages of intercalation, from $\approx 1000\ \Omega/\square$ to $\approx 200\ \Omega/\square$. Higher $< PosG >$, indicating better intercalation, further reduces sheet resistance from $\approx 200\ \Omega/\square$ to $\approx 100\ \Omega/\square$. Significantly at higher stages of intercalation samples are more self-consistent. The standard deviation of sheet resistances between samples drops from $\approx 140\ \Omega/\square$ to $\approx 10\ \Omega/\square$ at higher stages of intercalation.

Figure 4.4 (c) shows the relation between the sheet resistance of $FeCl_3$-FLG and T_1 during intercalation. Here as expected from Figure 4.4 (a) & (b) there is a strong relation between sheet resistance and T_1. Sheet resistance clearly saturates at $T_1 = 345°C$. I decided to proceed at $T_1 = 350°C$. This ensures the sample will not get damaged upon cooling, while maintaining the better doping conditions of higher T_1. The aim was to ensure that the T_2 is always slightly higher than every other zone, this ensures that the cooling $FeCl_3$ vapour will not crystallize on the sample.

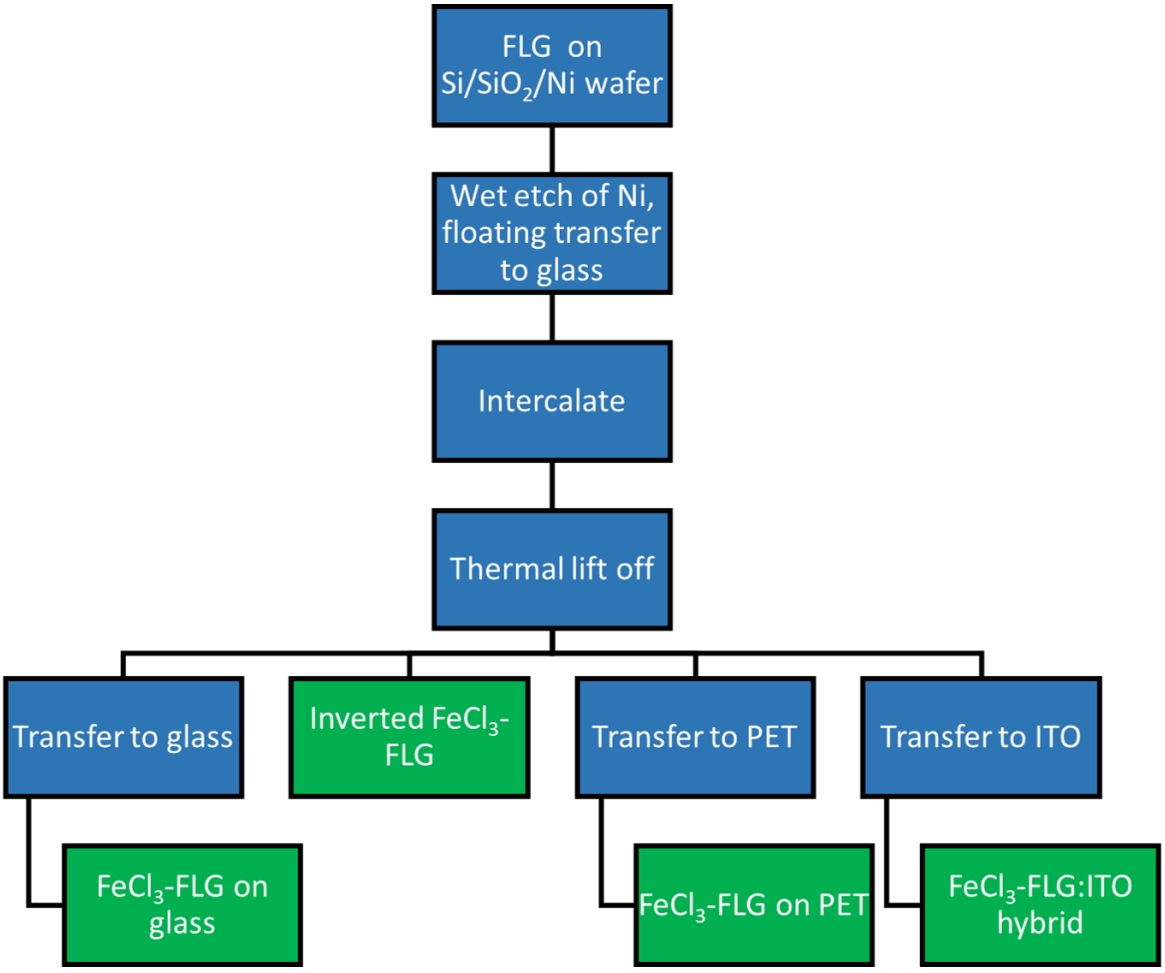

Figure 4.5: The process flow which leads to four types of graphene used in this thesis. $FeCl_3$-FLG on glass, inverted $FeCl_3$-FLG, $FeCl_3$-FLG on polyethylene terephthalate (PET), and $FeCl_3$-FLG enhanced ITO ($FeCl_3$-FLG:ITO)

4.3.3 *Laminator transfer*

4.3.3.1 *Introduction*

PMMA is used throughout this work as a support layer when transferring FLG or $FeCl_3$-FLG to new substrates. PMMA is a widely used support layer, but it has significant problems in relation to residue.[7] When PMMA is no longer needed it is dissolved in acetone, this removes most of the polymer, but leaves residues, capable of shorting a thin film device. The most common way to remove these residues is through thermal annealing.[7–9] This evaporates any remaining polymer molecules, removing them. This is only possible for materials and substrates which are compatible with high temperature. When $FeCl_3$-FLG is transferred to PET, thermal annealing is not an option.

A solution to this is to use a different polymer. One which is particularly attractive is one which can be dissolved in water. This is simpler, safer, cheaper, and more environmentally friendly. One such polymer is poly(vinyl alcohol) (PVA). It is safe to use and non-hazardous.[10] It is often used in hydro dipping.[11] Here a pattern can be printed onto water soluble PVA film, the film placed into water, and the film dissolves. This leaves the print floating on the water, held together by surface tension. An item can be dipped into the water, coating it in the print. It is this PVA film that is used.

The PVA film, designed for dipping transfers is already commercially available and designed to dissolve in water quickly. If the residues can be reduced compared to PMMA it could be a viable replacement. PVA films also have the added benefit of being able to be applied dry. They have been shown to be able to transfer SLG successfully from growth substrate to glass with minimal residues.[12] The dry transfer in the past made use of a laminator, heating the substrate to 110°C while rolling and applying pressure, this fuses it to the SLG, the PVA and SLG can then simply be peeled off the growth substrate.[12]

4.3.3.2 *Layer-by-layer $FeCl_3$-FLG*

In this work all the $FeCl_3$-FLG is fabricated from Ni grown FLG. This is well suited to intercalation because it is approximately 5 layers thick. One of the drawbacks however of using FLG grown in this way is its low transmittance, small domain size, and high surface roughness. Copper grown graphene is generally regarded as superior to nickel

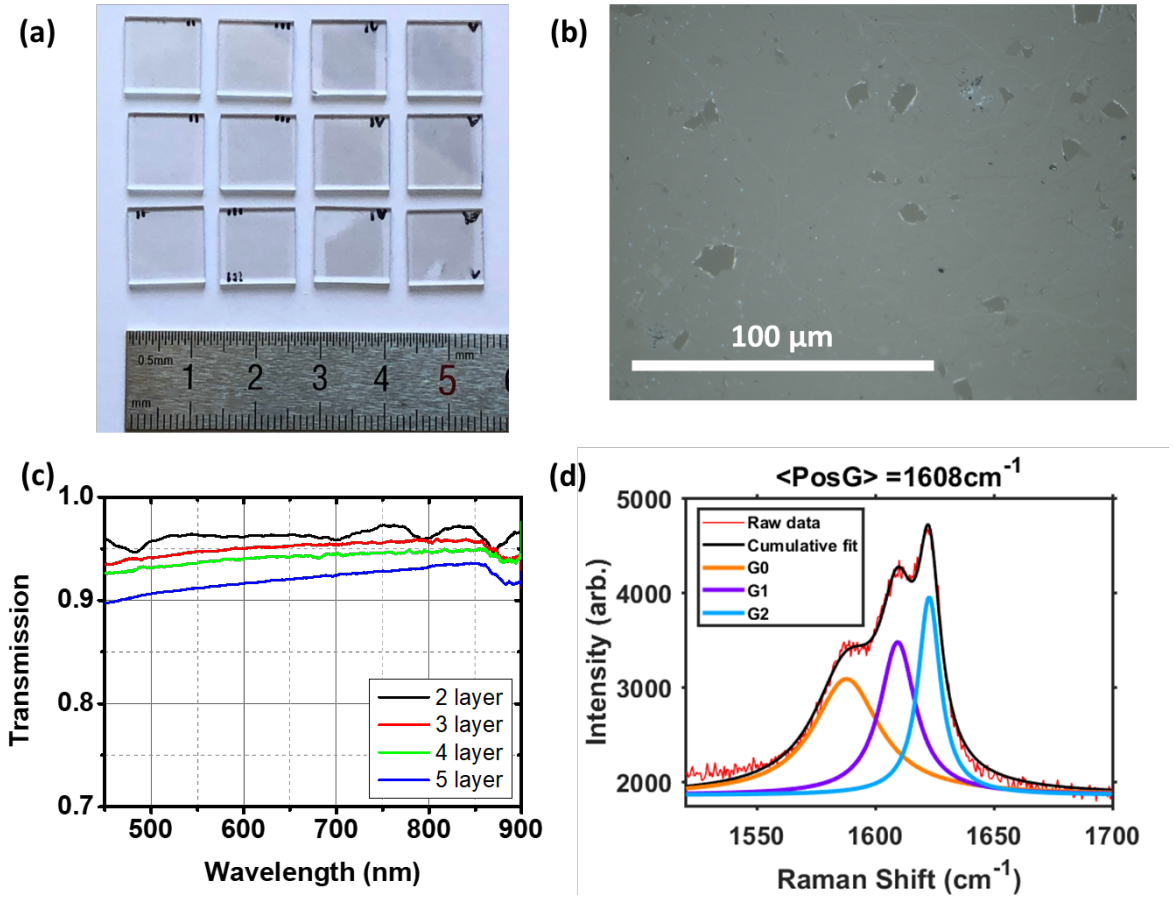

Figure 4.6: **(a)** Three sets of 2, 3, 4, and 5 layer (left to right) $FeCl_3$-FLG fabricated using the lamination transfer. **(b)** Microscope image of the surface of 2 layer $FeCl_3$-FLG transferred by this method. **(c)** Transmittance spectra for the 2, 3, 4, and 5 layer $FeCl_3$-FLG fabricated using the lamination transfer. **(d)** Raman spectrum showing the G peak of a 5 layer $FeCl_3$-FLG sample fabricated using the lamination transfer.

grown in this regard.[13] If it is possible to make FLG from multiply transferred SLG without residue this may be a better way to fabricate $FeCl_3$-FLG.

FLG was obtained from collaborators (the group of P Bøggild at DTU) who fabricated 2 - 5 layer FLG using the method described in Shivayogimath et al.[12] This was repeated 2 - 5 times to create the FLG.

This FLG was then intercalated as described in Section 3.2.1.2 to make $FeCl_3$-FLG. The $FeCl_3$-FLG was then characterised by Raman, transmittance, and sheet resistance.

Table 4.1: Properties of $FeCl_3$-FLG prepared by laminator transfer. Before/after intercalation.

Layers	Transmittance (%)	Sheet resistance ($\Omega\ \square^{-1}$)	$< PosG >$ (cm^{-1})	FoM
2 layer	96	2321/714	1590	4/13
3 layer	94	848/186	1593	7/32
4 layer	92	807/89	1595	5/47
5 layer	90	811/91	1599	4/38

The results of these can be seen in Figure 4.6.

Figure 4.6 (a) shows the 2 - 5 layer $FeCl_3$-FLG, the material appears uniform to the eye, with decreasing transmittance with the number of layers. Figure 4.6 (b) Shows a 50 times magnification microscope image of the surface of a 2-layer sample. Some small holes are present from damage caused by a four-point probe, the rest of the sample is highly uniform, with none of the obvious domains usually seen in nickel grown $FeCl_3$-FLG as there is in Figure 4.3 (b). The decreasing optical transmittance with layer number is confirmed across the visible part of the spectrum in Figure 4.6 (c). Figure 4.6 (d) shows a Raman spectrum of a point on a 5-layer sample. This spectrum clearly shows the presence of G_1, G_2, and G_3 peaks which make up the cumulative G peak. This indicates very strongly that $FeCl_3$ can at least partially penetrate the layers when transferred in this way.

The results of this study are summarised in Table 4.1. Here it is observed that after intercalation the 4-layer $FeCl_3$-FLG prepared by laminator transfer gives the highest figure of merit (FoM) at 47. This is a very respectable figure, outperforming the 35 that was indicated by De et al.[14] as the minimum threshold for commercial viability.

While the $< PosG >$ continues to increase with layer numbers, it can be seen that the sheet resistance is stable at approximately 90 $\Omega/\square$, and the transmittance is reducing with each additional layer. This results in 4-layer $FeCl_3$-FLG exhibiting the best combination of properties.

The success in fabrication of $FeCl_3$-FLG using this method clearly warrants further investigation. The material could be well suited to use as a transparent conductive electrode (TCE) in OLEDs if a lower roughness can be verified. The indication given by the FoM is that its electrical properties are well suited to use as TCE.

To continue the investigation into the lamination transfer method as an alternative for PMMA supported transfers I examined replacing PMMA for this method in the transfer of conventionally fabricated $FeCl_3$-FLG to PET.

4.3.3.3 *Nickel grown $FeCl_3$-FLG to PET transfer*

The PVA transfer method employed was as follows. All samples were rinsed with acetone, followed by IPA, before being blow-dried with nitrogen. The samples were placed on top of the PVA film, and sent through a laminator (Swordfish Armoured 660 Heavy Duty) at 110°C. The samples were then baked on a hot plate at 110°C for 30 seconds. The sample, now firmly adhered to the PVA is peeled off the initial substrate. The sample is placed onto the destination substrate and sent through the laminator at 110°C. The sample is baked on a hot plate at 110°C for 30 seconds. The paper support is peeled off the back of the PVA film. Finally, the sample, attached to the destination substrate is placed into a room temperature water bath for 24 hours. This dissolves the PVA leaving the transferred sample on a new substrate.

The results of previous works[12] involving copper substrates could be replicated for SLG. The transfer of $FeCl_3$-FLG from glass to PET was not possible. At the point in which $FeCl_3$-FLG was to be peeled off the glass substrate the sample remained firmly attached to the glass and did not stick to the PVA film. This result meant that going forward PMMA remains the best support layer and the one used throughout this work.

4.4 OLED CHARACTERISATION & OPTIMISATION

4.4.1 *OLED characterisation*

4.4.1.1 *Introduction*

As mentioned previously OLEDs had not been fabricated in my group before, this means the apparatus required to characterise them needed to be built. There are several device parameters that need to be measured to fully assess device performance, these are: bias voltage, device current, luminance, emission angle and wavelength.[15] The most basic measurements come from measuring the devices luminance while in operation.

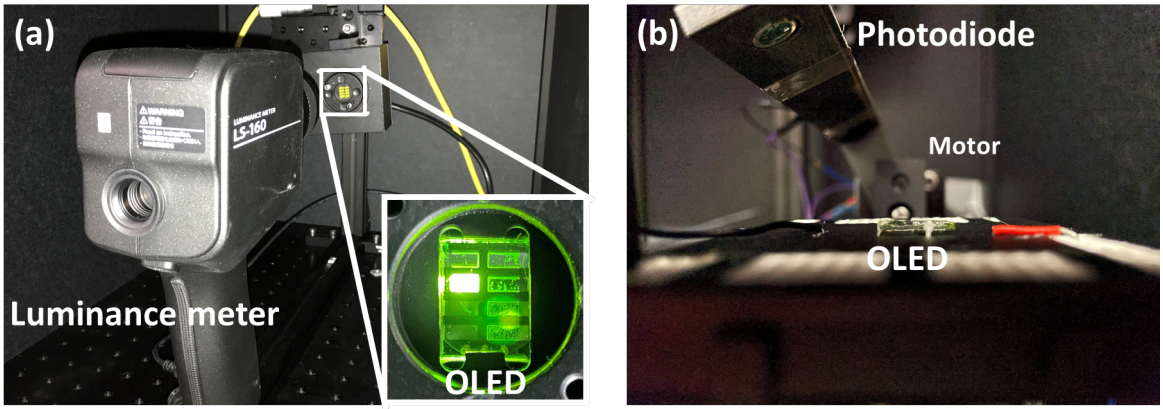

Figure 4.7: (a) The calibrated luminance meter in a dark box measuring the OLED (inset). **(b)** The goniometer setup measuring emission angle of an OLED. A photodiode inset into the goniometer arm moves around the device due to the stepper motor.

4.4.1.2 *Luminance measurement apparatus*

At all times OLEDs referred to in this thesis are operated by applying a bias voltage, V_{OLED}, and measuring the current, I_{OLED}. This is done by a Keithly 2400 multimeter, controlled by a LabVIEW routine. The most important parameter to measure when the OLED is powered is the luminance, L. There are two ways in which this can be done: using a photodiode, which will be discussed later, or using a calibrated luminance meter.

The luminance meter was chosen as it is factory calibrated and certified, detects luminance over the entire visible range and interfaces with the LabVIEW routine controlling the experiment. The luminance meter used throughout this work is a Konica Minolta LS-160 (Figure 4.7 (a)). This meter can detect a minimum luminance of 0.01 cd/m^2, has an accuracy of $\pm$ 2%, and minimum measuring area of 0.5 mm^2.

The luminance meter was mounted along an optical rail, directly opposite the OLED stage (Figure 4.7 (a)). The OLED stage could be moved by screw micrometers in x and y, so as the relevant pixel could be put in the view finder of the luminance meter. The luminance meter and the OLED were contained within a dark box. All natural light was excluded, and the luminance meter reported values below the 0.01 cm/m^2 threshold when measuring the dark.

It is possible to calculate two important metrics from these three measured param-

eters. These are current efficiency (CE) in cd/A:

$$CE = \frac{L}{I_{OLED}/a_{OLED}} \tag{4.2}$$

where a_{OLED} is the OLED area being powered, and power efficiency (PE) in lm/W:

$$PE = \frac{L \cdot a_{OLED} \cdot \pi}{I_{OLED} \cdot V_{OLED}} \tag{4.3}$$

4.4.1.3 *Emission angle apparatus*

To calculate the overall efficiency of an OLED device every photon being emitted from the device needs to be captured. This is normally done using an integration sphere. An integration sphere can capture photons emitted from all directions and redirect them to a spectrometer. To accommodate the samples discussed in this thesis, which are (12 mm x 12 mm x 1 mm), a relatively large integrating sphere would be required. Because one of the aims of this work is to have a compact, low-cost setup, the emission profile of the OLED is measured in a single plane using a goniometer, it can then be assumed that this profile is uniform when the device is rotated. It is also assumed that there is no back side emission. The emission angle measurement apparatus developed can be seen in Figure 4.7 (b) and is drawn in Figure 4.8 for clarity.

4.4.1.4 *EQE estimation*

To compare my OLED devices with those in the literature and with other devices with varying constructions it is important to know the EQE of the OLED.

EQE is the ratio of the number of photons emitted to the number of electrons injected. The number of electrons can be calculated via the current supplied to the OLED, I_{OLED}. Counting the photons emitted is not trivial.

There are two primary ways to count the photons out of a light-emitting device. The most rigorous way is to physically capture all the emitted photons using an integrating sphere. The integrating sphere captures all emitted photons and disperses them evenly around the spheres surface. By taking a measurement on this surface the total number of photons can be extrapolated from the intensity of the measurement. The advantage of this method is that the emission profile of the device does not need to be considered.

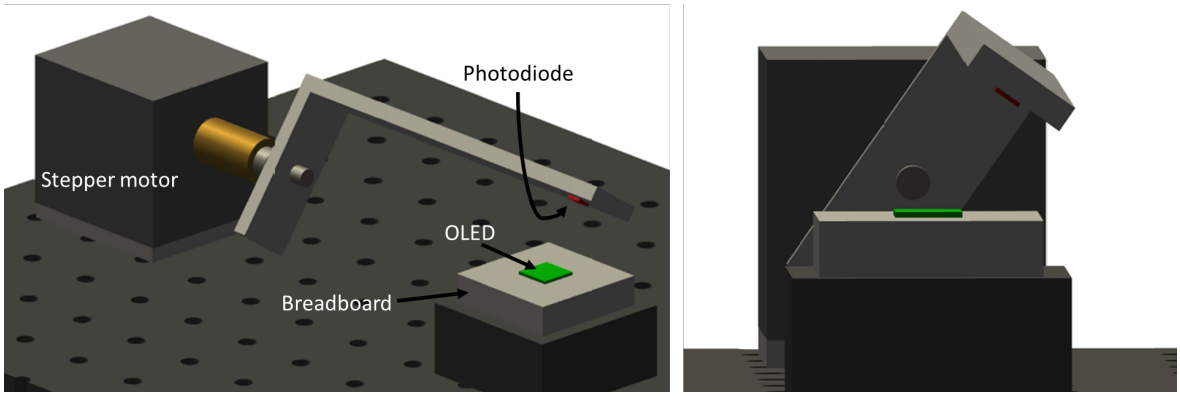

Figure 4.8: The emission angle apparatus used to measure the emission angle profile of OLED devices. A photodiode sweeps over the OLED, controlled by a stepper motor. The stepper motor is controlled by an Arduino microcontroller, the photodiode data is collected using a LabVIEW routine.

The second way to estimate EQE is by using a photodiode to measure the light intensity over a small solid angle out of the device and estimating the total light out of the forward hemisphere from the known emission angle dependence.[15;16]

To measure the light output of the device a photodiode (Osram BPW21) with known quantum efficiency (QE) is used. This quantity, $Q(\lambda)$, is given by the manufacturer. The photodiode operates in photovoltaic mode with a transimpedance amplifier consisting of an operational amplifier (Texas Instruments LM348N), feedback resistor, R_f, and feedback capacitor, C_f. This transimpedance amplifier setup is shown in Figure 4.9. The sensitivity, H, of the transimpedance amplifier can be calculated from Equation 4.4.

$$I_{PD} = -\frac{V_{out}}{R_f} \tag{4.4}$$

Where V_{out} is the voltage out of the transimpedance amplifier, and I_{PD} is the current supplied to the amplifier from the photodiode in the circuit seen in Figure 4.9. The sensitivity, H, which has units of $e^{-}s^{-1}V^{-1}$, is the number of electrons that flow resulting in 1 V at the output terminal. This is calculated by taking the number of electrons in 1 ampere of current, divided by R_f. Bearing in mind 1 ampere is defined as 1 C/s. The charge on the electron is 1.6×10^{-19} $C/electron$. Therefore, the number

of electrons per Columb is $\frac{1}{1.6\times10^{-19}}$ $electrons/C$. Giving 1 ampere being equal to 6.2×10^{18} $e^{-}s^{-1}$.

R_f is chosen so as to adjust the gain in the system. The voltage at point A is assumed to be always equal to zero. This is because the operational amplifier has a very high input impedance and is connected to ground via the non-inverting input (+). Therefore $I_{PD} = I_{R_f} = V_{out}/R_f$. This means $V_{out} = I_{PD} \cdot R_f$. To choose the resistor value, the maximum expected photodiode current, $I_{PD_{max}}$, is used:

$$R_f \leq \frac{V_{max}}{I_{PD_{max}}} \tag{4.5}$$

where V_{max} is the maximum voltage output of the op-amp, the voltage supplied to it, in this work that is 5 V. If $I_{PD_{max}} = 50$ μA, then ≤ 100 $k\Omega$ resistor should be used.

C_f ensures the stability of the device. In a real op-amp there will be some input capacitance and stray capacitance across the inputs. This can cause output drift and ringing oscillation. To eliminate this a capacitor is added in parallel. The capacitor needs to be chosen with respect to a required bandwidth.

$$C_f \leq \frac{1}{2\pi R_f f_p} \tag{4.6}$$

where f_p is the required bandwidth frequency.

The advantage of using the photodiode like this is that dark current is eliminated, making the photodiode very sensitive to low light.

The effective solid angle Ω_{PD} is now calculated. This is the solid angle swept out by the circular photodiode. This value is given by Equation 4.7.

$$\Omega_{PD} = 2\pi(1 - cos\frac{R_{PD}}{D}) \tag{4.7}$$

where R_{PD} is the radius of the circular photodiode sensor, and D is the distance from the device to the photodetector.

The photon flux, ϕ_{PD}, striking the photodiode at any given second for a given voltage, V_{out} is calculated.

$$\phi_{PD} = \frac{H}{C\Omega_{PD}} \cdot V_{out} \tag{4.8}$$

where C is the photodiode QE, $Q(\lambda)$ weighted by the electroluminescence (EL)

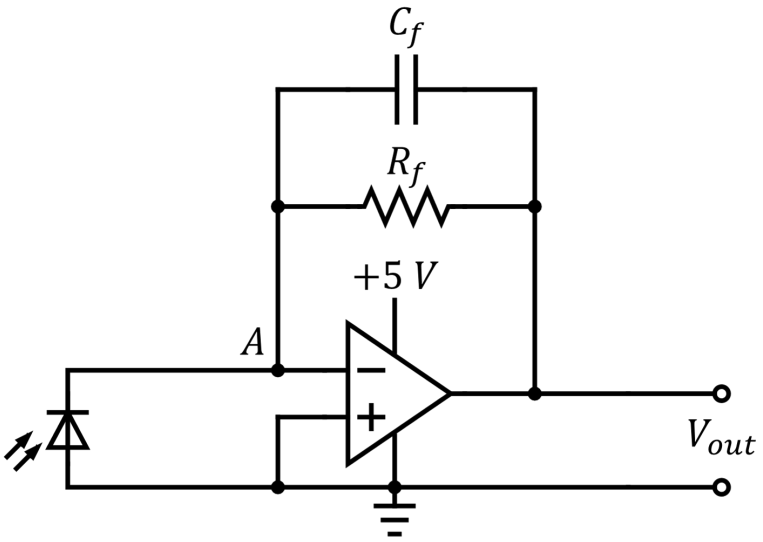

Figure 4.9: The transimpedance amplifier used in conjunction with a photodiode to measure light intensity out of the device. This apparatus is used when measuring the emission angle profile of the device.

spectrum of the device, $S(\lambda)$ and is given by Equation 4.9

$$C = \frac{\int Q(\lambda) \cdot S(\lambda) d\lambda}{\int S(\lambda) d\lambda} \tag{4.9}$$

The radiance of the device, R', is then given by $R' = \phi_{PD} \cdot E_{photon}$. Where E_{photon} is the average energy per photon and is given by Equation 4.10

$$E_{photon} = \frac{\int S(\lambda) \cdot \frac{hc}{\lambda} d\lambda}{\int S(\lambda) d\lambda} \tag{4.10}$$

where h is Planck's constant, and c is the speed of light.

With the angular distribution of light emitted measured, or assumed to be Lambertian, as in this case, then $R'(\theta) = R' cos(\theta)$. The total photon flux, Φ, can then be calculated by taking $R'(\theta)$ and integrating it over the entire forward-facing hemisphere. This is shown in Equation 4.11 for the Lambertian case.

$$\Phi = \frac{\pi}{E_{photon}} \int_0^{\pi/2} R'(\theta) d\theta = \phi_{PD} \pi \tag{4.11}$$

From the original definition of the EQE we know that it is simply the ratio of photons out to electrons in, this is seen in Equation 4.12.

$$EQE = \frac{\Phi}{I_{OLED}/q} = \frac{q\pi H}{C\Omega_{PD}} \cdot \frac{V_{out}}{I_{PD}} \tag{4.12}$$

where q is the elementary charge.

Going one step further from this will allow me to verify my results by comparing them to those obtained by the luminance meter. To do this the response of the human eye must be taken into account. For this $S(\lambda)$ must be weighted by the normalised photopic curve, $P(\lambda)$, which reproduces the spectral response of the human eye when normalised to $683.002\,\mathrm{lm\,W^{-1}}$. This is defined as the conversion factor K, shown in Equation 4.13

$$\frac{\int P(\lambda) \cdot S(\lambda) \cdot \frac{hc}{\lambda} d\lambda}{\int S(\lambda) d\lambda} \tag{4.13}$$

which returns a value with units $lm \cdot s \cdot photon^{-1}$.

With this conversion factor, K, the luminance can now be calculated, L, and the current efficacy, $\eta_{current}$, and compare these to the values obtained from the luminance meter.

$$L = \frac{\Phi_{PD} K}{a_{OLED}} = \frac{HK}{C\Omega_{PD} a_{OLED}} \cdot V_{PD} \tag{4.14}$$

$$\eta_{current} = \frac{HK}{C\Omega_{PD} I_{OLED}} \cdot V_{PD} \tag{4.15}$$

Finally, the luminous efficacy (power efficiency) can be obtained, η_{lum}, in a similar way to the EQE, by integrating the emitted photons over the entire forward hemisphere. The result of which is shown in Equation 4.16.

$$\eta_{lum} = \frac{\pi HK}{C\Omega_{PD}} \cdot \frac{V_{PD}}{V_{OLED} I_{OLED}} \tag{4.16}$$

When using this method of EQE estimation I now have a way of verifying the result by comparing the estimated L, $\eta_{current}$, and η_{lum} to their respective values given by the calibrated luminance meter.

4.4.2 *OLED optimisation*

4.4.2.1 *ITO etching*

When investigating the properties of $FeCl_3$-FLG as a TCE it is important to verify those properties in a working device. For this OLEDs were chosen. In almost all modern OLEDs the TCE of choice is ITO.[17;18] ITO has become the industry standard over decades for almost all TCE applications. Typically, ITO is sputtered onto glass for use in OLEDs and photovoltaics (PVs).[19] This meant it was easy to source patterned, ITO covered glass for use in rigid OLEDs. One of the key material properties of $FeCl_3$-FLG is that it is graphene-based and therefore flexible. This means ITO sputtered onto PET needed to be patterned. While acquiring ITO coated PET was possible, there was a need to develop a patterning method for ITO.

The method developed was as follows; ITO coated PET (Sigma Aldrich) is cut to desired size and the region of ITO required for the device is protected by masking with Kapton tape. The masked sample is then placed into HCl 2M for 2 minutes. The sample is rinsed in DI water, followed by IPA, then blow dried with nitrogen. The tape is removed, the sample is rinsed and dried again, and is now ready to be used in the device.

When the masked region of ITO was inspected it remained clean and there appeared to be no damage. The unmasked region had clearly been affected by the acid. Optically it was clear that the ITO had been etched, the PET appeared undamaged. The sheet resistance of the ITO was unchanged, the unmasked region was no longer conductive. When the roughness was measured using an atomic force microscopy (AFM) the ITO retained its low roughness, as did the unmasked region. This method was subsequently used to pattern all ITO coated PET used throughout this thesis.

I have already discussed the choice of OLED materials in Section 3.2.2. Here I will show the optimisation of the chosen layers. Of critical importance in any OLED device is the layer thickness. If layers are too thick, they will increase the overall device resistance, block light out, and reduce overall efficiency. If layers are too thin electrons or holes can pass through without the desired effect. It is important that the layer thickness of each layer in the OLED is known and controlled to ensure optimal device performance.

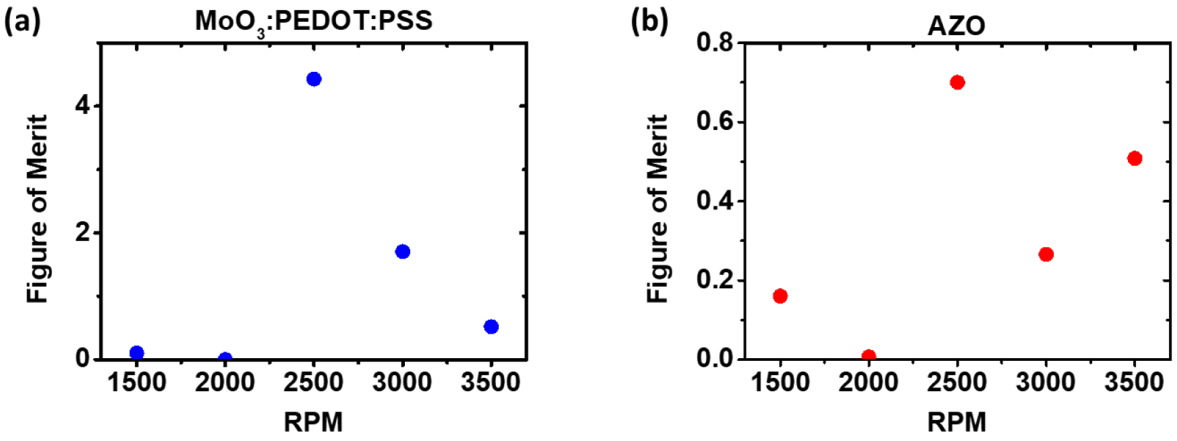

Figure 4.10: **(a)** Performance of MoO_3:PEDOT:PSS enhanced OLEDs, plotted against spin-coat speed in RPM. The devices with spin speed of 2500 RPM clearly performed best. **(b)** Performance of AZO enhanced OLEDs, plotted against spin-coat speed in RPM. The devices with spin speed of 2500 RPM clearly performed best.

4.4.2.2 *Inverted OLED*

The structure of the inverted OLED in this work is $FeCl_3$-FLG/ITO, aluminium doped zinc oxide (AZO), polyethylenimine ethoxylated (PEIE), poly(9,9-dioctylfluorene-alt-benzo-thiadiazole) (F8BT), MoO_3:PEDOT:PSS, gold. These are the transparent cathode, electron transport layer (ETL), hole blocking layer (HBL), emission layer, hole transport layer (HTL), and metal anode, respectively. In this section I will investigate the effect of various thicknesses of MoO_3:PEDOT:PSS and *AZO*.

To do this MoO_3:PEDOT:PSS and *AZO* were integrated into OLEDs in the way described in Section 3.2.2. These materials were spun at speeds ranging from 1500 RPM to 3500 RPM, the rest of the devices were made in the way described in Section 3.2.2. In total 14 OLEDs were made, with 8 pixels each. Every pixel was tested for a total of 112 pixels. For each spin speed 5 metrics were recorded, these were: luminance, L, CE, PE, turn-on voltage, V_T, and yield. These values were averaged for each spin speed and yield was calculated. To compare all these parameters at once a figure of merit was used, this gave equal weighting to all 5 parameters. The figure of merit is calculated as:

$$OLED_{FoM} = \frac{L \cdot CE \cdot PE \cdot V_T}{\text{yield}} \tag{4.17}$$

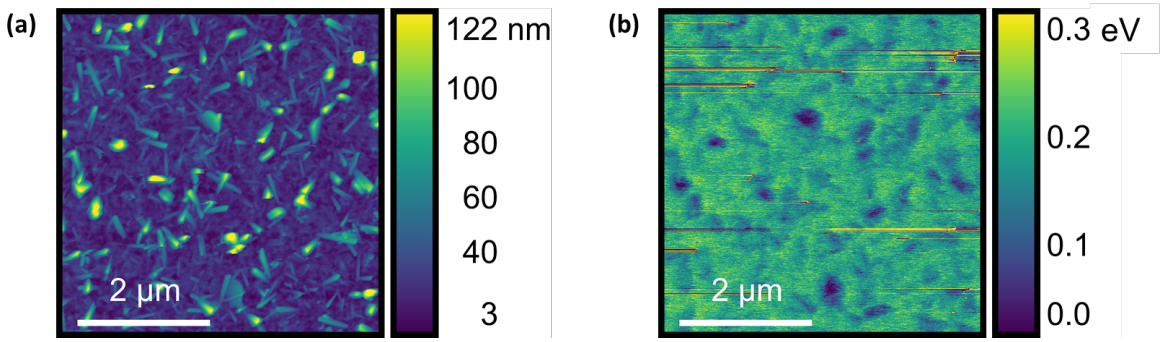

Figure 4.11: **(a)** AFM image of MoO_3:PEDOT:PSS surface. The core-shell structure of the material can be seen. **(b)** SKPFM map of the same. There is a peak-to-trough difference in potential of 0.4 eV.

Figure 4.10 (a) & (b) shows the results of this investigation for MoO_3:PEDOT:PSS and AZO respectively. It is clear that the optimal combination of properties occurs at 2500 RPM for both MoO_3:PEDOT:PSS and AZO. Going forward therefore all inverted OLEDs will use these spin speeds for spin-coating MoO_3:PEDOT:PSS and AZO. All these samples were annealed in the same way. For AZO the samples were annealed by placing on a hot plate at 200°C for 10 minutes. This temperature is too high for devices that will be made on PET substrates, so the recipe will change to a 120°C anneal.

4.4.2.3 *Work function of MoO_3:PEDOT:PSS*

The MoO_3:PEDOT:PSS used in this work is a composite material made from a mixture of MoO_3 in ethanol and aqueous poly(3,4-ethylenedioxythiophene) polystyrene sulfonate (PEDOT:PSS). The ink was originally proposed to allow MoO_3 to be solution processed without aggregating into clumps.[20] When in a mixture with PEDOT:PSS a core-shell structure forms with PEDOT chains at the core, and MoO_3 particles connected to PSS chains making the shell.[20] The ink was chosen because of the known effectiveness of PEDOT:PSS as a HTL, and because of the deep work function of MoO_3. The very deep lowest unoccupied molecular orbital (LUMO) of MoO_3 should act as a hole reservoir for the active material with no energy barrier.[20]

Using an AFM and a technique known as scanning Kelvin probe force microscopy (SKPFM) the electrical potential of the material was measured alongside a height map. The results of this are seen in Figure 4.11. The core-shell structure can be seen

clearly in Figure 4.11 (a). The tubular shapes consistent with a shell forming around a long polymer chain. Areas where larger aggregates have formed coincide with deeper work function consistent with the deeper work function of MoO_3 and their tendency to form aggregates. The absolute values here are not relevant as the probe tip was not calibrated before mapping, but the difference is. The areas with aggregates have a work function up to 0.4 eV deeper than the other regions.

Overall, the surface is not as homogeneous as expected. The shell structure does not result in a uniform work function. 0.4 eV is large enough to add significant resistance to the device. The roughness is also high, at 19 nm. This however is not so much of an issue for my devices, as this layer is deposited on top of the emission layer, and the gold deposited on top is at least 60 nm thick.

Going forward an investigation using calibrated SKPFM must take place to determine the work function of this material layer. This could confirm whether the MoO_3 shell does act in the same way as evaporated MoO_3 in providing a very deep LUMO.

4.5 SAMPLE BENDING

4.5.0.1 *Push bender*

To test OLED devices, substrates, and electrodes for bending performance a quantitative bending apparatus needed to be built. Initially it was envisaged that a simple push bender could serve this purpose. This device works by wedging a sample between a gap so as the sample is lying horizontally, then reducing the size of the gap, forcing the sample to bend. This device allows the sample to either rest on the sample holder, or the sample is clamped down at both sides. The opposite edges of the sample are pushed together so as the sample bends, this is done repeatedly, and can be seen in Figure 4.12. This type of sample and material bending is reported widely. This type of bending has major drawbacks, however. Figure 4.12 (a) shows the unclamped sample being bent. The bending is not uniform across the device. There is almost no bending at the left and rightmost edges, while there is a small bending radius in the centre. This bending is not putting a uniform amount of stress on the device, the shape is parabolic. Figure 4.12 (b) shows the clamped sample, here there are three points of low bending radius. This configuration also potentially damages the device when being clamped. To address these issues a completely different bending apparatus is required.

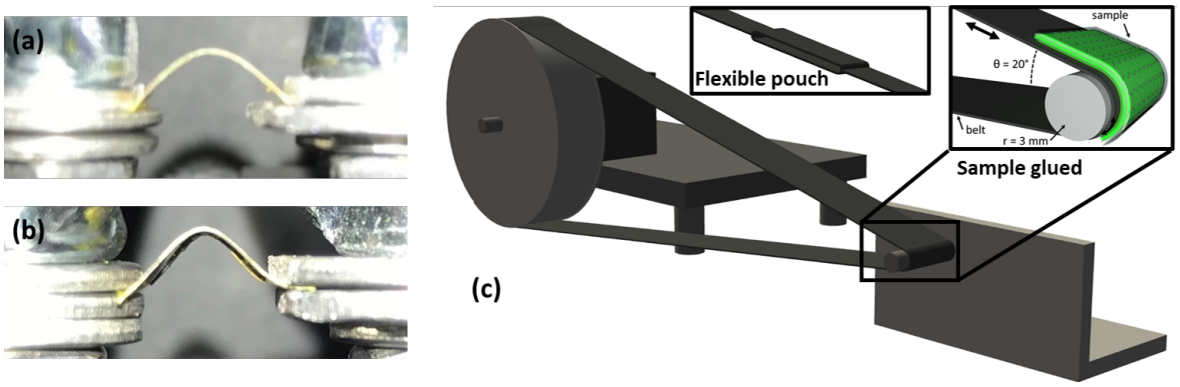

Figure 4.12: **(a)** Image of a sample being bent using a push bender. The bending radius is smallest in the middle of the sample. **(b)** Image of a sample being bent in a clamped push bender. The sample bends at 3 points, the bending radius is not uniform across the device. **(c)** The roller bender solution. The sample is attached to a belt which moves around a pin of set radius. The sample (shown inset) bends around the pin in a uniform way, the entire sample is subject to the same stress. The sample can be glued to the belt or slid into a flexible pouch.

4.5.0.2 *Roller bender*

Based on the ideas in Li et al.[21] I developed a roller bender apparatus. Here the idea is to mount the test device on a belt and move the belt around a pin of fixed, known diameter. This pin can be easily changed for different diameter pins, and hence different bending radii. Figure 4.12 (c) shows the bending solution that I have employed in this work. Here the sample is mounted to a belt and rolled around a pin of fixed radius. This allows the entire device to be subject to uniform stresses. This apparatus allows for bending around a fixed radius, the pin can be swapped out for a different size at any point. This apparatus works by rotating a belt back and forward around the pin. The rotation is controlled by a stepper motor controlled by an Arduino microcontroller. The bender can repeatedly bend samples thousands of times in a controlled and repeatable manner. The samples must be removed from the bender to be tested for performance. OLEDs cannot be lit while in the bender, they must be tested before and after bending. They can be tested multiple times by using the flexible pouch to hold the sample.

4.6 SUMMARY AND OUTLOOK

A new Raman metric, $< PosG >$, has been introduced for assessing the intercalation quality of FLG with $FeCl_3$. This metric was then used in a large area map to assess the overall quality of $FeCl_3$-FLG samples.

Through the optimisation of $FeCl_3$-FLG fabrication the transfer process has been enhanced for large area samples, preventing breakage, and allowing for more controlled and repeatable transfers. Furnace temperature has also been optimised, this has resulted in an increase in the measured $< PosG >$, and a reduction in the sheet resistance of intercalated samples from $\approx 200\ \Omega/\square$ for the original T_1 to $\approx 100\ \Omega/\square$ for the new T_1. It has also reduced the variation between samples, meaning a more consistent material can now be fabricated. This reduction in variation is particularly important for use in OLEDs, as the consistency of ITO is very good, and the aim was to be able to make fair comparisons.

I was able to optimise the OLED fabrication also. The material thicknesses were assessed and compared to expected thicknesses. These were then assessed in working devices using ITO as the TCE.

The characterisation tools were constructed, in order to evaluate the performance of OLEDs in the next sections. The EQE will be estimated for devices fabricated later using the setup introduced here, without the help of an expensive integrating sphere.

Finally sample bending was introduced. Common bending techniques were compared and built a setup to repeatedly bend samples around a constant and fixed radius, thus subjecting a sample to a constant level of bending in a controlled and uniform way.

BIBLIOGRAPHY

[1] Thomas H. Bointon, Gareth F. Jones, Adolfo De Sanctis, Ruth Hill-Pearce, Monica F. Craciun, and Saverio Russo. Large-area functionalized CVD graphene for work function matched transparent electrodes. *Scientific Reports*, 5(1):16464, 12 2015.

[2] Kieran Walsh, Conor Murphy, Gareth Jones, Matthew Barnes, Adolfo De Sanctis, Dong-Wook Shin, Saverio Russo, and Monica Craciun. Wafer scale FeCl3 intercalated graphene electrodes for photovoltaic applications. In *Photonics for Solar Energy Systems VII*, volume 10688C, page 52. SPIE, 5 2018.

[3] Simone Pisana, Michele Lazzeri, Cinzia Casiraghi, Kostya S. Novoselov, A. K. Geim, Andrea C. Ferrari, and Francesco Mauri. Breakdown of the adiabatic Born-Oppenheimer approximation in graphene. *Nature Materials*, 6(3):198–201, 2 2007.

[4] Michele Lazzeri and Francesco Mauri. Nonadiabatic Kohn anomaly in a doped graphene monolayer. *Physical Review Letters*, 97(26):266407, 12 2006.

[5] Ivan Khrapach, Freddie Withers, Thomas H. Bointon, Dmitry K. Polyushkin, William L. Barnes, Saverio Russo, and Monica F. Craciun. Novel highly conductive and transparent graphene-based conductors. *Advanced Materials*, 24(21):2844–2849, 6 2012.

[6] Yi Zhang, Lewis Gomez, Fumiaki N Ishikawa, Anuj Madaria, Koungmin Ryu, Chuan Wang, Alexander Badmaev, and Chongwu Zhou. Comparison of graphene growth on single-crystalline and polycrystalline Ni by chemical vapor deposition. *Journal of Physical Chemistry Letters*, 1(20):3101–3107, 2010.

[7] Da Luo, Xueqiu You, Bao Wen Li, Xianjue Chen, Hyo Ju Park, Minbok Jung, Taeg Yeoung Ko, Kester Wong, Masood Yousaf, Xiong Chen, Ming Huang, Sun Hwa Lee, Zonghoon Lee, Hyung Joon Shin, Sunmin Ryu, Sang Kyu Kwak, Noejung Park, Revathi R. Bacsa, Wolfgang Bacsa, and Rodney S. Ruoff. Role of Graphene in Water-Assisted Oxidation of Copper in Relation to Dry Transfer of Graphene. *Chemistry of Materials*, 29(10):4546–4556, 5 2017.

[8] Yung Chang Lin, Chun Chieh Lu, Chao Huei Yeh, Chuanhong Jin, Kazu Suenaga, and Po Wen Chiu. Graphene annealing: How clean can it be? *Nano Letters*, 12(1):414–419, 1 2012.

[9] Joshua D Wood, Gregory P Doidge, Enrique A Carrion, Justin C Koepke, Joshua A Kaitz, Isha Datye, Ashkan Behnam, Jayan Hewaparakrama, Basil Aruin, Yaofeng Chen, Hefei Dong, Richard T Haasch, Joseph W Lyding, and Eric Pop. Annealing free, clean graphene transfer using alternative polymer scaffolds. *Nanotechnology*, 26(5), 2015.

[10] Manfred L. Hallensleben, Robert Fuss, and Florian Mummy. Polyvinyl Compounds, Others. In *Ullmann's Encyclopedia of Industrial Chemistry*, pages 1–23. John Wiley & Sons, Ltd, 7 2015.

[11] Hydrokon PVA Film User Guide. *Hydrokon Water Transfer Film*, 2 2021.

[12] Abhay Shivayogimath, Patrick Rebsdorf Whelan, David M.A. MacKenzie, Birong Luo, Deping Huang, Da Luo, Meihui Wang, Lene Gammelgaard, Haofei Shi, Rodney S. Ruoff, Peter Bøggild, and Timothy J. Booth. Do-It-Yourself Transfer of Large-Area Graphene Using an Office Laminator and Water. *Chemistry of Materials*, 31(7):2328–2336, 4 2019.

[13] Arjun Dahal and Matthias Batzill. Graphene-nickel interfaces: A review. *Nanoscale*, 6(5):2548–2562, 2 2014.

[14] Sukanta De and Jonathan N. Coleman. Are there fundamental limitations on the sheet resistance and transmittance of thin graphene films? *ACS Nano*, 4(5):2713–2720, 5 2010.

[15] Miguel Anaya, Barry P. Rand, Russell J. Holmes, Dan Credgington, Henk J. Bolink, Richard H. Friend, Jianpu Wang, Neil C. Greenham, and Samuel D. Stranks. Best practices for measuring emerging light-emitting diode technologies. *Nature Photonics*, 13(12):818–821, 12 2019.

[16] Illuminating Engineering Society of North America Standards LM-79-08, LM-80-08, TM-21-11 and LM-82-12. Technical report, American National Standards Institute.

[17] Thomas H. Bointon. *Graphene and functionalised graphene for flexible and optoelectric applications*. PhD thesis, University of Exeter, 4 2015.

[18] Michael Hengge, Konstantin Livanov, Natalia Zamoshchik, Felix Hermerschmidt, and Emil J.W. List-Kratochvil. ITO-free OLEDs utilizing inkjet-printed and low temperature plasma-sintered Ag electrodes. *Flexible and Printed Electronics*, 6(1):015009, 2 2021.

[19] Ocal Tuna, Yusuf Selamet, Gulnur Aygun, and Lutfi Ozyuzer. High quality ITO thin films grown by dc and RF sputtering without oxygen. *Journal of Physics D: Applied Physics*, 43(5):055402, 1 2010.

[20] Yiling Wang, Qun Luo, Na Wu, Qiankun Wang, Hongfei Zhu, Liwei Chen, Yan Qing Li, Liqiang Luo, and Chang Qi Ma. Solution-processed MoO3:PEDOT:PSS hybrid hole transporting layer for inverted polymer solar cells. *ACS Applied Materials and Interfaces*, 7(13):7170–7179, 2015.

[21] Haoyu U. Li and Thomas N. Jackson. Flexibility testing strategies and apparatus for flexible electronics. *IEEE Transactions on Electron Devices*, 63(5):1934–1939, 5 2016.

5

FECL$_3$-FLG AS TRANSPARENT, FLEXIBLE ELECTRODE IN OLEDS

5.1 INTRODUCTION

This chapter covers the integration of $FeCl_3$ intercalated FLG ($FeCl_3$-FLG) into organic light-emitting diodes (OLEDs). The devices discussed in this chapter are solution processed at relatively low temperature, often in ambient conditions. This satisfies the requirements of potentially flexible, low temperature, solution processable, and low-cost. The fabrication procedures of all the devices discussed in this chapter are shown in Section 3.2.2. These OLEDs are repeatedly exposed to atmosphere during the fabrication process and are not encapsulated for testing.

All devices are prepared in the same way, this allows me to compare them reliably to each other. For this reason, I have elected to evaluate the performance of $FeCl_3$-FLG in OLEDs by comparing them to the same devices running with the industry standard transparent conductive electrode (TCE), indium tin oxide (ITO).

The key properties to consider when evaluating $FeCl_3$-FLG against ITO are the sheet resistance, R_S, the optical transmittance, T, particularly the transmittance at 550 nm (T_{550}) as this is most commonly cited[1] and the peak luminance of poly(9,9-dioctylfluorene-alt-benzo-thiadiazole) (F8BT) is close to 550 nm, the work function, Φ, and the flexibility. The transmittance of the TCEs can be seen in Figure 5.1 (a).

A material used as TCE with higher sheet resistance will result in an OLED device with lower luminance uniformity and higher turn-on voltage.[2;3] Lower luminance results from the fact that there will be a high voltage drop across the active area of the device and more voltage will be required to drive the same current and achieve the same

brightness. Overall device efficiency will be reduced as a result, therefore $EQE \propto \frac{1}{R_S}$, where external quantum efficiency (EQE) is defined in Equation 4.12.

If the material has reduced optical transmittance this will result in fewer photons out of the device. This will be seen as a reduction in luminance. Overall device efficiency will be lowered as a result with $EQE \propto T$.

Any mismatched work function will create an energy barrier for electrons or holes depending on inverted or conventional device structure.[2–4] The energy barrier ΔE will require higher voltage to achieve the same luminance. Overall device efficiency will reduce as a result, with $EQE \propto \frac{1}{\Delta V}$.

When considering the mechanical properties, materials with low flexibility will break when flexed. An open circuit will be created, and the device will not operate. As the material begins to crack small cracks may appear across the material, this will result in a large increase in the material's sheet resistance and so the device efficiency will drop before failing completely. This is shown when I tested the flexibility of $FeCl_3$-FLG vs ITO.

The overall aim of this chapter is to access the performance of the solution processed OLEDs with $FeCl_3$-FLG electrodes. These will be benchmarked against ITO based devices. Following devices on rigid substrates, electrodes will be assessed for flexible performance, before devices are fabricated in the same was as before on these flexible substrates. I will then look at an alternative device architecture in an attempt to improve the base device performance.

5.2 CHARACTERISATION

5.2.1 *OLED materials characterisation*

Before the OLED devices are tested, it is important to know if they have been fabricated as expected. The transmittance of the electrodes can vary depending on the exact material, substrate, and supplier, so transmittance was measured for all TCEs before they were incorporated into OLEDs. Figure 5.1 (a) shows the optical transmittance of the various TCEs from 420 nm to 850 nm, the limits of the spectrometer used. The transmittance curves are all relatively flat, indicating uniform transmittance across the visible range, consistent with what is observed. The numerical values for transmittance are summarised in Table 5.3.

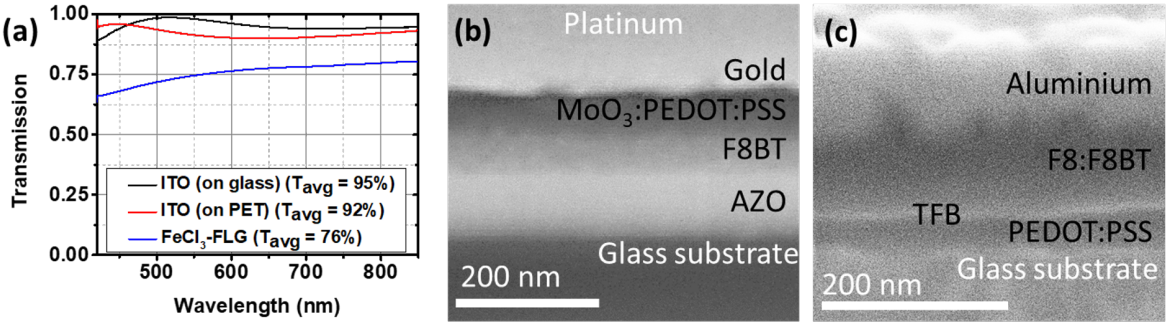

Figure 5.1: **(a)** Transmittance data for the TCEs used in this chapter. The transmittance value shown is the average value from 420 to 850 *nm*. **(b)** SEM image of the conventional device. **(c)** SEM image of the inverted device. Each of the materials observed are labelled.

Table 5.1: Thicknesses of each material layer in the inverted and conventional OLEDs as recorded by the SEM and the profiler.

Material	Thickness (*nm*)		Material	Thickness (*nm*)	
	SEM	Profiler		SEM	Profiler
Gold	59.5	60	Aluminium	97.2	100
MoO_3:PEDOT:PSS	55.5	50	Liq	10	5
F8BT	71.4	224	F8:F8BT	58.0	80
AZO	119.0	90	TFB	25.6	40
			PEDOT:PSS	30.2	40

Once the devices are fabricated it is important to know that the layers were deposited correctly. Most issues can be spotted visually, but it is important to know the layer thickness is approximately what is expected. This can be done by destructively using a focused ion beam (FIB)-scanning electron microscope (SEM). The FIB is used to mill a hole through the OLED, the sample is then viewed at an angle using the SEM. Depending on whether or not good electrical contact can be made, more metal may need to be deposited onto the device. In Figure 5.1 (b) I needed to deposit platinum to get good contact. Each layer can be clearly seen for both the inverted device and the conventional device in Figure 5.1 (b) and (c). The layer thicknesses were then measured using the built-in measuring tool, and checked by measuring each layer using a profiler. The results of this are summarised in Table 5.1.

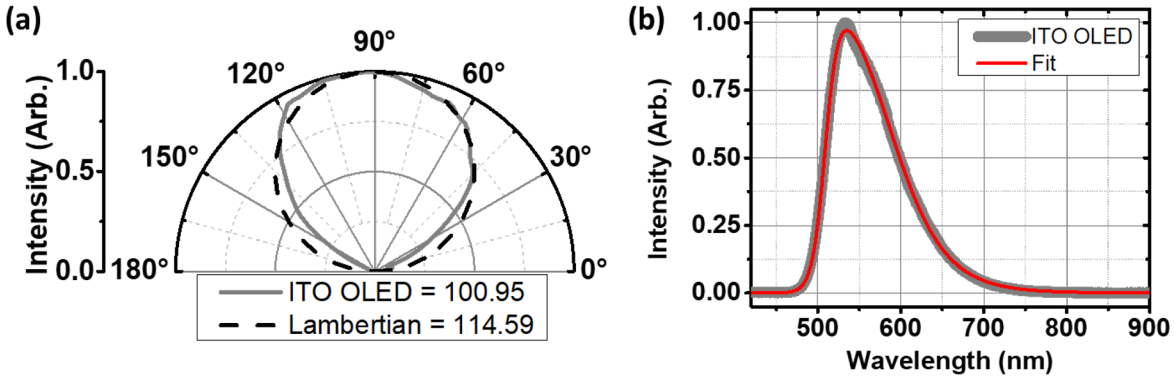

Figure 5.2: **(a)** Polar graph of emission intensity vs emission angle for an ITO based OLED. The area under the curve is compared to that of ideal Lambertian emission. **(b)** The EL spectrum of an ITO OLED with BiHill curve fit and a peak luminescence at 535 nm.

5.2.2 *Methodology for OLED performance characterisation*

To fully characterise the OLEDs made in this work the most widely reported value for efficiency need to be known. This is the EQE which is derived in Section 4.4.1.4. The first parameter needed to quantify to estimate the EQE is the emission angle profile of the OLEDs. This is done using the setup described in Section 4.4.1.3. For this a rigid ITO based OLED is used as reference.

When EQE is derived in Equation 4.12 it is assumed that the emission profile of the device is Lambertian. This would mean that the measured emission is proportional to $\sin(\theta)$, where θ is the angle in degrees. As this may not be the case the emission angle profile needs to be measured. In order to obtain the correction factor, the area under the curve for the OLED device was compared to a Lambertian emitter, as seen in Figure 5.2 (a). The resulting correction factor is $C.F. = 100.95/114.59 = 0.881$. This correction factor will simply be multiplied by the EQE as calculated in Equation 4.12 to give the actual EQE value. In the OLED devices investigated here there is a significant loss compared to a Lambertian emitter at high angles of emission. This is likely due to some internal reflections caused by the 1 mm thick glass substrate with the emitter on the bottom side.

The next device property that needs to be measured is its electroluminescence (EL) spectrum, denoted $S(\lambda)$. This is measured using the spectrometer in the custom-build microscope setup seen in Figure 3.7. The sample is mounted on the sample stage and

powered on, the light travels through the same optics used for transmittance measurements seen in Figure 3.7 (c). The measurement is then recorded by the spectrometer. The results of this measurement are seen in Figure 5.2 (b). In order to integrate the EL spectrum into the EQE derivation, the experimental data is fitted to find the function that best describes it. In this case the best mathematical description of the EL spectrum curve is given by the biphasic Hill (BiHill) function[5] defined by:

$$y = \frac{P_m}{[1 + (\frac{K_a}{x})^{H_a}][1 + (\frac{x}{K_i})^{H_i}]} \tag{5.1}$$

where P_m is the maximum, K_a is the half-maximal activating, K_i is the half-maximal inhibitory, H_a is the activation Hill coefficient, and H_i is the inhibitory Hill coefficient. When fit to EL spectrum, y represents intensity, and x represents wavelength. For the fit shown in Figure 5.2 (b) has values of: $P_m = 1.18396$, $K_a = 5.09472 \times 10^{-7}$, $K_i = 5.88633 \times 10^{-7}$, $H_a = 64.7142$, and $H_i = 18.5058$. The fit using this method is excellent, evidenced by an $R^2 = 0.99957$, with a value of 1 indicating a perfect fit. This fit using these values will be taken as $S(\lambda)$ for the EQE calculation.

These values for the emission angle correction factor and $S(\lambda)$ will be assumed to be constant for all devices tested. This methodology is appropriate because for the correction factor the substrate is the major cause for the difference from a Lambertian emitter, which is constant, and the $S(\lambda)$ will be the same for all devices fabricated using an identical protocol.

When using the photodiode to measure device EQE, Equation 4.12 is used. To this end, the photodiode voltage, V_{PD}, and the OLED current, I_{OLED} must be measured. The remaining factors are constants for this arrangement.

For devices which are tested using the Konica Minolta luminance meter, rather than the photodiode the EQE can be estimated, this is shown as:

$$EQE = \frac{A_{OLED} L q \pi}{K \cdot I_{OLED}} \tag{5.2}$$

where

$$K = \frac{\int P(\lambda) \cdot S(\lambda) \cdot \frac{hc}{\lambda} d\lambda}{\int S(\lambda) d\lambda} = 1.67 \times 10^{-16}\ lm \cdot s \cdot photon^{-1} \tag{5.3}$$

here $P(\lambda)$ is the normalised photopic curve. To calculate the OLED EQE I now need

Table 5.2: Summary of rigid ITO vs $FeCl_3$-FLG OLEDs. $V_{L_{peak}}$ refers to the voltage at which the peak luminance occurs.

TCE material	L (cd/m^2)	CE (cd/A)	PE (lm/W)	V_T (V)	$V_{L_{peak}}$ (V)	EQE (%)
ITO (avg)	1155	0.4	0.2	4.8	6.4	0.1
(±)	(199)	(0.2)	(0.1)	(0.3)	(0.3)	(0.1)
$FeCl_3$-FLG (avg)	707	0.2	0.09	6	9	0.06
(±)	(306)	(0.09)	(0.04)	(1)	(1)	(0.03)
ITO (best)	1256	0.94	0.54	5	6.5	0.28
$FeCl_3$-FLG (best)	1131	0.31	0.15	5	7.5	0.09

to measure just the luminance, L, and the current drawn by the OLED, I_{OLED}.

With this in mind I have measured the following OLEDs using the Konica Minolta luminance meter and calculated the EQE from above.

5.3 RIGID OLED

5.3.1 *ITO*

Table 5.2 shows the summary of results of ITO-based OLEDs vs $FeCl_3$-FLG OLEDs. The devices compared here were all made in the same batch. The yield for the ITO devices was 91%, and 19% for the $FeCl_3$-FLG devices. The criteria for "working" device is luminance $> 1\ cd/m^2$, this is similar to the criteria for turn-on voltage, V_T, which occurs at the voltage required for 1 cd/m^2 luminance.[6–8] Each pixel is tested from 0 V to destruction in 0.5 V increments.

For the ITO based device, the peak values are all relatively low when compared to the literature.[9] This is especially true when the estimated EQE values are considered. The device could only achieve 0.28%. Usually reported ITO based devices achieve $\approx$ 5%[10] (up to 17.8%[11]). This is almost certainly due to the fabrication method. Solution processing using spin-coated materials is not as controlled or as clean as more evaporated materials. Evaporation is now the more common deposition method in research devices presented in the literature.[11] Another significant issue is the device processing conditions. The devices were processed partially in ambient conditions, they were not encapsulated, and the device testing was conducted in ambient conditions.

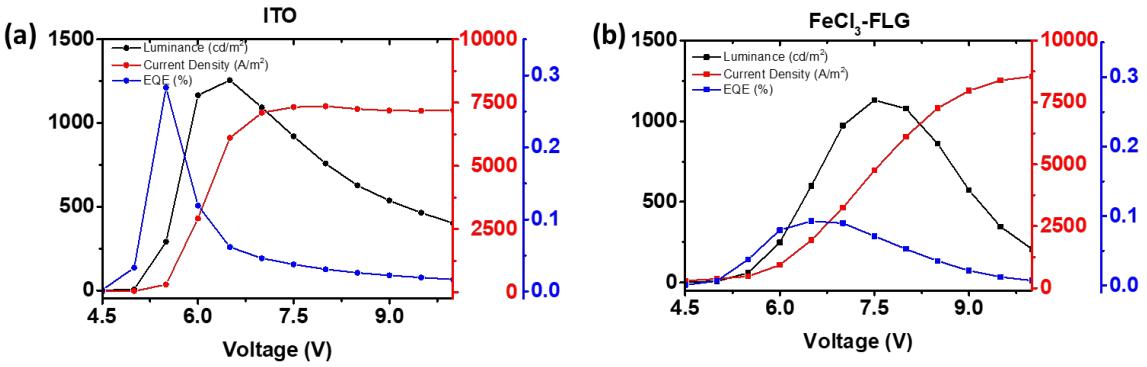

Figure 5.3: **(a)** Luminance, current density, and estimated EQE data from the best ITO based OLED in the batch. **(b)** The same data for the best $FeCl_3$-FLG OLED in the batch. Peak values for both reported in Table 5.2.

The above fabrication and testing conditions resulted in very short device lifetime.

For the unencapsulated device, due to its short lifetime, the data collection method can even make a difference. When using the Konica Minolta luminance meter, as done in Table 5.2 (Figure 5.3), the acquisition time is 7 seconds. In this time the device will partially degrade, this will be accelerated at higher bias voltages. Less degradation is seen when the acquisition time is reduced as is the case when the photodiode is used. The photodiode can measure in 0.1 s, this gives the device much less time to degrade, and the device will get much brighter before dying. This effect was observed when devices were tested using a photodiode and biased in increments as fast as possible. The resulting peak luminance and EQE were $\approx 4000\ cd/m^2$ and 1.2% respectively. Both approximately 4 times larger than when tested with the other method. This shows the importance of encapsulation and device stability which is discussed in Chapter 6.

5.3.2 *$FeCl_3$-FLG*

The $FeCl_3$-FLG based device summarised in Table 5.2 and seen in Figure 5.3 (b) shows consistently lower performance compared to the ITO based device. The peak luminance and EQE are on average 39% and 47% less for the $FeCl_3$-FLG based device. The only property that matches for both is the turn-on voltage. This low V_T suggests that the material work functions are well matched in the $FeCl_3$-FLG devices.[4] Initially it appears as if $FeCl_3$-FLG and ITO perform similarly. At higher voltages however,

Table 5.3: Summary of ITO vs $FeCl_3$-FLG properties.

	R_S ($\Omega/\square$)	T_{avg} (%)	T_{550} (%)	Φ (eV)	Flexible?
ITO (on glass)	14	95	98	-4.7	No
$FeCl_3$-FLG	110	76	71	-5.0 to -5.5	Yes
ITO (on PET)	60	92	91	-4.7	No

it is clear that the $FeCl_3$-FLG device has a very low luminance to bias ratio. This indicates high resistance, caused by the higher material resistance of $FeCl_3$-FLG. At higher voltages resistance will have a larger effect, at low voltages this is less likely to occur and hence why similar turn-on voltages are seen. To achieve the same level of brightness, the $FeCl_3$-FLG OLED is biased at a much higher voltage, at 7.5 V compared to 6 - 6.5 V, indicating high resistance. In order to maintain the same current, a much higher voltage is required.

The reduction in peak brightness is most likely caused by the transmittance of this large-area $FeCl_3$-FLG. The large-area $FeCl_3$-FLG used in these devices has a transmittance at 550 nm, $T_{550} = 71\%$. The amount by which the luminance is expected to drop due to the reduced transmittance of the electrode alone can be calculated. The expected luminance $L_{expected}$ is:

$$L_{\text{expected}} = \frac{L_{ITO}}{T_{ITO}} \times T_{FeCl_3-FLG} \tag{5.4}$$

if the values are put on this and the transmittance is assumed to be constant across all wavelengths, which is approximately true for $FeCl_3$-FLG and ITO, $T_{ITO} = 95\%$, and $L_{ITO} = 1256\ cd/m^2$, this gives $L_{expected} = 925\ cd/m^2$. This suggests that for the best devices, $FeCl_3$-FLG outperformed ITO electrically, but not optically. Electrically this device was at least 24% better than the ITO based device. This is interesting, as ITO is smoother, and has a much lower sheet resistance on glass. It is suggestive of these benefits being outweighed by the deeper $FeCl_3$-FLG work function, resulting in better energy level matching.

For the average case, where $L_{ITO} = 1155\ cd/m^2$, $L_{expected} = 837\ cd/m^2$, suggesting that on average for $FeCl_3$-FLG there are more factors causing a reduction in performance than exclusively transmittance. I estimate that 29% of the losses are these other

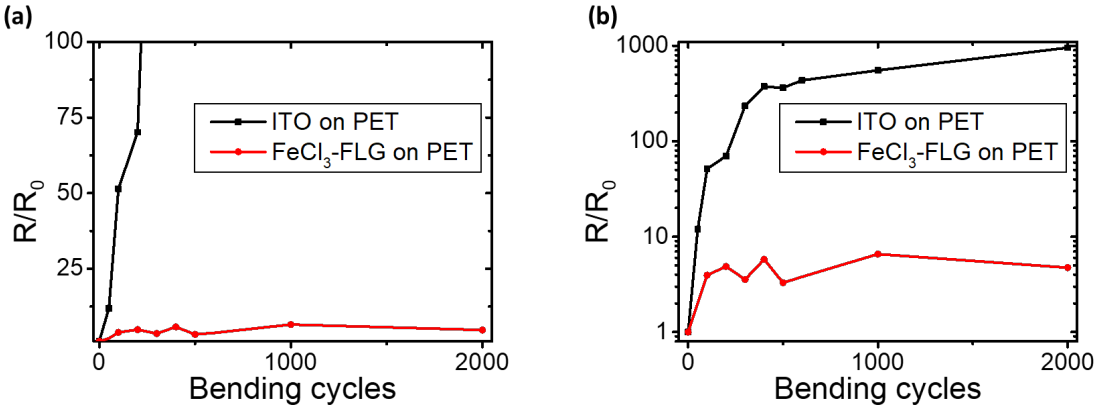

Figure 5.4: **(a)** Graph comparing the bending performance of $FeCl_3$-FLG vs ITO. The values given are a ratio of the initial value and are not absolute. **(b)** The same data as in (a), however plotted on a log 10 scale. This allows me to show the extreme degradation of ITO.

factors discussed below. These account for 16% of device performance.

The obvious area where the performance loss could be coming from is the sheet resistance of $FeCl_3$-FLG. The sheet resistance of $FeCl_3$-FLG is almost 8 times higher than for ITO. In these devices which are small ($A_{OLED} = 4.5 \times 10^{-6}\ m^2$) the dimming caused by this is not expected to be very large. This is likely the primary cause of the loss. The other major area where the losses could be occurring are regions where there are pinhole defects, caused by the underlying material roughness, or possible holes. As mentioned in Section 4.3.1, holes can take up as much as 18.5% of the few-layer graphene (FLG) surface area.

Controlling for sheet resistance is more difficult. One way in which it can be partially controlled for is to use a different substrate. While $FeCl_3$-FLG maintains its properties on polyethylene terephthalate (PET) substrate, ITO does not. The lowest sheet resistance ITO on PET available commercially has a sheet resistance of $60\Omega/\square$, over 4 times higher than when on glass. The average transmittance is reduced from 95% to 92%. The properties of both TCEs are summarised in Table 5.3.

5.4 MATERIAL FLEXIBILITY

One of the most important material properties of $FeCl_3$-FLG is its flexibility. Flexibility is a property inherent in graphene[12] and extends to $FeCl_3$-FLG. ITO on the other hand is known for its highly brittle nature.[13;14] Extensive work has been done to enhance the flexibility of ITO, using graphene,[15;16] carbon nanotubes (CNTs),[17] polymers,[18] and metal meshes and nanowires,[19] however the structural properties that give ITO its low roughness and high conductivity contribute to its brittle nature. Flexibility is an important property to compare between $FeCl_3$-FLG and ITO electrodes.

I conducted bending tests on $FeCl_3$-FLG and ITO using the bender designed and referred to in Section 4.12. For these tests small samples of $FeCl_3$-FLG were prepared using the methods described in Section 3.2.1. These samples were $FeCl_3$-FLG on PET, they were cut into 12×12 mm squares, the same size as the OLED devices will be. The samples were measured using the two-point resistance technique (Section 3.3.1.1). The pristine samples were first measured to give an initial resistance R_0. This was done by clamping samples between the two probes and measuring using a Keithley 2400 source measure unit. The samples were then bent using the custom-built roller bender discussed in Section 4.5.0.2. The samples were bent 100 times before being measured again, then bent another 100 times. This was repeated for $FeCl_3$-FLG until 500 bends were completed, then the number of bends was further increased to 1000. The results of this can be seen in Figure 5.4. Figure 5.4 (a) shows the data plotted against a linear y-axis, Figure 5.4 (b) shows the data plotted against a $log10$ y-axis. This shows the slight increase, followed by constant resistance of $FeCl_3$-FLG alongside the extreme and continuous degradation of ITO. It was anticipated that ITO might not survive as long, so it was tested initially after 50 bends. Both materials were eventually bent through 2000 cycles. The final resistance value for $FeCl_3$-FLG was $R/R_0 = 4.7$, the final resistance value for ITO was $R/R_0 = 956$. These values were where the resistances of the materials stabilised, $FeCl_3$-FLG reached $R/R_0 = 4$ after 100 bends, ITO never stabilised, the relationship between bends and R/R_0 remained linear up to 2000 bends.

This study shows the inherent flexible nature of $FeCl_3$-FLG. It proves that $FeCl_3$-FLG on a large-area flexible substrate retains its low resistance after up to 2000 bending cycles. It also shows the effect when compared to ITO. The result can be summed up

Table 5.4: Summary of rigid ITO vs ITO on PET OLEDs.

TCE material	L (cd/m^2)	CE (cd/A)	PE (lm/W)	V_T (V)	$V_{L_{peak}}$ (V)	EQE (%)
ITO on glass (avg)	1155	0.4	0.2	4.8	6.4	0.1
(±)	(199)	(0.2)	(0.1)	(0.3)	(0.3)	(0.1)
ITO on PET (avg)	481	0.3	0.1	6.8	9	0.09
(±)	(147)	(0.2)	(0.1)	(0.5)	(1)	(0.07)
Change	-58%	-15%	-38%	+43%	+39%	-15%

by the fact the resistance of ITO increases by a factor of 50 after just 100 bending cycles, while the resistance of $FeCl_3$-FLG increases by a factor of just 5 after 2000 bending cycles. This sets $FeCl_3$-FLG up to be a promising ITO replacement candidate in OLEDs and other devices which require a flexible TCE.

5.5 FLEXIBLE OLED

There are several important reasons to look at comparing these devices for flexibility. The first is the commercial relevance of flexible OLEDs. Bendable phones, tablets, and computers are now available with bendable OLED screens.[20] These devices largely use modified forms of ITO and a flexible substrate such as PET.[21;22] The devices themselves bend in an extremely controlled manner, with complex hinges, moving components, and a single, controlled line of strain.[23] Replacing ITO with a material that is truly flexible is of high importance for future emerging flexible electronic technologies.

Within this work investigating flexibility of devices is important as it gives more information about the primary contributory properties of $FeCl_3$-FLG in OLEDs. It enables me to control for and investigate the role of sheet resistance, with the sheet resistance of ITO on PET being 4 times higher than on glass.

5.5.1 *ITO*

The first way I will examine flexible OLEDs is by looking at the properties of ITO based OLEDs. These devices are fabricated in the same way as rigid OLEDs, only on a flexible ITO on PET substrate. These devices were made in a different batch; however they were made soon after the rigid OLEDs, and all of the materials were

stored in a nitrogen glovebox to prevent degradation. The results of this study can be seen in Table 5.4.

The overall efficiency of the ITO OLED on flexible substrate has reduced by 15%. More significant changes are the reduction in peak luminance (-58%) and the increase in turn-on voltage (+43%). The increase in turn-on voltage can be attributed to the increased sheet resistance of ITO on PET. Higher voltage is required to draw the same current across the electrode. The significant increase in turn-on voltage is the most interesting change in device performance. This is because the only large change in properties between rigid and flexible devices is the sheet resistance, from 14 $\Omega/\square$ to 60 $\Omega/\square$, the change in turn-on voltage is from $4.8 \pm 0.3\ V$ to $6.8 \pm 0.5\ V$, an increase of 43%. When ITO is compared to $FeCl_3$-FLG the change in turn-on voltage is from $4.8 \pm 0.3\ V$ to $5.7 \pm 1.1\ V$, an increase of just 19%. It is clear from these results that $FeCl_3$-FLG is much less affected by high sheet resistance than would be expected if it was ITO.

This effect can be quantified. I know that the increase in sheet resistance for ITO on PET and $FeCl_3$-FLG compared to just ITO on glass are 328% and 386% respectively. I also know that the increase in turn-on voltage for both is 43% and 19% respectively. So, the percentage increase in turn-on voltage per percentage increase in sheet resistance for both is 0.13 and 0.03, respectively. Therefore, I can say that the change in turn-on voltage is 4.7 times more dependent on sheet resistance in the case on ITO than it is in the case of $FeCl_3$-FLG. This indicates the superior work function is likely damping the expected negative effect of high sheet resistance in the case of $FeCl_3$-FLG electrodes.

5.5.2 *$FeCl_3$-FLG*

Although $FeCl_3$-FLG based OLEDs were successfully fabricated on glass substrates, the yield was at all times low. Often devices would short circuit as soon as they were biased, with the current immediately hitting the compliance limit. This is most likely caused by contamination on the surface of the $FeCl_3$-FLG, or just the higher surface roughness of the material.

The same problem appeared when fabricating $FeCl_3$-FLG on PET OLEDs. In total 96 $FeCl_3$-FLG on PET pixels were fabricated and tested, none worked. At the same time ITO on PET devices were always fabricated as control, of these 32% of pixels

Table 5.5: Summary of ITO OLEDs for both device architectures.

TCE material	L (cd/m^2)	CE (cd/A)	PE (lm/W)	V_T (V)	$V_{L_{peak}}$ (V)	EQE (%)
ITO (inverted) (avg)	1155	0.4	0.2	4.8	6.4	0.11
(±)	(199)	(0.2)	(0.1)	(0.3)	(0.3)	(0.07)
ITO (conventional) (avg)	1124	0.8	0.11	14	26	0.28
(±)	(773)	(0.4)	(0.06)	(4)	(5)	(0.14)
Difference	-3%	+128%	-47%	+196%	+301%	+150%

fabricated and characterised worked.

5.6 ALTERNATIVE ARCHITECTURE

The inverted $FeCl_3$-FLG OLEDs fabricated so far had shown low yield on glass substrate and failed to work entirely on PET substrate. For this reason, a new device architecture was introduced. This is the conventional device structure which was discussed in Section 3.2.2.2. The structure of this device is $FeCl_3$-FLG or ITO, PEDOT:PSS, TFB, F8:F8BT, Liq, aluminium. The device and its energy levels can be seen in Figure 3.3 (b).

One of the primary reasons for choosing this structure, conventional in particular, was to better match the work function of $FeCl_3$-FLG with its adjacent layer. The energy barrier in this new device is 0.2 eV, as opposed to 1.4 eV in the previous device. This should mean that this new device structure slightly favours $FeCl_3$-FLG electronically. The overall device thickness is slightly less however, which may make it more susceptible to roughness. In the previous inverted device, the active layer was $\approx$ 200 nm thick, in this device it is just 80 nm.

Investigating this architecture operating with a rigid ITO electrode the very large turn-on voltage is clearly seen. When compared to the inverted device (in Table 5.5) the major parameter differences are the voltages, with both the turn-on, and the voltage at peak luminance being over two times higher. The turn-on voltage has risen from 4.8 V to 14 V, while the voltage at peak luminance has risen from 6.4 V to 26 V. This is indicative of a large energy barrier in this device that can only be overcome by very high voltage. Despite this high voltage requirement, the average EQE of the conventional device is 150% better than the inverted device at 0.28% compared to

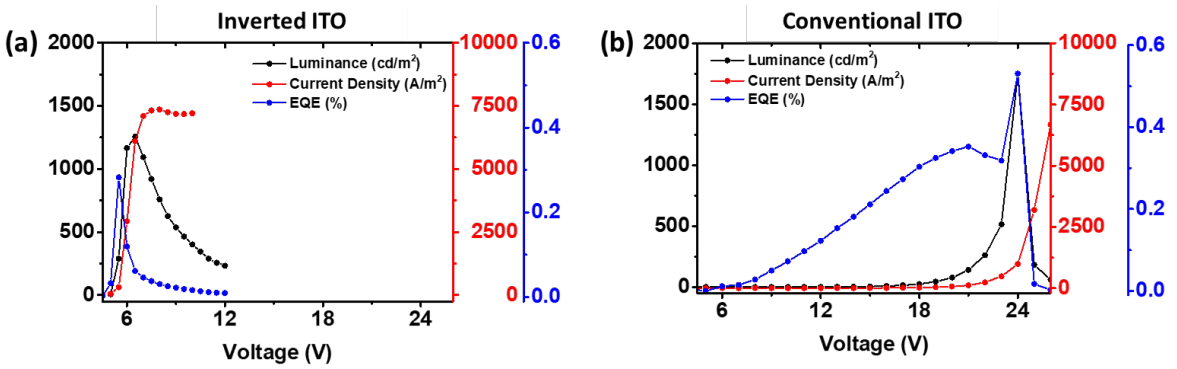

Figure 5.5: **(a)** J-V-L curve and EQE of the inverted device, this device has a low turn-on voltage and operating range. Stopped measurement at 12 V. **(b)** J-V-L curve and EQE of the conventional device, this device has a much higher turn-on voltage and operating range.

0.11%.

The much higher operating voltage can be clearly seen in the J-V-L curve in Figure 5.5. What is also notable is the very large working range. The EQE remains much higher for much longer in the case of the conventional device structure. This is the first indication of the enhanced stability of this device architecture, an important parameter for measuring device bending, and other parameters such as EL and emission angle.

As with the inverted device, all flexible devices fabricated with $FeCl_3$-FLG electrode failed. The reason for this can be attributed to the same as in the case of inverted devices. The roughness issue was likely more acute due to the thinner active layer; however the work functions were better matched and this should have contributed to a higher device performance when using $FeCl_3$-FLG. Overall, the efficiency of the flexible ITO based conventional device was better and more stable than previous.

While it was not possible to fabricate OLEDs using primarily solution processed materials, they were fabricated by Dr Liping Lu (for an as yet unpublished work where I am a joint first author), using primarily evaporated materials, on rigid substrates (Figure 5.6). In this case the MoO_3 (as opposed to MoO_3:PEDOT:PSS), and calcium were evaporated in inert atmosphere systems.

Device performance was assessed by looking at J-V-L curves and calculating current efficiency (CE) from them. The conventional device performance based on $FeCl_3$-FLG and ITO are very similar, and their J-V-L curves are nearly overlapping, the FLG

based device however demonstrates a significantly lower efficiency. The efficiency of the conventional device is not as good as the inverted device, therefore focus is shifted to the inverted device, as the inverted structure appears to be optimal for all devices.

Figure 5.6 (c), (d), (e) and (f) shows the CE and J-V-L curve of an inverted structure based on the $FeCl_3$-FLG and ITO. Here a more consistent J-V-L curve for sequential measurements of the same pixel of $FeCl_3$-FLG based devices compared to ITO based is seen. It even improves slightly after 3 sequential measurements of the same pixel. This indicates the stability of $FeCl_3$-FLG based devices are better, as these devices are all tested in ambient conditions. This is likely due to the impermeability of the graphene layers. The peak CE of the $FeCl_3$-FLG devices is also better than the ITO equivalent, with CE above 20 cd/A compared to ITO's 15 cd/A. The current turn-on and luminance turn-on voltage is observed at around 4 V which is higher than the results from previous studies.[24–29] This is likely due to the process of how ZnO thin film is deposited. In previous studies, the ZnO layer is deposited via spray pyrolysis at a temperature of 400°C which would allow for the uniform formation of relatively good crystallites.[30] Aluminium doped zinc oxide (AZO) is spin-coated, this quick process might not allow the enough time for a formation of good crystallites and/or a uniform coverage of ZnO on the ITO surface. Nevertheless, the performance of the electrodes is the interest here and this ZnO effect should have the same impact on the performance of all electrodes presented.

Since intercalation of $FeCl_3$-FLG varies from position to position due to its patchwork structure, ranging from single layer to six layers as indicated by Raman spectra, it is necessary to understand whether there is a big discrepancy in device performance on the macroscopic scale. Figure 5.6 (g), (h), (i) and (j) illustrate the J-V-L characterisation and CE of the inverted structure based on $FeCl_3$-FLG and ITO with F8BT film thickness of 200 nm at different positions. The results show that the current density and luminance for different pixels on the same devices partially overlap in the case of devices based on $FeCl_3$-FLG, hence a good uniformity over the surface of $FeCl_3$-FLG. It is also clear that their efficiency is very similar and, in some cases, better than devices with ITO as cathode. Though the devices based on ITO shows similar efficiency on different pixels, there is still a discrepancy in the current density and luminance from different pixels on the same device as indicated in Figure 5.6 h.

In general, the inverted devices all perform better than the conventional devices.

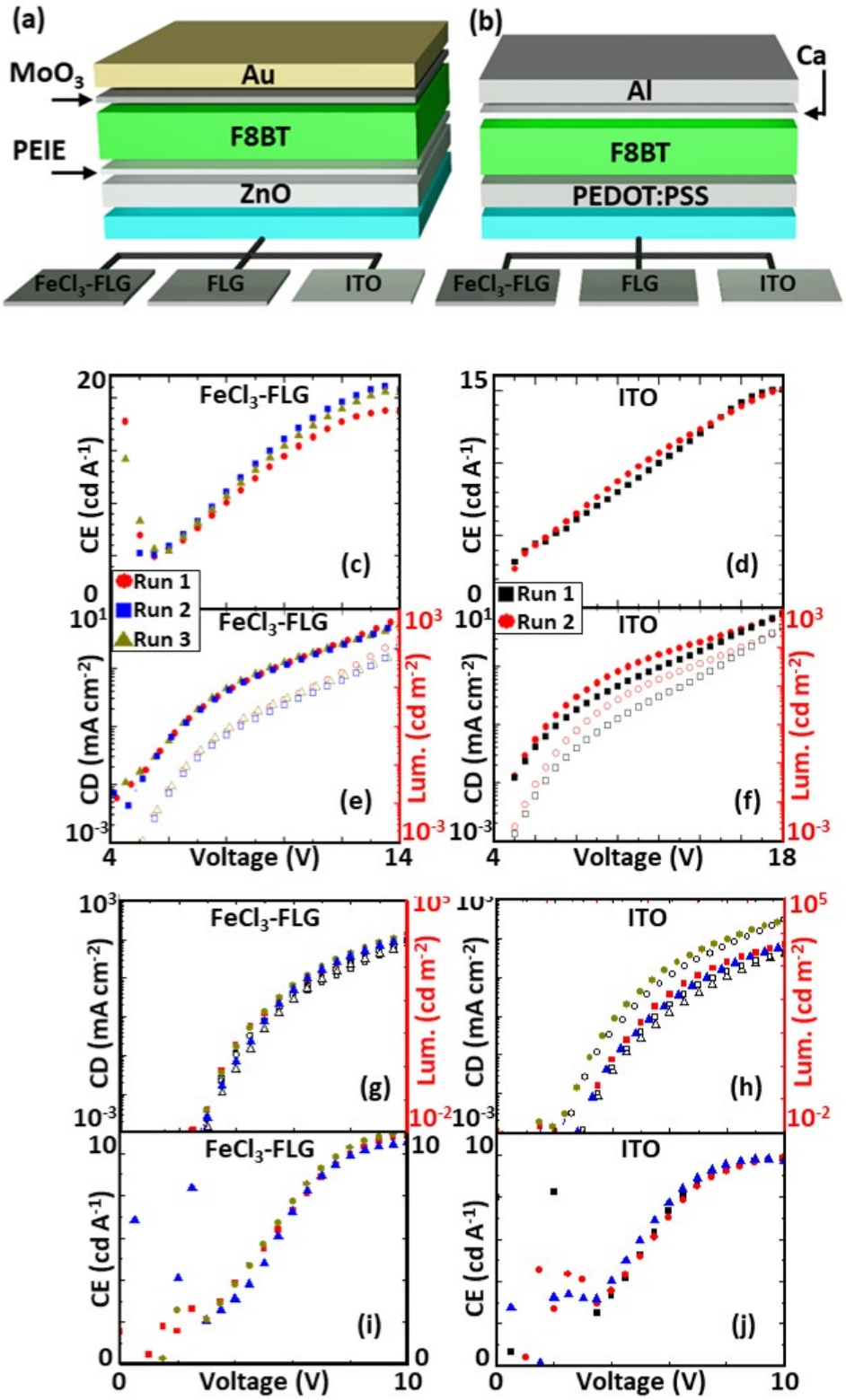
(a)
MoO3
Au
F8BT
PEIE
ZnO
FeCl3-FLG
FLG
ITO
(b)
Ca
Al
F8BT
PEDOT:PSS
FeCl3-FLG
FLG
ITO
FeCl3-FLG
CE (cd A-1)
(c)
Run 1
Run 2
Run 3
CD (mA cm-2)
Lum. (cd m-2)
(e)
Voltage (V)
ITO
(d)
Run 1
Run 2
(f)
(g)
(h)
(i)
(j)

Figure 5.6

Figure 5.6: The architecture of inverted devices **(a)** and conventional devices **(b)** with $FeCl_3$-FLG, FLG and ITO as bottom electrodes, respectively. J-V-L curves and current efficiency for sequential measurements, run 1, 2 (and 3), in inverted devices with $FeCl_3$-FLG, **(c)** & **(e)**, and ITO, **(d)** & **(f)** as cathodes. Unfilled points correspond to the luminance axis. The J-V-L characterization of the inverted structure on $FeCl_3$-FLG **(g)** & **(i)**, and ITO **(h)** & **(j)**, where each colour corresponds to a different location on the electrode. Although $FeCl_3$-FLG has a patchwork structure and film thickness from single layer to 5 layers, the results show that the current density and luminance at different positions on the devices almost overlap with each other. This demonstrates good uniformity across the surface of $FeCl_3$-FLG. The devices on ITO show similar efficiency, however there is still a variation in current density and luminance at different positions across the ITO substrate. In **(g)**, **(h)**, **(e)** & **(f)** unfilled data points correspond to luminance and filled to CD or CE.

The device performance based on $FeCl_3$-FLG in inverted structures appears better than that based on ITO, and ITO based devices outperform devices based on FLG. In the case of conventional structure, $FeCl_3$-FLG and ITO based devices show very similar performance whereas devices based on FLG have a lower current efficacy. The fact that conventional structures give lower efficiency compared to inverted structures, is very different from the previous studies using this architecture, where devices with both conventional and inverted structure show similar efficiency.[24–29] This might have to do with the different choices of poly(3,4-ethylenedioxythiophene) polystyrene sulfonate (PEDOT:PSS). Nevertheless, $FeCl_3$-FLG is shown to be more efficient, and more consistent across a 70 mm^2 area, than ITO and pristine FLG.

In summary, from all the rigid devices made here, in general the current efficacy on $FeCl_3$-FLG is similar or slightly higher than on ITO and the brightness of devices with $FeCl_3$-FLG electrodes is similar or slightly lower than on ITO. This agrees with what would be expected given that the transmittance of $FeCl_3$-FLG in visible range is lower than that of ITO. The transmittance of $FeCl_3$-FLG is lowest around the wavelength of 400 nm to 550 nm and as the peak luminance of F8BT is centred on 535 nm, it follows that $FeCl_3$-FLG OLEDs based on yellow or red emitting polymer should perform even better than those shown on F8BT. These devices should therefore more comfortably

outperform ITO based devices.

5.7 SUMMARY AND OUTLOOK

I have investigated the role of $FeCl_3$-FLG in solution processed (spin coated) OLED devices. These devices were fabricated in ambient and inert environments, they were not encapsulated for testing.

OLED devices were first fabricated, then characterised to ensure expected parameters, such as layer thickness, matched the recipe. The transmittance of the electrodes was also measured and verified with previous works.

The first devices characterised were those with an ITO TCE on rigid glass substrate. The emission angle profile was measured to compare it to the expected Lambertian emission. The difference will act as a correction factor on estimating the EQE without an integrating sphere. To estimate the EQE itself (defined in Equation 4.12) I measured the EL spectrum of the device. This EL spectrum was assumed to be the same for the $FeCl_3$-FLG device, as the transmittance spectrum of $FeCl_3$-FLG is approximately flat.

Rigid ITO and $FeCl_3$-FLG devices were then measured and compared. I reported that the peak luminance and EQE are 39% and 47% less for the $FeCl_3$-FLG based device. This significant reduction in performance is likely caused by the low material transmittance, pinholes caused by the high roughness, and the lack of encapsulation exacerbating that issue. I noted that the $FeCl_3$-FLG based device was brighter than expected for the low transmittance. I also noted that the turn-on voltage was equal to the ITO based device. This is indicative of good work function matching, despite the other issues.

I then moved onto flexible substrates. First the TCEs were characterised for bending performance. I found that the resistance of ITO increases by a factor of 50 after just 100 bending cycles, while the resistance of $FeCl_3$-FLG increases by a factor of just 5 after 2000 bending cycles. $FeCl_3$-FLG is clearly a superior flexible conductor.

OLEDs were then examined on flexible PET substrates. Here the performance of the ITO device was reduced compared to the rigid device, likely due to the increased surface roughness and sheet resistance of the substrate and TCE. I was unable to fabricate a working $FeCl_3$-FLG device on PET. Most likely for the same roughness related reason.

I then examined OLEDs using an alternative architecture, these devices used the conventional device structure. For ITO devices this resulted in a large increase in performance, EQE increased by 150%. This device structure was chosen so as to better match the work function of $FeCl_3$-FLG. The failure of $FeCl_3$-FLG based devices here is again likely due to the surface roughness. The layers in this architecture were thinner than the last, making it more sensitive to high surface roughness.

Finally, I examined the unreported work carried out by a colleague using devices which involved the evaporation of MoO_3, and calcium. Here, in contrast with the solution processed work, the inverted devices showed better performance. The $FeCl_3$-FLG based devices outperformed the ITO based devices and showed better uniformity. The $FeCl_3$-FLG used in this work was prepared in the same way, only the device fabrication was different. It indicates device related issues, not exclusively TCE. Nonetheless in this work, the TCE appeared to be the common cause of failure. It is therefore extremely important to attempt to mitigate the effects of a rough TCE and also find a way of obtaining a smoother film.

BIBLIOGRAPHY

[1] Sukanta De and Jonathan N. Coleman. Are there fundamental limitations on the sheet resistance and transmittance of thin graphene films? *ACS Nano*, 4(5):2713–2720, 5 2010.

[2] Yulong Shen, Ahmad R. Hosseini, Man Hoi Wong, and George G. Malliaras. How to make ohmic contacts to organic semiconductors. *ChemPhysChem*, 5(1):16–25, 1 2004.

[3] G. G. Malliaras and J. C. Scott. The roles of injection and mobility in organic light emitting diodes. *Journal of Applied Physics*, 83(10):5399–5403, 4 1998.

[4] I. Wen Wu, Yu Hung Chen, Po Sheng Wang, Chao Gong Wang, Shu Han Hsu, and Chih I. Wu. Correlation of energy band alignment and turn-on voltage in organic light emitting diodes. *Applied Physics Letters*, 96(1):013301, 1 2010.

[5] Help Online - Origin Help - BiHill.

[6] Xinxin Ban, Kaiyong Sun, Yueming Sun, Bin Huang, and Wei Jiang. Enhanced Electron Affinity and Exciton Confinement in Exciplex-Type Host: Power Efficient Solution-Processed Blue Phosphorescent OLEDs with Low Turn-on Voltage. *ACS Applied Materials and Interfaces*, 8(3):2010–2016, 1 2016.

[7] Guohua Xie, Yanlong Meng, Fengmin Wu, Chen Tao, Dandan Zhang, Mingjun Liu, Qin Xue, Wen Chen, and Yi Zhao. Very low turn-on voltage and high brightness tris-(8-hydroxyquinoline) aluminum-based organic light-emitting diodes with a Mo Ox p -doping layer. *Applied Physics Letters*, 92(9):093305, 3 2008.

[8] C. C. Yap, M. Yahaya, and M. M. Salleh. Influence of thickness of functional layer on performance of organic salt-doped OLED with ITO/PVK:PBD:TBAPF6/Al structure. *Current Applied Physics*, 8(5):637–644, 8 2008.

[9] Jinouk Song, Kwon Hyeon Kim, Eunhye Kim, Chang Ki Moon, Yun Hi Kim, Jang Joo Kim, and Seunghyup Yoo. Lensfree OLEDs with over 50% external quantum efficiency via external scattering and horizontally oriented emitters. *Nature Communications*, 9(1):1–10, 12 2018.

[10] Alessandro Minotto, Paul A. Haigh, Łukasz G. Łukasiewicz, Eugenio Lunedei, Daniel T. Gryko, Izzat Darwazeh, and Franco Cacialli. Visible light communication with efficient far-red/near-infrared polymer light-emitting diodes. *Light: Science and Applications*, 9(1):1–11, 4 2020.

[11] Bo Ram Lee, Eui Dae Jung, Ji Sun Park, Yun Seok Nam, Sa Hoon Min, Byeong Su Kim, Kyung Min Lee, Jong Ryul Jeong, Richard H. Friend, Ji Seon Kim, Sang Ouk Kim, and Myoung Hoon Song. Highly efficient inverted polymer light-emitting diodes using surface modifications of ZnO layer. *Nature Communications*, 5(1):1–8, 9 2014.

[12] U. Stöberl, U. Wurstbauer, W. Wegscheider, D. Weiss, and J. Eroms. Morphology and flexibility of graphene and few-layer graphene on various substrates. *Applied Physics Letters*, 93(5):051906, 8 2008.

[13] Zhong Chen, Brian Cotterell, and Wei Wang. The fracture of brittle thin films on compliant substrates in flexible displays. *Engineering Fracture Mechanics*, 69(5):597–603, 3 2002.

[14] Khalid Alzoubi, Mohammad M. Hamasha, Susan Lu, and Bahgat Sammakia. Bending fa-

tigue study of sputtered ITO on flexible substrate. *IEEE/OSA Journal of Display Technology*, 7(11):593–600, 11 2011.

[15] Tae Hee Han, Min Ho Park, Sung Joo Kwon, Sang Hoon Bae, Hong Kyu Seo, Himchan Cho, Jong Hyun Ahn, and Tae Woo Lee. Approaching ultimate flexible organic light-emitting diodes using a graphene anode. *NPG Asia Materials*, 8(9), 2016.

[16] Ning Li, Satoshi Oida, George S. Tulevski, Shu Jen Han, James B. Hannon, Devendra K. Sadana, and Tze Chiang Chen. Efficient and bright organic light-emitting diodes on single-layer graphene electrodes. *Nature Communications*, 4(1):1–7, 8 2013.

[17] Wenya Xu, Jianwen Zhao, Long Qian, Xianying Han, Liangzhuan Wu, Weichen Wu, Minshun Song, Lu Zhou, Wenming Su, Chao Wang, Shuhong Nie, and Zheng Cui. Sorting of large-diameter semiconducting carbon nanotube and printed flexible driving circuit for organic light emitting diode (OLED). *Nanoscale*, 6(3):1589–1595, 1 2014.

[18] Yong Hyun Kim, Jonghee Lee, Simone Hofmann, Malte C. Gather, Lars Müller-Meskamp, and Karl Leo. Achieving high efficiency and improved stability in ITO-free transparent organic light-emitting diodes with conductive polymer electrodes. *Advanced Functional Materials*, 23(30):3763–3769, 8 2013.

[19] So Ra Shin, Hock Beng Lee, Won Yong Jin, Keum Jin Ko, Sunghee Park, Seunghyup Yoo, and Jae Wook Kang. Improving light extraction of flexible OLEDs using a mechanically robust Ag mesh/ITO composite electrode and microlens array. *Journal of Materials Chemistry C*, 6(20):5444–5452, 5 2018.

[20] Flexible OLEDs: introduction and market status — OLED-Info.

[21] Sung Il Kim, Kyo Woong Lee, Bibhuti Bhusan Sahu, and Jeon Geon Han. Flexible OLED fabrication with ITO thin film on polymer substrate. *Japanese Journal of Applied Physics*, 54(9):090301, 9 2015.

[22] Zhenlin Yang, C. Cheng, Xudong Pan, Fei Pan, Fei Wang, Mengying Tian, and Hongmei Zhang. Effects of hole injection layer on performance of green OLEDs based on flexible ITO. *Materials Chemistry and Physics*, 239:121828, 1 2020.

[23] Samsung Shows Off New Foldable OLED Tech - ExtremeTech.

[24] Dinesh Kabra, Li Ping Lu, Myoung Hoon Song, Henry J. Snaith, and Richard H. Friend. Efficient single-layer polymer light-emitting diodes. *Advanced materials*, 22(29):3194–3198, 8 2010.

[25] Li Ping Lu, Chris E Finlayson, and Richard H Friend. A study of tin oxide as an election injection layer in hybrid polymer light-emitting diodes. *Semiconductor Science and Technology*, 29(12):125002, 10 2014.

[26] Li Ping Lu, Chris E. Finlayson, Dinesh Kabra, Sebastian Albert-Seifried, Myoung Hoon Song, Remco W.A. Havenith, Guoli Tu, Wilhelm T.S. Huck, and Richard H. Friend. The influence of side-chain position on the optoelectronic properties of a red-emitting conjugated polymer. *Macromolecular Chemistry and Physics*, 214(9):967–974, 5 2013.

[27] Li Ping Lu, Chris E Finlayson, and Richard H Friend. Thick polymer light-emitting diodes

with very high power efficiency using Ohmic charge-injection layers. *Semiconductor Science and Technology*, 29(2):025005, 1 2014.

[28] Li Ping Lu, Dinesh Kabra, and Richard H. Friend. Barium hydroxide as an interlayer between zinc oxide and a luminescent conjugated polymer for light-emitting diodes. *Advanced Functional Materials*, 22(19):4165–4171, 10 2012.

[29] Li Ping Lu, Dinesh Kabra, Kerr Johnson, and Richard H. Friend. Charge-carrier balance and color purity in polyfluorene polymer blends for blue light-emitting diodes. *Advanced Functional Materials*, 22(1):144–150, 1 2012.

[30] Jewel Kumer Saha, Ravindra Naik Bukke, Narendra Naik Mude, and Jin Jang. Significant improvement of spray pyrolyzed ZnO thin film by precursor optimization for high mobility thin film transistors. *Scientific Reports*, 10(1):1–11, 6 2020.

6

NOVEL ENCAPSULATION OF OLEDS

6.1 INTRODUCTION

The flexible $FeCl_3$ intercalated FLG ($FeCl_3$-FLG) based organic light-emitting diodes (OLEDs) showed poor performance, the most significant part of this was put down to roughness, the pinholes that this causes, and therefore the ability of moisture and oxygen (ambient conditions) to enter the device.

One of the biggest problems with current OLED materials is their fast degradation in ambient conditions.[1] This is caused by moisture and oxygen in the atmosphere.[2] For this reason, commercially all OLEDs and photovoltaics (PVs) are fabricated in inert environments.[3] It is for the same reason that I have attempted to conduct as much fabrication as possible in the inert environment of a nitrogen glovebox. In commercial processes the final step is to encapsulate the device, usually using atomic layer deposition (ALD) of Al_2O_3 or using Barix technology.[4] The latter is a method that involves laying down alternating films of organic and inorganic films as barrier layers. This is done to prevent further device degradation after fabrication and extend the lifetime of the device.

One of the problems when measuring emission angle or electroluminescence (EL) spectra, which require constant luminance, is the variability of device performance over time. When one of the encapsulated devices which was biased at a constant 20 V is examined, a large change in luminance over time is seen (Figure 6.1 (b)). The device takes up to 2 hours to reach peak performance, before starting several hours of degradation. For measurements which require stable luminance this is not useful. I therefore measured devices at constant luminance, this is discussed in Section 6.4.3.

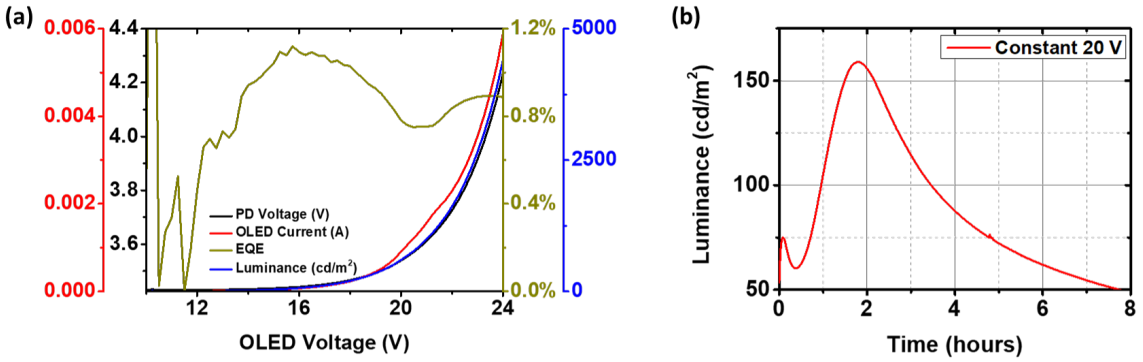

Figure 6.1: **(a)** OLED data taken using a photodiode rather than calibrated luminance meter. Each data point could be taken much quicker, resulting in a higher luminance than usual. **(b)** Graph showing the luminance of an encapsulated device biased at a constant 20 V over time. The device is very slow to come up to peak luminance, indicating a large, time dependant device evolution.

One way to mitigate against the fast degradation and variability of OLED devices is to measure the device quickly. This may be appropriate when peak performance numbers are sought. This is seen when I measured the device with a photodiode, rather than the usual calibrated luminance meter which takes 7 seconds to acquire each data point. Figure 6.1 (a) shows values of peak luminance and external quantum efficiency (EQE) which are much higher than is usually seen for this architecture. This is due to the very fast measurement, 0.1 seconds per data point. The peak luminance, when taken this way, was the highest I recorded from over working 470 devices tested. This method is not practical for measuring emission angle, or EL spectra.

The only reliable way to stabilise the device performance and protect from degradation is to encapsulate the device. I have attempted several methods in this chapter, getting remarkable results from a simple wax based encapsulation.

6.2 DEGRADATION FACTORS

OLEDs are extremely sensitive to many operational conditions, these include: oxygen and moisture permeation, heat, light, and electric field. When heat, light, and electric field are considered, there is not much that can be done. Devices must be biased in order to operate, so an electric field will always be present, degradation caused by this cannot

be easily remedied. Heat and light too result directly from device operation, heat may be able to be transported away from the device efficiently, however light degradation will always persist. External factors such as oxygen and moisture permeation can be effectively controlled for however using encapsulation.

The most serious obstacle restricting the commercialisation of OLEDs further is degradation.[4] Therefore overcoming this issue on all scales, from the lab to fab is extremely important. To do this the degradation mechanism oxygen and moisture has on a device must be understood. There are several mechanisms that have been proposed, all play at least some part in the degradation. These are oxidation, of the metal electrode with the device layers leading to the oxidation of hydrogen,[5] and the oxidation of the organic layers themselves.[6] These have been shown to be related to the formation of dark spots on the device.[7–10] These dark spots result in the areas in which pinholes occur. These form around impurities or contaminants from the fabrication process. Shadows then form around these points, this is due to water and oxygen ingress through the pinhole, increasing the size of the dead zone.[4]

6.3 ENCAPSULATION CLASSIFICATION

By encapsulating devices, they can be sealed in an airtight environment and protected from oxygen and water ingress, the volatile decomposition of the organic layers can also be prevented, even when the decomposition reaction is not fully reversible.[4]

Any encapsulation method should satisfy some basic requirements. The material should have a high dielectric constant, be highly transparent, resistant to ultraviolet (UV) and thermal irradiation, be inert, and have high mechanical strength.[11;12]

The ability to prevent oxygen and moisture entering the device is of particular importance. There are minimum requirements generally recognised for commercial devices. I have not categorised my materials in this way, however it is nonetheless important to recognise the minimum standard. The recognised maximum water vapour transmission rate (WVTR) value for OLEDs is 10^{-6} g/m^2/day.[13] The maximum oxygen transmission rate (OTR) value is $10^{-3} - 10^{-5}$ cm^3/m^2/day/atm

Considering encapsulation itself, it can be broken down into two categories, these are cover encapsulation, and film encapsulation. Cover encapsulation involves sealing the device with a cover or lid using an adhesive. Film encapsulation is when a barrier

film is deposited onto the device to protect it. I will discuss both in this work. Glass cover slip with UV epoxy is an edged-cover encapsulation, along with lamination, wax encapsulation is a form of film encapsulation. One of the primary differences between the two is the ability of film encapsulation to transfer heat away from the device, helping to prevent thermal degradation.[4]

One of the most common encapsulation techniques is ALD of Al_2O_3. This is known for its flexible, ultra-thin, pinhole-free micro-structure, and accuracy of deposition.[4]

In laboratory settings ALD of Al_2O_3 is common, however, the ALD deposition process usually requires long processing times, meaning ALD is not always practical in commercial settings.[4] More commonly in laboratory settings a glass cover slide is placed onto the device and glued in place using a UV-cured optics grade epoxy.[4] In this section I attempted to extend the lifetime and stability of my devices through various methods. The UV method uses glass, and so is never relevant for flexible devices, ALD is often used when flexibility is required. I attempted this method with rigid devices, nonetheless. I also attempted a method involving "laminating" a plastic encapsulation layer onto the device, and finally I attempted to use a flexible wax encapsulation layer, this was applied wet and offers total device coverage.

6.4 ENCAPSULATION METHOD

6.4.1 *UV epoxy and coverslip*

The first way in which OLEDs are encapsulated is the easiest laboratory encapsulation technique, with UV epoxy and a glass coverslip. The cover slip is made from diced standard microscope slides into a rectangle measuring $7 \times 10\ mm$. This is just large enough to cover the same area as the transparent conductive electrode (TCE), while leaving the contacts exposed. In this configuration moisture and oxygen ingress may be possible at the edges, however it is essential to leave the contacts uncontaminated with epoxy. This pattern can be seen in Figure 6.2 (a). The epoxy used is "Encapsulation Epoxy for Photovoltaics and OLEDs" (Ossila - E132).

When the OLEDs are fabricated in the way described in Section 3.2.2, they are sealed in a moisture barrier bag in an inert atmosphere. The encapsulation takes place in ambient conditions in a cleanroom. The bag is opened at the last possible moment. A single drop of epoxy is dropped onto the centre of the device before the coverslip is

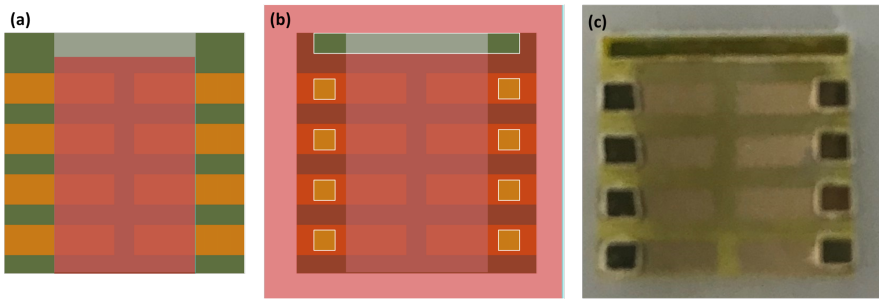

Figure 6.2: **(a)** The encapsulation pattern used in the UV epoxy and glass coverslip encapsulation method. The red area is the encapsulated area, the rest of the device is exposed to allow access to the contacts. **(b)** The encapsulation pattern used in the laminator encapsulation method. The whole device is encapsulated except small holes which are laser cut to allow access to the contacts. **(c)** Photograph of the real device after lamination.

placed on top. The coverslip is adjusted so it is in the centre and allowed to settle for a few seconds. This allows the epoxy to spread out under the cover slip. The device is then loaded into a Kloé UV-KUB 2. The UV source is set at full sample exposure, at 100% power for 5 minutes.

The device is then removed from the UV source and placed into a desiccator until it is characterised. This is done to ensure minimal degradation between long lifetime testing.

The major downside to encapsulation with a glass coverslip is the loss of flexibility. Therefore, some flexible encapsulation technique is highly sought after.

6.4.2 *Laminator encapsulation*

Encapsulation has been shown to improve device flexibility on its own.[14] So, a flexible alternative was desired to help improve the performance of OLEDs on polyethylene terephthalate (PET). Additionally, an encapsulation method that reduced the size of the encapsulation edges was sought.

The solution was to laser pattern standard office laminator sheets. These are 150 μm thick and have a heat activated glue, and fuse together creating a sealed enclosure at just 110°C. This might seem to violate the principle that OLEDs are very sensitive to heat, however OLEDs have been encapsulated successfully with thermally activated (100°C) adhesives before.[15] The pattern used allowed a much smaller open area for the

contacts to access the electrodes. This pattern can be seen in Figure 6.2 (b).

The OLEDs on PET were made in the way described in Section 3.2.2. They are then sealed in a moisture barrier bag in an inert atmosphere. The encapsulation takes place in ambient conditions in a cleanroom. The bag is opened at the last possible moment. The OLED is slid into the patterned laminator sheet pouch. The pouch is held between two sheets of paper to prevent it getting lost in the rollers of the laminator. The pouch and sheets are then sent through the laminator (Swordfish 40352), which is set to 110°C. The device is placed into a desiccator before testing.

One of the issues that occurred with the laminator encapsulation was ensuring the encapsulation layer always remained adhered to the sample. Therefore, it is necessary to continue to investigate more encapsulation methods.

6.4.3 *Wax encapsulation*

A different way of encapsulating the entire device involves wax encapsulation. This is a form of film encapsulation, like ALD encapsulation. In this form of encapsulation, the layer is adhered extremely well to the sample, and there is no way for air or moisture to get in, or for volatile gasses to escape. This form of encapsulation traditionally has excellent thermal transport properties.[4]

This involves coating the sample in beeswax. The sample is masked off to protect the contacts using dicing tape. The exposed region, the same as in Figure 6.2 (a), is used. The samples are spin-coated in a cleanroom environment and then baked on a hot plate at 80°C. The dicing tape which acts as a mask is gently peeled off to reveal the contacts. The device is placed into a desiccator before testing.

Over a very long time, this method may be limited by how soft the material is, and the oxygen permeability of the wax. Pinholes may form in the film, limiting its lifetime.

6.5 RESULTS

As this study was on improving the stability of the OLED devices, and not on electrode performance, the indium tin oxide (ITO) based OLEDs were used. These were used in the conventional configuration.

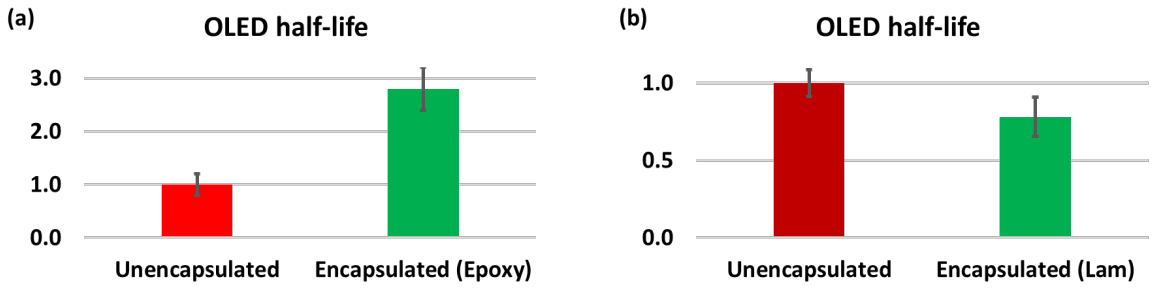

Figure 6.3: **(a)** The half-life of the epoxy encapsulated devices is compared relative to the half-life of unencapsulated devices from the same batch. **(b)** The same comparison for devices encapsulated using the laminator method.

6.5.1 *UV epoxy and coverslip*

The devices which were encapsulated using epoxy, and the devices encapsulated using the laminator method were tested in the same way. A test device from the batch was first characterised from 0 V to failure. The voltage required to power it to 80% of peak luminance was chosen to do the lifetime tests. The lifetime tests were then carried out by holding the device at this voltage until the luminance fell by half, to $L_{1/2}$. This way the half-life of the OLED could be calculated. The half-life, $t_{1/2}$, is given in Equation 6.1:

$$t_{1/2} = t_{L_{1/2}} - t_{L_{max}} \tag{6.1}$$

where $t_{L_{1/2}}$ is the time it takes for the luminance to fall to half its peal value, and $t_{L_{max}}$ is the time at which the luminance was at its peak value.

The half-life of devices tested with epoxy encapsulation was shown to be 2.8 ± 0.4 times longer than unencapsulated devices from the same batch. This is seen in Figure 6.3 (a), which shows the improvement in performance gained by using the conventional encapsulation technique. It should be noted however that the yield of devices tested using this method was low, with many devices seemingly failing in the same way. Scorch marks were observed on the device itself, suggesting very poor thermal performance. This is something that is often observed when encapsulating devices in this way.[16] Often a solution to this is to use a glass cap, filled with a getter that can dissipate heat, this could be in the form of a liquid getter.[16] As with all devices encapsulated in this way, this method does not allow for flexible devices. It is therefore necessary to

investigate an alternative encapsulation method.

6.5.2 *Laminator encapsulation*

The half-life of devices encapsulated using the laminator method were shorter than the unencapsulated devices from the same batch. These devices showed a half-life that was just 0.8 ± 0.1 times the unencapsulated device. This can be seen in Figure 6.3 (b). The devices in this configuration were more covered than those with epoxy encapsulation, so they were expected to produce better results. The likely reason for the poor results is the thermally activated glue in the lamination sheets. The glue was not sufficiently strong enough to bond with the device layers below. The lamination sheet could be seen to be lifting off the surface. This is likely what lead to equivalent lifetime to the unencapsulated reference. As the lamination sheet lifted off, in some instances it was seen to peel up device layers, especially the electrodes. This is most likely what lead to the reduced performance compared to the reference devices.

It is possible that some of these issues could be solved in future with stronger glue. For commercially available lamination paper however, the glues used are not published. This would make a further study of this technique extremely difficult. If it works however, it could provide an extremely simple and cheap way of encapsulating flexible OLED devices on the laboratory scale.

6.5.3 *Wax encapsulation*

The longevity of devices encapsulated with wax were analysed differently to those using epoxy or the lamination method. This was because these devices were more stable and so a more relevant method could be used.

The devices tested in this section had their luminance constantly measured. If the luminance fell above or below 105 or 95 cd/m^2, the voltage was adjusted down or up by 0.1 V until the luminance was back within that range. This adjustment was carried out automatically by a LabVIEW script. The luminance, voltage, and current were measured at all times. The initial luminance was chosen so as the device would be close to, but not over 100 cd/m^2, to prevent damage. This was done by first measuring a device from 0 V to failure. When the device can no longer sustain 95 cd/m^2 despite increasing voltage then the device is declared failed, and the failure time is recorded

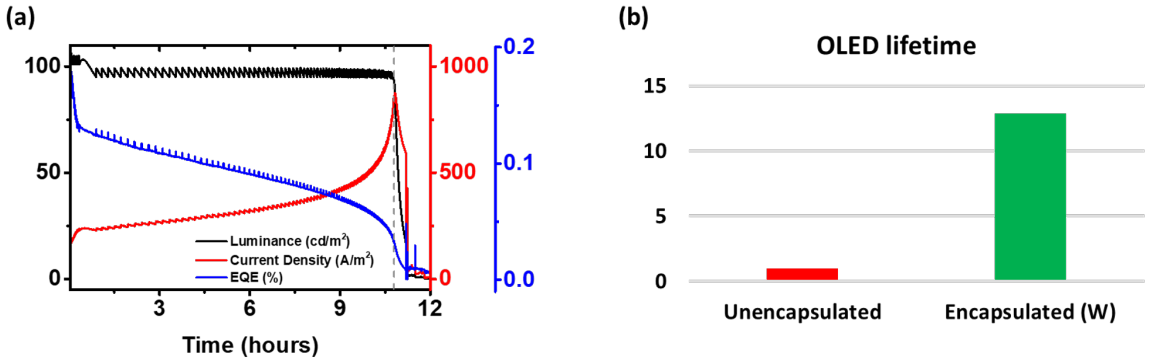

Figure 6.4: **(a)** The J-L curve of an encapsulated OLED undergoing lifetime testing. The dashed grey line shows where the device fails to remain above 100 cd/m^2 **(b)** The comparison of relative lifetime of an unencapsulated device vs a wax encapsulated device.

as the device's lifetime.

The J-L curves of a wax encapsulated OLED, lifetime tested in the way described is shown in Figure 6.4 (a). The luminance initially goes above 100 cd/m^2 and the system attempts to reduce the voltage, hitting the upper limit several times as despite reducing voltage, the luminance continues to rise. This is consistent with other devices, taking some time to become stable after turning on. The luminance then begins to fall and starts hitting the lower limit before voltage is increased. As this is happening with the luminance the EQE undergoes a large drop from its initial value. All metrics now become very stable after 30 minutes. The device EQE steadily declines throughout the life of the device, as would be expected. Before the device fails to remain lit evidence of failure is seen in the rapidly increasing current density and tumbling efficiency. Eventually the device fails to remain within the 95 - 105 cd/m^2 window, and despite rising voltage fails quickly. The device shown here is typical of the devices tested for lifetime.

When the lifetime of wax encapsulated OLEDs is compared with an unencapsulated device from the same batch a very large difference in lifetime is observed. Figure 6.4 (b) shows the comparison of the best performing devices of each type. The lifetime values are with respect to the lifetime of the unencapsulated device, which has a lifetime of 1. The wax encapsulated OLED showed a lifetime $\approx$ 13 times higher.

For laboratory encapsulation this method is low-cost and simple and can be adapted

to many other types of devices, such as PVs or photodetectors. It also could be used on a large scale, being solution processable could allow it to be used in conjunction with roll-to-roll manufacturing techniques with relative ease.

For use in this work this method of encapsulation ensures device stability for long enough to fully characterise the EL spectrum, and emission angle without luminance degradation. Between hours 1 and 2 the EQE fell by just 0.8 points, or 6%. All measurements that require stability can be easily taken in this time, and a 6% change in EQE is not going to significantly change any of the measurements.

6.6 SUMMARY AND OUTLOOK

Encapsulation is a very important element of OLED device fabrication.[4] In laboratory settings stability is critical to accurately characterising device performance. When flexible devices are considered the usual small-scale method of gluing a glass coverslip with UV cured epoxy is not suitable. It has been shown in the past to work very successfully in rigid devices,[4] and when implemented in the devices investigated in this thesis increased the lifetime of them by a factor of almost 3. The fact so much of the device remained exposed to the ambient environment likely meant the benefit wasn't greater. There is also the fundamental problem of heat dissipation using this method. The fact the system is not flexible meant it could not be used in flexible devices.

I investigated a novel encapsulation method using standard office lamination sheets and a laminator. The sheets were laser cut with an appropriate pattern and applied in the standard way. The results of this showed that the overall half-life of the devices was reduced. This was likely due to weak adhesive, not adequately adhering to the OLED surface. The difficulty of choosing lamination sheets based on their adhesives meant this study could not continue further. With more commercial knowledge into the materials used in these sheets, this is an area that could be investigated further to give a cheap, easy, and scalable encapsulation method for flexible devices.

Finally, I investigated another novel encapsulation method. This time using beeswax as the encapsulation film. The results of this study showed very promising results. The encapsulated devices remained at a useful luminance for almost 13 times longer than the unencapsulated devices. The degradation was slow enough that many measurements could be carried out to characterise the devices. Critically I have shown that

this method of encapsulation is significantly better than the standard laboratory technique of epoxy encapsulation. Although cover encapsulation techniques that involve caps, getters, or air gaps were not compared. This technique is also potentially scalable and compatible with current industry roll-to-roll techniques. This method offers the most promise going forward.

This area of research is very active, there is still a significant search on for a novel material that meets the requirements of low-cost and high throughput. It is still well recognised that for OLEDs, PVs, and perovskite solar cells there is an urgent demand for a flexible, cost-effective encapsulation material. I have demonstrated beeswax as being a potential starting point for investigating new, wax-based encapsulation materials.

BIBLIOGRAPHY

[1] Seunghwan Lee, Ju Hwan Han, Seong Hyeon Lee, Geon Ho Baek, and Jin Seong Park. Review of Organic/Inorganic Thin Film Encapsulation by Atomic Layer Deposition for a Flexible OLED Display. *JOM*, 71(1):197–211, 1 2019.

[2] Tzu En Huang, Hou Jen Chen, Ching Hsiu Chen, Yu Hung Lin, Sun Zen Chen, Shih Wen Wen, and Jwo Huei Jou. Organic lighting devices are plausibly more vulnerable to oxygen than moisture. *Organic Electronics*, 99:106333, 12 2021.

[3] Fabrication and Characterization of Organic Light Emitting Diode (OLED).

[4] Qian Lu, Zhichun Yang, Xin Meng, Youfeng Yue, Muhammad Ashfaq Ahmad, Wenjun Zhang, Shasha Zhang, Yiqiang Zhang, Zonghao Liu, and Wei Chen. A Review on Encapsulation Technology from Organic Light Emitting Diodes to Organic and Perovskite Solar Cells. *Advanced Functional Materials*, 31(23):2100151, 6 2021.

[5] John E. Knox, Mathew D. Halls, Hrant P. Hratchian, and H. Bernhard Schlegel. Chemical failure modes of AlQ3-based OLEDs: AlQ3 hydrolysis. *Physical Chemistry Chemical Physics*, 8(12):1371–1377, 3 2006.

[6] Masamichi Yamada, Isao Ikemoto, and Haruo Kuroda. Photooxidation of the Evaporated Films of Polycyclic Aromatic Hydrocarbons Studied by X-Ray Photoelectron Spectroscopy. *Bulletin of the Chemical Society of Japan*, 61(4):1057–1062, 6 1988.

[7] Hany Aziz, Zoran Popovic, Shuang Xie, Ah Mee Hor, Nan Xing Hu, Carl Tripp, and Gu Xu. Humidity-induced crystallization of tris (8-hydroxyquinoline) aluminum layers in organic light-emitting devices. *Applied Physics Letters*, 72(7):756–758, 6 1998.

[8] Takao Noguchi, Bappaditya Roy, Daisuke Yoshihara, Junji Sakamoto, Tatsuhiro Yamamoto, and Seiji Shinkai. A Chiral Recognition System Orchestrated by Self-Assembly: Molecular Chirality, Self-Assembly Morphology, and Fluorescence Response. *Angewandte Chemie*, 129(41):12692–12696, 10 2017.

[9] Min Geun Song, Kwan Soo Kim, Hye In Yang, Seong Keun Kim, Jae Hyun Kim, Chang Wook Han, Hyun Chul Choi, Ramchandra Pode, and Jang Hyuk Kwon. Highly reliable and transparent Al doped Ag cathode fabricated using thermal evaporation for transparent OLED applications. *Organic Electronics*, 76:105418, 1 2020.

[10] Jianbin Wang, Zhanhao Hu, Zhiming Zhong, Lei Wang, Jianhua Zou, Yueju Su, Dongyu Gao, Hua Zheng, Jian Wang, Junbiao Peng, and Yong Cao. Stressing organic light-emitting diode under constant-brightness driving mode. *Organic Electronics*, 21:192–197, 6 2015.

[11] Jakaria Ahmad, Kateryna Bazaka, Liam J. Anderson, Ronald D. White, and Mohan V. Jacob. Materials and methods for encapsulation of OPV: A review. *Renewable and Sustainable Energy Reviews*, 27:104–117, 11 2013.

[12] Hongkyu Kang, Geunjin Kim, Junghwan Kim, Sooncheol Kwon, Heejoo Kim, and Kwanghee Lee. Bulk-Heterojunction Organic Solar Cells: Five Core Technologies for Their Commercialization. *Advanced Materials*, 28(36):7821–7861, 9 2016.

[13] Jens A. Hauch, Pavel Schilinsky, Stelios A. Choulis, Sambatra Rajoelson, and Christoph J. Brabec. The impact of water vapor transmission rate on the lifetime of flexible polymer solar cells. *Applied Physics Letters*, 93(10):103306, 9 2008.

[14] A. Ra Cho, Eun Hye Kim, Soo Young Park, and Lee Soon Park. Flexible OLED encapsulated with gas barrier film and adhesive gasket. *Synthetic Metals*, 193:77–80, 7 2014.

[15] Kenta Nishijima, Tatsuki Hasegawa, and Mikihiro Kashio. Gas-barrier adhesive sheet as a face-sealing encapsulation for flexible OLEDs. In *Digest of Technical Papers - SID International Symposium*, volume 48, pages 441–444. John Wiley & Sons, Ltd, 5 2017.

[16] Jongwoon Park, Hyokyun Ham, and Cheolyoung Park. Heat transfer property of thin-film encapsulation for OLEDs. *Organic Electronics*, 12(2):227–233, 2 2011.

7

ALTERNATIVE PROPERTIES WHICH AFFECT DEVICE PERFORMANCE

7.1 INTRODUCTION

Surface roughness of substrates for use in organic light-emitting diode (OLED) and photovoltaic (PV) manufacture is known to be a major barrier to efficient and uniform devices.[1;2] Large surface roughness is known to cause pinhole defects, which cause high leakage current, electrical shorts, and reduced device lifetime due to ingress of oxygen, moisture, and other contaminants.[2] High surface roughness is also known to cause charge scattering, charge trapping, charge imbalance in devices, and an increase in exciton quenching.[3;4] The electrical effects appear as dark spots on the device. Reducing surface roughness is often seen as one of three key elements of integrating graphene-based materials such as $FeCl_3$ intercalated FLG ($FeCl_3$-FLG) into OLEDs, the other two are reducing sheet resistance, and tuning work function.[4] Already $FeCl_3$-FLG achieves the latter two, with a 10-fold reduction in sheet resistance, and a reduction in work function from -4.4 eV to -5.0 - -5.5 eV.

The importance of surface roughness in transparent conductive electrodes (TCEs) means I wanted to investigate and report the surface roughness of $FeCl_3$-FLG along with other common materials and precursors used in this work. I also wanted to investigate possible mitigation strategies that could be introduced to reduce surface roughness before OLEDs are made on top. Here I evaluated the surface roughness of various electrode candidates and substrates, I then evaluated mitigation strategies, before integrating these materials into OLED devices.

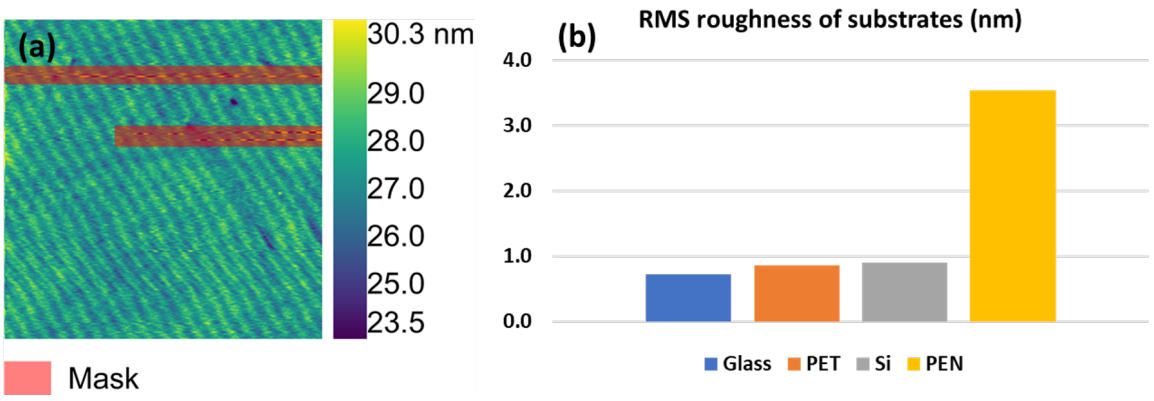

Figure 7.1: **(a)** AFM map of glass used as OLED substrate. The masked area is not included in the roughness calculation. **(b)** Bar chart showing the RMS roughness of OLED substrates used in this work.

7.2 ROUGHNESS OF VARIOUS ELECTRODES/SUBSTRATES

The most fundamental part of the OLED device is the substrate. If the roughness of the substrate is not controlled, any material deposited on top will take its form. It is also important to look at substrates to get an idea of the resolution of the measurement equipment.

A NanoSurf Naio atomic force microscopy (AFM) is used to measure the surface roughness of all substrates and materials. The AFM in contact mode is used to create 5×5 μm roughness map. The data is then processed using the free, open source, Gwyddion software package. Using Gwyddion, the data is levelled by mean plane subtraction, align rows using various methods, correct horizontal scars, shift the minimum data value to zero, and mask off remaining scarred regions, before measuring the statistical quantities of the map. The primary quantity evaluated is the root mean squared (RMS) surface roughness Sq, defined as:

$$Sq = \sqrt{\frac{1}{A}\int\int_A (Z(x,y))^2 dxdy} \tag{7.1}$$

where A is the area being measured, Z is the height, and x and y are the location coordinates. The resultant map, with masked region where there is a horizontal scar,

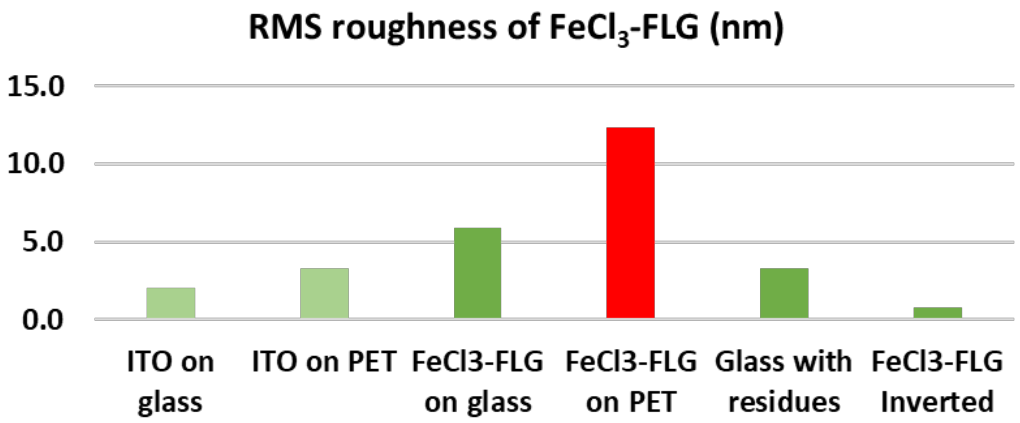

Figure 7.2: Bar chart of the RMS roughness of $FeCl_3$-FLG and ITO, on glass and PET substrates. PMMA residues from thermal transfer and inverted $FeCl_3$-FLG is also compared.

can be seen in Figure 7.1 (a). In Figure 7.1 (a) a repeating pattern can be clearly seen. This pattern is not a defect or material parameter, rather the resolution of the AFM, the pattern is likely caused by the AFM tip and the internal fan. The pattern can be extracted when a 1D fast Fourier transform filter is applied. The pattern has a horizontal resonance of 0.026 nm^{-1} after clockwise rotation by 31°. The pattern is particularly prevalent in samples with RMS values < 1 nm. For this reason, 1 nm is set as the minimum roughness resolution. I will not routinely subtract the resonance, as the high roughness of other materials seen later makes it irrelevant.

Figure 7.1 (b) shows four substrates used for OLEDs in this work. The roughness is obtained in the same way as described before for all of them. Here the lowest value roughness is reported for each of the four materials tested. The glass, polyethylene terephthalate (PET), and silicon substrates all show RMS roughness < 1 nm, I can conclude that these are all very smooth, sufficient for OLED fabrication. The poly(ethylene 2,6-naphthalate) (PEN) substrate shows a much higher RMS roughness, however studies suggest roughness below 10 nm may be sufficient for working devices.

Next, the electrodes are examined. To do this the electrode and substrate will be taken together. As the device layers will be spin-coated onto the electrode-substrate in liquid form, this is a relevant study. The results of this can be seen in Figure 7.2.

The roughness of both indium tin oxide (ITO) substrates is low, at approximately 2.0 and 3.5 nm. The roughness of ITO on PET is comfortably under the suggested 10

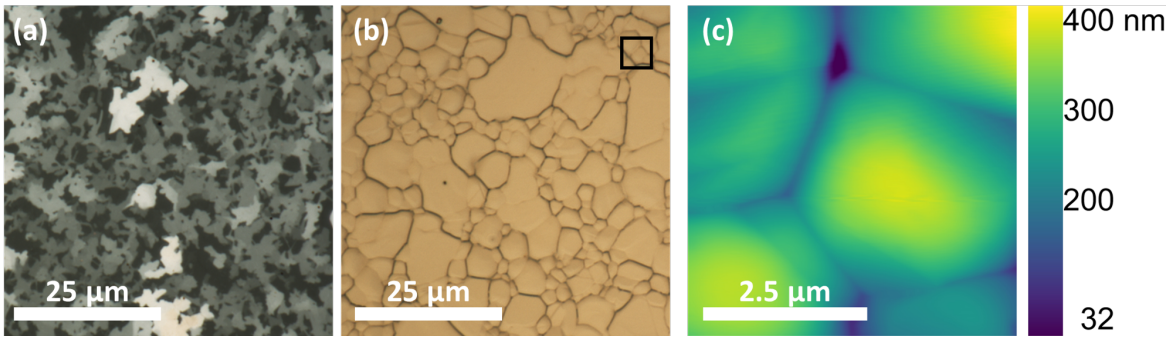

Figure 7.3: **(a)** Optical image of $FeCl_3$-FLG. **(b)** Optical image of the Ni/Si/SiO_2 substrate on which FLG grows. **(c)** AFM of same. The small square inset in (b) is the equivalent size of the AFM map in (c).

nm cut-off, and as I will show later has no problems in working devices. The $FeCl_3$-FLG based substrates are considerably rougher, with $FeCl_3$-FLG on PET breaking the 10 *nm* cut-off. This will be seen to be important and relevant later. These results show the effects of the transfer process and adding materials with high roughness. Here the effect of adding $FeCl_3$-FLG to PET is seen to be greater than the sum of its parts. Residues that remain from the thermal transfer process are the likely source of this. Thermal transfer tape uses a thermal adhesive which likely leaves significant residues, even after acetone cleaning, the same is known for poly(methyl 2-methylpropenoate) (PMMA) which is used as a support layer. Due to being on a plastic substrate it is not possible to thermally anneal these samples.

The roughness of the $FeCl_3$-FLG substrates is clearly very high. This is fundamentally due to the domain structure of Ni grown few-layer graphene (FLG). The domains in Figure 7.3 (a) can clearly be seen, and it can be clearly seen how the graphene takes this form. Figure 7.3 (b) & (c) show the Ni substrate on which FLG is grown. The nickel on the SiO_2/Si substrate appears in its own domains, up to 400 *nm* tall. The FLG then takes this form during chemical vapour deposition (CVD) resulting in a patchy and rough material. This is the one major drawback to using Ni grown FLG for $FeCl_3$-FLG, however no other graphene grown by other, smoother forms of CVD, such as copper grown, have proven successful at making $FeCl_3$-FLG.

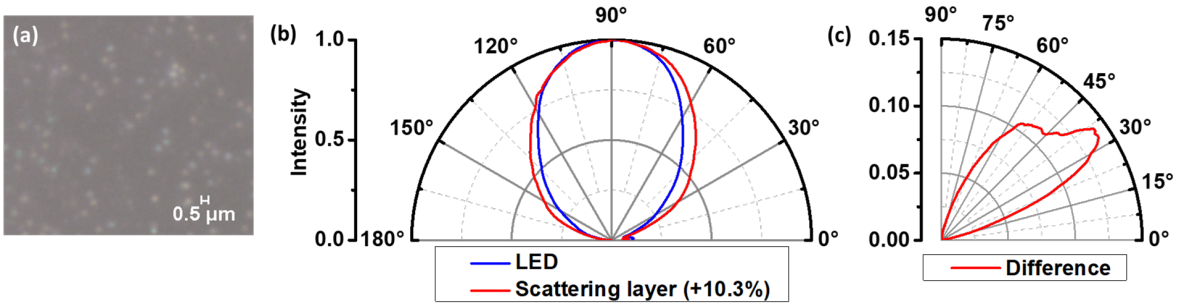

Figure 7.4: **(a)** Microscope image of SiO_2 nanospheres cured in optical adhesive glue. **(b)** Emission angle profile of the scattering film compared to the control emission from the LED. The area under the curve for the scattering layer is 10% greater. **(c)** The intensity of the scattering layer minus the intensity of the control LED.

7.3 OUT COUPLING AND SUBSTRATE SCATTERING

One of the main sources of loss in an OLED device is through light lost within the device. 40% of light can become trapped in the device due to waveguide modes.[5] These modes form because of total internal reflection within the device, at every material boundary. One effective way of reducing the amount of light lost because of this effect, and to increase the viewing angle of a device is to employ a scattering layer.[6] This can also serve as a useful test of my custom-built goniometer.

A simple and cost-effective way of using a scattering layer is to coat the emission side of the OLED device with a scattering film.[6] For this test of the goniometer, I choose a film that has been investigated before, and shown its ability as a scattering film. This film is composed of 507 nm diameter SiO_2 nanospheres encased in a ultraviolet (UV)-cured optical adhesive, NOA73 (Norland Products).

The scattering layer is made by mixing SiO_2 nanospheres 3% by wt. in NOA73. This mixture is sonicated in a sonic bath for 5 hours, before being filtered into a clean amber vial using 5 μm syringe filters.

To coat the substrate the mixture is dropped onto a static sample, before the sample is spun at 500 RPM for 60 seconds. The sample is then cured under UV for 5 minutes.

To investigate the effect that such a scattering layer might have at improving the viewing angle of the OLEDs referred to in this work I compared the emission angle profiles of scattering layers with a bare substrate. The control sample was a bare 12 ×

12 mm glass substrate, the same as devices are built on, back illuminated by a standard light-emitting diode (LED). The scattering sample was the same 12 $\times$ 12 mm glass substrate with the scattering layer deposited as described above.

Figure 7.4 (a) shows the distribution of scatters in the adhesive. Each scatterer is spaced out from one another this ensures high transmittance and keeps haze reduced. This figure also shows the nanospheres do not aggregate to form clumps this is likely due to successful sonication followed by filtering out any particles larger than 5 μm.

Figure 7.4 (b) shows the effect the scattering layer has on the emission angle profile of a commercial LED. Here it is observed that the area under the curve of the scattering film emission angle profile is 10.3% greater than that of the control device. This results in an increase in viewing angle with a higher proportion of emission between 29° and 57°. The angle where viewing angle is most improved is seen in Figure 7.4 (c), this graph shows the difference between the normalised control and normalised scattering layer. A large increase in intensity, $>$ 10%, centred around 45° can be seen.

These data show the potential benefits of using a scattering layer to increase viewing angle. Ultimately however the reduction in transmittance means such a scattering film in its current form would not be of benefit to increasing the efficiency of the devices used in this work.

7.4 NOVEL SUBSTRATES AND METHODS TO REDUCE ROUGHNESS

Due to poor performance of $FeCl_3$-FLG based OLED devices due to high surface roughness it is necessary to investigate new methods of preparing $FeCl_3$-FLG for devices. As can be seen in Figure 7.2 the roughness of $FeCl_3$-FLG on PET is very high. A simple way of reducing the roughness of $FeCl_3$-FLG on flexible substrates may be to simply invert it.

When FLG is grown on nickel via CVD the structure that forms is believed to be 1 or 2 continuous layers of graphene with 3 - 7-layer domains forming on top. These domains are believed to contribute significantly to the roughness of nickel-grown FLG. If the material can be easily inverted, it may be possible to access this smoother side of the material. It is also worth considering the use of PMMA in the transfer of FLG from nickel to glass. PMMA is used as a support layer on the top side of the material, and this needs to be washed off. It needs to be used again when undergoing

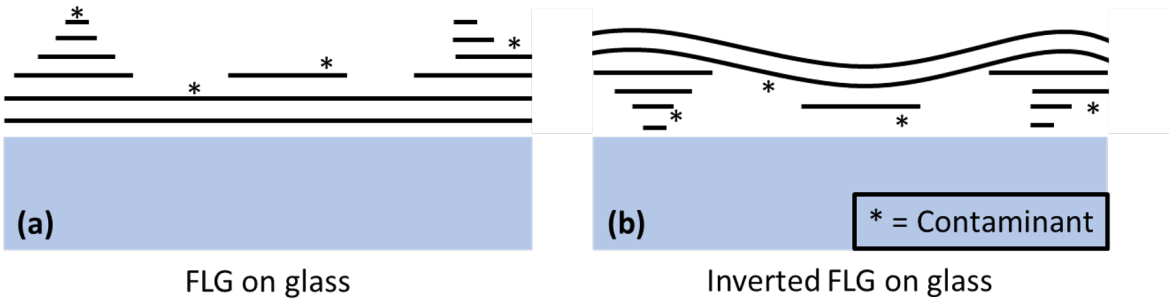

Figure 7.5: **(a)** The domain structure of FLG. Multi-layer islands of graphene sit on a continuous bi-layer sheet. Any contaminants, such as PMMA residue, sit on top. **(b)** When FLG is inverted the smooth bilayer is exposed on top, contaminants are covered on the bottom side, leaving a smoother surface.

the thermal transfer procedure for the same reason. It again needs to be washed off. At no stage however is PMMA or any other polymer used on the bottom side. The bottom side is etched from the nickel chemically, then rinsed in deionised (DI) water before being transferred to cleaned glass. This means there may be a double effect of low roughness on this bottom side due to lack of exposure to any polymers, and the continuous structure present.

The effect of the mentioned residues was investigated. The thermal transfer process was conducted on glass. A PMMA support layer was deposited on glass, and then removed using the thermal transfer method. It was transferred onto a new clean glass substrate. This sample was then washed in acetone in the same way as transferred $FeCl_3$-FLG is. The roughness of this sample can be seen in Figure 7.2. The surface roughness of cleaned glass is $< 1\ nm$, while the residues increase the roughness to 3.3 nm.

Most importantly the inverted structure was investigated. This method relies on using the thermal transfer tape to peel the $FeCl_3$-FLG off the glass substrate but does not involve any other destination substrate. The inverted $FeCl_3$-FLG now sits on its PMMA support layer, thermal adhesive, and PET thermal tape. The top side is now the bilayer. Figure 7.2 shows the roughness of this structure is very low, $< 1\ nm$ RMS. This material, deposited in this way clearly solves the roughness issues associated with $FeCl_3$-FLG.

7.5 SUMMARY AND OUTLOOK

This new way of inverting $FeCl_3$-FLG shows great promise at significantly reducing surface roughness of the material on flexible substrates where there is greatest need. There are however several significant drawbacks that need to be overcome if this method can be used for electrodes in devices.

This study used thermal transfer tape to invert the $FeCl_3$-FLG. This was used as it is known to be very effective at removing $FeCl_3$-FLG from glass. The problems introduced by using thermal transfer tape are primarily its low temperature resistance and chemical resistance. As the name suggests thermal tape undergoes a change in properties at a certain temperature. At approximately 90°C this tape loses its adhesion properties. This causes the inverted $FeCl_3$-FLG to bubble up and partially detach from the substrate. While poly(9,9-dioctylfluorene-alt-benzo-thiadiazole) (F8BT) can be processed below 90°C, most other common OLED materials need to be processed at much higher temperatures, aluminium doped zinc oxide (AZO) for example requires a 200°C anneal.[7] This is likely to be an issue with most adhesives, however it does not mean this method cannot be pursued further. Almost all commercial OLEDs are not solution processed and so do not need high temperature annealing. Most commonly materials are evaporated and do not need high temperature processes, this would allow thermal tape to be used successfully. The chemical resistance problem can also potentially be solved by evaporated devices. The tape used in this study is not resistant to common laboratory solvents such as acetone. Chemicals used in the solution coating of other OLED layers cause the adhesion of thermal tape to fail, and the $FeCl_3$-FLG lifts off in the same way as for heat. With an evaporated device, this could be an effective way of reducing the surface roughness of $FeCl_3$-FLG.

Going forward further investigation is needed into inverted $FeCl_3$-FLG to significantly reduce its surface roughness. The method presented preserves transmittance, ensures smoothness, and may offer better electrical contact with adjacent layers. This method is not compatible with solution processed devices, however. This means it cannot be tested in devices using the methods presented in this work. There is no reason however as to why it cannot work in evaporated devices, the standard deposition method in industry settings.[8] It is important that this work is carried out quickly as overcoming surface roughness limitations is of key importance to integrating $FeCl_3$-FLG

into commercial OLEDs and PVs.

BIBLIOGRAPHY

[1] Thomas J. Routledge, David G. Lidzey, and Alastair R. Buckley. Ultrasonic spray coating as an approach for large-area polymer OLEDs: The influence of thin film processing and surface roughness on electrical performance. *AIP Advances*, 9(1):015330, 1 2019.

[2] Ki Beom Kim, Yoon Heung Tak, Yoon Soo Han, Kwang Heum Baik, Myung Hee Yoon, and Moon Ho Lee. Relationship between surface roughness of indium tin oxide and leakage current of organic light-emitting diode. *Japanese Journal of Applied Physics, Part 2: Letters*, 42(4 B):L438, 4 2003.

[3] Tae Hee Han, Youngbin Lee, Mi Ri Choi, Seong Hoon Woo, Sang Hoon Bae, Byung Hee Hong, Jong Hyun Ahn, and Tae Woo Lee. Extremely efficient flexible organic light-emitting diodes with modified graphene anode. *Nature Photonics*, 6(2):105–110, 2 2012.

[4] Zhikun Zhang, Lianlian Xia, Lizhao Liu, Yuwen Chen, Zuozhi Wang, Wei Wang, Dongge Ma, and Zhaoping Liu. Ultra-smooth and robust graphene-based hybrid anode for high-performance flexible organic light-emitting diodes. *Journal of Materials Chemistry C*, 9(6):2106–2114, 2 2021.

[5] Alongkarn Chutinan, Kuniaki Ishihara, Takashi Asano, Masayuki Fujita, and Susumu Noda. Theoretical analysis on light-extraction efficiency of organic light-emitting diodes using FDTD and mode-expansion methods. *Organic Electronics*, 6(1):3–9, 2 2005.

[6] Jinouk Song, Kwon Hyeon Kim, Eunhye Kim, Chang Ki Moon, Yun Hi Kim, Jang Joo Kim, and Seunghyup Yoo. Lensfree OLEDs with over 50% external quantum efficiency via external scattering and horizontally oriented emitters. *Nature Communications*, 9(1):1–10, 12 2018.

[7] Jewel Kumer Saha, Ravindra Naik Bukke, Narendra Naik Mude, and Jin Jang. Significant improvement of spray pyrolyzed ZnO thin film by precursor optimization for high mobility thin film transistors. *Scientific Reports*, 10(1):1–11, 6 2020.

[8] Fabrication and Characterization of Organic Light Emitting Diode (OLED).

8

HYBRID FECL$_3$-FLG:ITO TRANSPARENT CONDUCTIVE ELECTRODE

8.1 INTRODUCTION

Organic light-emitting diode (OLED) devices fabricated on indium tin oxide (ITO) worked remarkably well throughout this work. ITO is the industry leading transparent conductive electrode (TCE) material, its fabrication has been perfected over many years, as a result the current material is incredibly well suited to many applications.[1] I have discussed and investigated extensively using $FeCl_3$ intercalated FLG ($FeCl_3$-FLG) as an ITO replacement. The results from this investigation have been meagre. To attempt to address this and to improve and increase the suite of materials available attempting to incorporate the good properties of both ITO and $FeCl_3$-FLG is desirable.

To do this I have fabricated a hybrid material, known as $FeCl_3$-FLG enhanced ITO ($FeCl_3$-FLG:ITO). This material is composed of $FeCl_3$-FLG on ITO on a flexible polyethylene terephthalate (PET) substrate.

8.2 FABRICATION

$FeCl_3$-FLG:ITO was fabricated by taking $FeCl_3$-FLG, fabricated in the way described in Section 3.2.2 on glass and thermally transferring it to ITO coated PET using the thermal transfer technique discussed in Section 3.2.1.3. Once transferred the material is cleaned in acetone to remove any poly(methyl 2-methylpropenoate) (PMMA) residues from the transfer and it is then washed in propan-2-ol (IPA), before being blow dried with nitrogen.

8.3 MATERIAL CHARACTERISATION

The characterisation will assume that this material combination is a single, new hybrid material. I will investigate its properties as any other single material. There are several main areas that I want to investigate this new material. The areas investigated will be limited to those relevant for its use as a TCE in OLEDs. These are sheet resistance, optical transmittance, Raman spectroscopy, and bending performance.

8.3.1 *Sheet resistance*

Sheet resistance is one of the most important properties for assessing materials suitable for use as TCE. The expected sheet resistance of this hybrid material can be predicted by assuming the two materials will act as resistors in parallel. It is known that the sheet resistance of ITO on PET is approximately 60 Ω/□, and the sheet resistance of $FeCl_3$-FLG is approximately 100 Ω/□, therefore it is expected that the sheet resistance of the hybrid material will be approximately 37.5 Ω/□.

$$\frac{1}{R_{\parallel}} = \frac{1}{R_1} + \frac{1}{R_2} \tag{8.1}$$

$R_{\parallel}$ is the total resistance of resistors in parallel, and R_n is the resistance of one of the resistors.

When the sheet resistance of $FeCl_3$-FLG:ITO is measured values very close to expected are seen. With only a small number of samples tested a sheet resistance of 39.5 ± 3.8 Ω/□ was measured. This matches well with what is expected for two resistors in parallel and is also a good value for an effective TCE in its own right. It is a value that is significantly lower than both ITO and $FeCl_3$-FLG, this is essential for an ITO replacement material.

The measurements taken here were taken as described in Section 2.5. These measurements can damage graphene-based materials due to the four-point probe making physical contact with the material. It is for this reason that few measurements were carried out. As the standard deviation was less than 10% it was decided that this was appropriate. More measurements should be carried out in future to get a more accurate number for sheet resistance of $FeCl_3$-FLG:ITO.

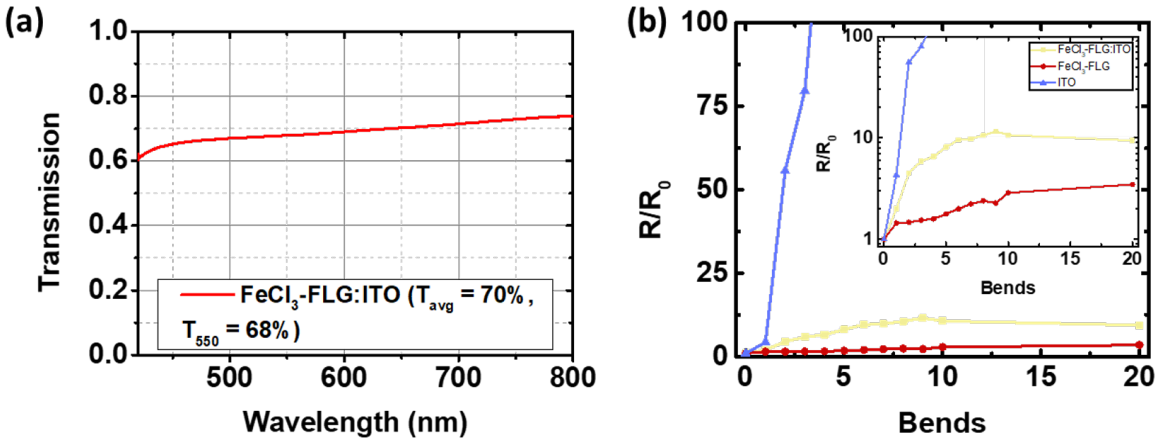

Figure 8.1: **(a)** Optical transmittance of $FeCl_3$-FLG:ITO in the visible range. **(b)** Bending performance of $FeCl_3$-FLG:ITO vs $FeCl_3$-FLG vs ITO, with the same graph in log scale **inset**. R_0 is the same value for all materials, allowing for all three to be compared against each other.

8.3.2 *Optical transmittance*

The next most important property that must be investigated for TCE materials is optical transmittance. Here no benefit of putting these two materials together is expected. It is anticipated that the transmittance of the hybrid material will be reduced compared to the materials individually. The expected transmittance, $T_{expected}$, will be as follows:

$$T_{expected} = T_1 \cdot T_2 \tag{8.2}$$

where T_n is the optical transmittance of one of the materials.

Knowing that the transmittance of ITO at 550 nm is 91%, and the same for $FeCl_3$-FLG is 71% indicates that the transmittance of $FeCl_3$-FLG:ITO is expected to be 65%. The optical transmittance of this hybrid material can be seen in Figure 8.1 (a). The transmittance is approximately flat across the visible range, as expected as both constituent materials have a flat profile. The transmittance at 550 nm is 68%, and the transmittance on average is 70%. These values fit well with what I have just predicted. The transmittance on average was expected to be 70%.

8.3.3 *Bending*

The primary reason for combining ITO and $FeCl_3$-FLG is to incorporate their properties. OLEDs made on ITO worked well for us, but ITO is not flexible, OLEDs made on $FeCl_3$-FLG failed to work, but $FeCl_3$-FLG is flexible. Combining these two into a hybrid material could allow the TCE to continue conducting well, even with slight damage occurring to the ITO underneath.

To assess the bending performance, the roller bender described in Section 4.5.0.2 was used. The samples are all bent around a cylindrical pin with a radius of 3 mm. The samples used are all 12×12 mm in size, the same as the OLEDs discussed in this work.

When looking at the relative increase in resistance, in Figure 8.1 (b), and compare the three TCEs after bending it can be seen how the resistance of ITO rises very quickly. After just 4 bends the resistance of ITO has increased over 100 times, meanwhile the resistance of $FeCl_3$-FLG and $FeCl_3$-FLG:ITO increased by 1.6 and 6.5 times respectively.

The change in resistance of ITO and $FeCl_3$-FLG has been discussed before in Section 5.4, and the results seen here mirror those in that section. Here it is seen that in terms of bending performance $FeCl_3$-FLG:ITO degrades in a way which is much more like $FeCl_3$-FLG than ITO. The layer of $FeCl_3$-FLG manages to successfully mitigate the cracking ITO and allows it to retain its low resistance. To see how the overall performance as a TCE might be affected, and whether $FeCl_3$-FLG:ITO is closer overall to $FeCl_3$-FLG or ITO the figure of merit for TCEs must be examined.

8.3.4 *Figure of merit*

Figure of merit (FoM) introduced in Section 2.3, is a figure which relates the electrical and optical properties of a TCE for the purposes of accessing material suitability with a single figure.[2] The overall suitability of $FeCl_3$-FLG:ITO can be assessed with this figure and by comparing it directly to ITO and $FeCl_3$-FLG. I can also look at how the figure of merit changes after the material is repeatedly bent. The figure of merit, FoM, is defined as:

$$FoM = \frac{Z_0}{2R_S(T^{-0.5} - 1)} \tag{8.3}$$

Table 8.1: Figure of merit of the various TCEs.

TCE material	R_S ($\Omega/\square$)	T_{550} (%)	FoM
ITO (on PET)	60	91	65
$FeCl_3$-FLG	100	71	10
$FeCl_3$-FLG:ITO	40	70	22

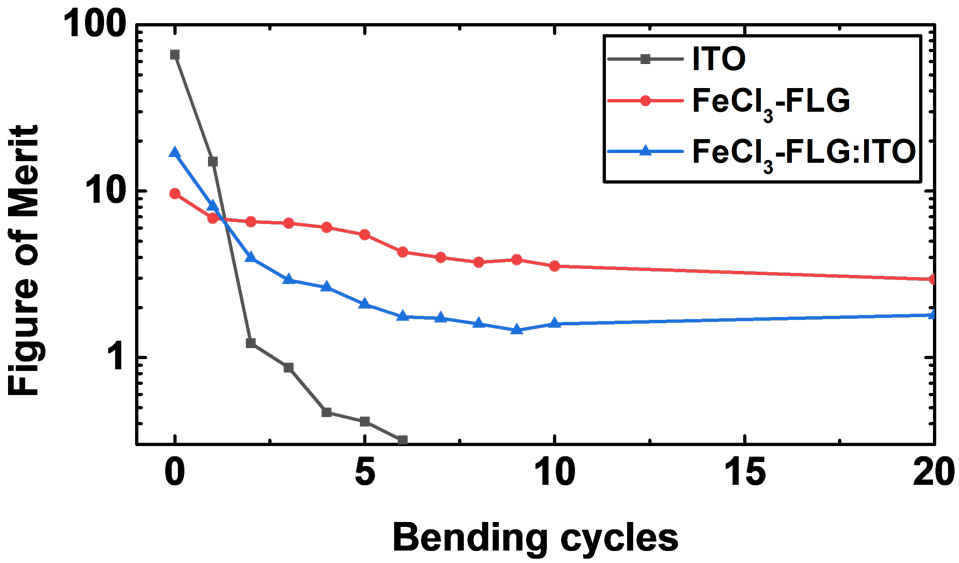

Figure 8.2: Graph showing how the figure of merit (FoM) changes with bending cycles. As the ITO cracks sheet resistance rises and FoM falls dramatically.

where Z_0 is the impedance of free space (377 Ω).

Table 8.1 shows the calculated FoM values for the three materials being studied. It shows that despite the sheet resistance of $FeCl_3$-FLG:ITO now being less than that of ITO, the FoM is not. It is also noted that the FoM of $FeCl_3$-FLG:ITO is more than double that of $FeCl_3$-FLG, this is due almost entirely to the significant reduction in sheet resistance, without much compromise in optical transmittance. This suggests that ITO would be a better TCE than $FeCl_3$-FLG:ITO, if $FeCl_3$-FLG:ITO offered no new properties. I showed in the previous section however that $FeCl_3$-FLG:ITO does offer a significant new property in flexibility.

Looking at how the FoM changes as the device is bent, the superior properties of both $FeCl_3$-FLG:ITO and $FeCl_3$-FLG over ITO are clear. Figure 8.2 shows how the

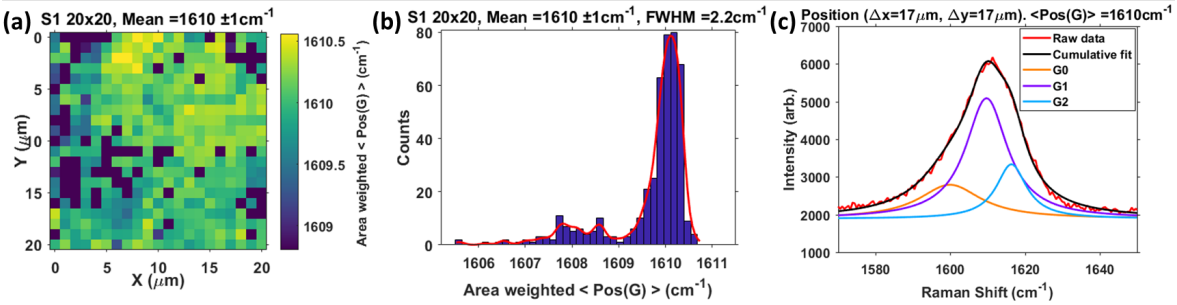

Figure 8.3: **(a)** Raman map showing the area weighted $< PosG >$ for $FeCl_3$-FLG:ITO. **(b)** Histogram summarising the data in (a). **(c)** Raman spectrum showing how a typical point on the map is a convolution of three peaks, indicating the shift in G peak is due to intercalation rather than strain.

high FoM of ITO quickly drops far below that of $FeCl_3$-FLG:ITO and $FeCl_3$-FLG. The large drop in TCE performance is seen in the first 5 bends of the material, with the FoM of ITO dropping by nearly three orders of magnitude in this time. At the same time $FeCl_3$-FLG and $FeCl_3$-FLG:ITO stay relatively stable. This is the clearest indicator of the benefits of $FeCl_3$-FLG and $FeCl_3$-FLG:ITO over ITO as a flexible TCE.

By covering ITO in a layer of $FeCl_3$-FLG it is clear that I can combine the conductivities of the two materials and enhance the bending performance. This leaves a material which combines the best overall properties of ITO and $FeCl_3$-FLG, and it gives substantially superior electrical properties after just 6 bending cycles. Even if this material is not utilised for a flexible application, it offers significantly better robustness for manufacturing processes such as roll-to-roll, which could damage ITO during OLED fabrication.

8.3.5 *Raman spectroscopy*

With $FeCl_3$-FLG deposited onto a new substrate it is important to assess if the vibrational modes have changed. Raman is one of the primary characterisation tools when using $FeCl_3$-FLG and it is important to know if these modes have been affected by the new substrate. The G peak is the most important to know about as it indicates intercalation. It can however be affected by strain,[3;4] which may have occurred during the transfer process.

When Raman spectroscopy is examined, it is clear that the $FeCl_3$-FLG:ITO has not been affected by strain. Raman maps were taken of the material which show a constant material with little variation. Figure 8.3 (a) shows the Raman map. Here the area weighted $< PosG >$ position is plotted. The values have a mean of 1610 pm 1 cm^{-1}. The distribution of this is seen in histogram form in Figure 8.3 (b). Here it can be seen that most values cluster tightly around 1610 cm^{-1}. 1610 cm^{-1} is a figure that most likely indicates good stage 1, G_1 doping, with some partial G_2. In Figure 8.3 (c) a typical spectrum has been selected. This spectrum can be accurately reconstructed through the convolution of 3 Lorentzian peaks. These are the 3 stages of intercalation. It is clear from this that stage 1 doping dominates, with partial stage 2. The fact that the spectrum is a convolution of multiple peaks is a clear indication that the doping has not been affected and is the reason for the G peak shift. I anticipated that the $FeCl_3$-FLG on $FeCl_3$-FLG:ITO will perform the same as it usually does on various other substrates. This is seen to be true when sheet resistance and optical transmittance are looked at.

8.4 OLED INTEGRATION

A significant motivation for investigating $FeCl_3$-FLG:ITO is the absence of any working $FeCl_3$-FLG on PET OLED devices. By incorporating the two materials into a single hybrid electrode it may be possible to minimise the brittle nature of ITO, while getting working devices.

The $FeCl_3$-FLG:ITO electrode was fabricated as described above and incorporated into a conventional OLED. These OLEDs were tested unencapsulated, the same way as all previous $FeCl_3$-FLG were tested. The devices were characterised using the calibrated luminance meter based setup. Each pixel was tested individually, they were tested by biasing them in 1-volt increments, each voltage was held for 7.46 seconds while the luminance meter acquired. Each pixel was tested to beyond the point of peak luminance. Pixels were tested to destruction.

The $FeCl_3$-FLG:ITO devices were tested in comparison to devices with ITO TCE from the same batch. This ensures the results are directly comparable, accounting for any storage related material degradation. The only difference in these devices is the TCE.

Table 8.2: Summary of ITO vs $FeCl_3$-FLG:ITO OLEDs. $V_{L_{peak}}$ refers to the voltage at which the peak luminance occurs.

TCE	L (cd/m^2)	CE (cd/A)	PE (lm/W)	V_T (V)	$V_{L_{peak}}$ (V)	EQE (%)
ITO (best)	434	0.62	0.077	15	27	0.19
$FeCl_3$-FLG:ITO (best)	17	0.0014	0.0004	7	10	0.0004
Difference	(-96%)	(-99.8%)	(-99.4%)	(-53%)	(-63%)	(-99.8%)

Table 8.2 shows the results of these $FeCl_3$-FLG:ITO based OLEDs vs the standard ITO based OLEDs. The results of this are clear, $FeCl_3$-FLG:ITO do not work nearly as well as ITO OLEDs. The reasons for this are less clear. The likely major factor preventing better device performance is roughness. The transfer process of $FeCl_3$-FLG most likely increases roughness, adding polymer residues, wrinkles, and dust. It is of fundamental importance that the roughness issue with $FeCl_3$-FLG is solved before it can be seriously considered as an ITO replacement candidate.

There is one major positive that can be taken away from these results however, the turn-on voltage, and the voltage at peak luminance are much lower for the $FeCl_3$-FLG:ITO device than they are for ITO. This suggests that for domains where emission takes place, a much lower driving voltage is required, this is indicative of better work function matching between layers. It is likely that the deeper work function of $FeCl_3$-FLG is responsible for this. With a layer with roughness equivalent to ITO, and work function this deep, it is likely that device performance will be much better. This requires further investigation.

8.5 SUMMARY AND OUTLOOK

$FeCl_3$-FLG:ITO was investigated to see if the combined properties of $FeCl_3$-FLG and ITO could yield a working, flexible OLED using the methods described in this work.

The sheet resistance of $FeCl_3$-FLG:ITO was less than that of both $FeCl_3$-FLG and ITO separately, matching very well what would be expected for resistors in parallel. By combining the materials, I get an increase in conductivity.

The optical transmittance of $FeCl_3$-FLG:ITO is lower than the two materials separately. The transmittance appears close to the multiple of the transmittances indi-

vidually. The low transmittance of the combined material is a potential issue as it significantly reduces the figure of merit.

The bending performance results show a compromise of properties. The $FeCl_3$-FLG:ITO performs much better than ITO, but slightly worse than $FeCl_3$-FLG. After being bent around a radius of 3 mm just 3 times the FoM of ITO fell significantly below that of $FeCl_3$-FLG:ITO.

Raman spectroscopy indicated that the vibrational modes of $FeCl_3$-FLG are not affected by the ITO layer adjacent. The G peak maintains its shift due to intercalation and is not affected by strain.

The results of the $FeCl_3$-FLG:ITO TCE incorporated into an OLED are poor. The main device parameters, such as external quantum efficiency (EQE) are reduced by 99% or more. There is one important improvement in properties however, the operating voltages are significantly reduced. This is indicative of lower charge carrier injection barriers, therefore better matched work functions between layers. The poor results are likely caused by high surface roughness; however, the low operating voltage suggests that if this can be solved, $FeCl_3$-FLG:ITO could be a better TCE candidate than ITO.

More work is needed to optimise the transfer of few-layer graphene (FLG) and $FeCl_3$-FLG for smoother samples. This is the most significant area where the material differs to ITO. The deeper work function of $FeCl_3$-FLG, and the better bending and sheet resistance properties of $FeCl_3$-FLG:ITO could result in a suitable ITO replacement if this issue of fabrication can be solved.

BIBLIOGRAPHY

[1] The Uses Of ITO Coated Glass — Glass With ITO — Diamond Coatings.

[2] Sukanta De and Jonathan N. Coleman. Are there fundamental limitations on the sheet resistance and transmittance of thin graphene films? *ACS Nano*, 4(5):2713–2720, 5 2010.

[3] B. Amorim, A. Cortijo, F. De Juan, A. G. Grushin, F. Guinea, A. Gutiérrez-Rubio, H. Ochoa, V. Parente, R. Roldán, P. San-Jose, J. Schiefele, M. Sturla, and M. A.H. Vozmediano. Novel effects of strains in graphene and other two dimensional materials. *Physics Reports*, 617:1–54, 3 2016.

[4] T. M.G. Mohiuddin, A. Lombardo, R. R. Nair, A. Bonetti, G. Savini, R. Jalil, N. Bonini, D. M. Basko, C. Galiotis, N. Marzari, K. S. Novoselov, A. K. Geim, and A. C. Ferrari. Uniaxial strain in graphene by Raman spectroscopy: G peak splitting, Grüneisen parameters, and sample orientation. *Physical Review B - Condensed Matter and Materials Physics*, 79(20):205433, 5 2009.

9

FINAL REMARKS AND OUTLOOK

The purpose of this work was to investigate $FeCl_3$ intercalated FLG ($FeCl_3$-FLG), its properties as they relate to organic light-emitting diodes (OLEDs), how and if the material can be integrated into them, and what is the resulting performance compared to indium tin oxide (ITO) for a range of substrates, both rigid and flexible. To maintain relevance to low-cost commercial processes there was a stipulation that the OLED devices be fabricated in a way which maintains low temperature solution processability, and allows for device flexibility in order to remain relevant to future flexible and wearable devices.

In Chapter 4, I developed and improved upon some of the experimental setups used throughout this work. A single metric, ($< PosG >$), was developed to represent quality of intercalation. This allows for the direct comparison of different samples' levels of intercalation. This number can be compared for samples of all sizes, and can be calculated from measurements that can be taken quickly and non-destructively using Raman spectroscopy. From this a Raman mapping technique for assessing the quality of few-layer graphene (FLG) intercalation was developed which gives a more representative figure of the sample as a whole. The transfer process could be enhanced for large area samples using a new floating transfer method. A poly(vinyl alcohol) (PVA) enabled transfer method was also investigated, and warrants further investigation. The usefulness of $< PosG >$ was again seen when the $FeCl_3$-FLG fabrication process was optimised. There was an increase in $< PosG >$, and a reduction in sheet resistance of intercalated samples to $\approx 100\ \Omega/\square$ for a new powder zone temperature. The characterisation tools were also constructed, in order to evaluate the performance of OLEDs in this work. The external quantum efficiency (EQE) could now be estimated for devices

fabricated later using the setup introduced here, without the help of an expensive integrating sphere, keeping to the low-cost remit. Finally sample bending was introduced. A setup was built to repeatedly bend samples around a constant and fixed radius, thus subjecting a sample to a constant level of bending in a controlled and uniform way.

In Chapter 5 I investigated the role of $FeCl_3$-FLG in solution processed OLED devices. Rigid ITO and $FeCl_3$-FLG devices were measured and compared. I reported that the peak luminance and EQE were 39% and 47% less for the $FeCl_3$-FLG based device. This significant reduction in performance was likely caused by the low material transmittance, pinholes caused by the high roughness, and the lack of encapsulation exacerbating that issue. I noted that the turn-on voltage was equal to the ITO based device. This is indicative of good work function matching, despite the other issues. I then moved onto flexible substrates. I found that the resistance of ITO increases by a factor of 50 after just 100 bending cycles, while the resistance of $FeCl_3$-FLG increases by a factor of just 5 after 2000 bending cycles. $FeCl_3$-FLG is clearly a superior flexible conductor. OLEDs were then examined on flexible polyethylene terephthalate (PET) substrates. Here the performance of the ITO device was reduced compared to the rigid device, likely due to the increased surface roughness and sheet resistance of the substrate and transparent conductive electrode (TCE). I was unable to fabricate a working $FeCl_3$-FLG device on PET. Most likely for the same roughness related reason. I then examined OLEDs using an alternative architecture, these devices used the conventional device structure. For ITO devices this resulted in a large increase in performance, EQE increased by 150%. The failure of $FeCl_3$-FLG based devices here is again likely due to the surface roughness. Finally, I examined the unreported work carried out by a colleague using devices which involved the evaporation of MoO_3, and calcium. Here, in contrast with the solution processed work, the inverted devices showed better performance. The $FeCl_3$-FLG based devices outperformed the ITO based devices and showed better uniformity. In my work, the TCE appeared to be the common cause of failure. It is therefore extremely important to attempt to mitigate the effects of a rough TCE and also find a way of obtaining a smoother film.

In Chapter 6 in order to address some of the degradation and stability issues I investigated various ways of encapsulating the OLED devices which maintained the low-cost, solution processable remit of the work. Most interesting from this chapter was the work on the wax encapsulation. Here a beeswax was used to encapsulate the

entire device. The encapsulated devices remained at a useful luminance for almost 13 times longer than the unencapsulated devices. The degradation was slow enough that many measurements could be carried out to characterise the devices. Critically I have shown that this method of encapsulation is significantly better than the standard laboratory technique of epoxy encapsulation. This technique is also potentially scalable and compatible with current industry roll-to-roll techniques. This method offers the most promise going forward.

In Chapter 7 several additional ways of improving the device performance of $FeCl_3$-FLG based OLEDs were investigated. Roughness of various substrates and TCEs were investigated which resulted in the creation of a novel method of preparing $FeCl_3$-FLG. Here $FeCl_3$-FLG was inverted during the thermal transfer process and rather than being transferred to a destination substrate, it was investigated in its inverted state. The measured roughness of this inverted $FeCl_3$-FLG was found to be much less than that of $FeCl_3$-FLG, similar to ITO. This is significant given the effect roughness has had on devices throughout this work.

Finally in Chapter 8 I investigated a hybrid material which is a combination of $FeCl_3$-FLG and ITO. Here I showed that the transmittance was equal to the combination of the two constituent materials, and the sheet resistance was equal to the two taken as resistors in parallel. The bending performance too shows performance superior to ITO but worse than $FeCl_3$-FLG. The results of the $FeCl_3$-FLG enhanced ITO ($FeCl_3$-FLG:ITO) TCE incorporated into an OLED show the EQE is reduced by 99% or more. There is one important improvement in properties however, the operating voltages are significantly reduced. This is indicative of lower charge carrier injection barriers, therefore better matched work functions between layers. The low operating voltage suggests that if issues such as high surface roughness can be solved, as it was in Chapter 7, $FeCl_3$-FLG:ITO could be a better TCE candidate than ITO.

FUTURE WORK

I highlighted some positive results at the end of Chapters 6, 7, & 8 which all should be further investigated, optimised, and incorporated together.

The wax encapsulation presented in Chapter 6 needs to be expanded further to devices beyond OLED where there may be additional success. Different waxes, with

different melting temperatures should be investigated to provide a wax encapsulation layer with better mechanical robustness. Flexibility is important, but too soft and the layer will not be able to provide adequate protection to the device in commercial devices.

The results of Chapter 7 and Chapter 8 should be incorporated together. It would follow from my results that by using inverted $FeCl_3$-FLG to reduce roughness, and $FeCl_3$-FLG:ITO to enhance electrical performance, a new hybrid material could be fabricated, investigated, and incorporated into OLEDs. This has the potential to result in a $FeCl_3$-FLG based OLED with far superior properties to any fabricated thus far.

Looking at Chapter 4, the performance of the PVA transferred $FeCl_3$-FLG showed good results. It is worth investigating this material also in OLED devices. This material could be significantly better due to its copper growth, and residue free PVA transfer.

Finally there is an emerging single layer graphene (SLG) growth methodology emerging in the literature which does not involve transfers. This is the sapphire growth of SLG.[1] The next potential FLG for use in $FeCl_3$-FLG should come from a metal-free growth source. This will minimise contamination, reduce roughness, and reduce cost. It could be incorporated with a PVA transfer to build up to FLG before being intercalated. If successful a $FeCl_3$-FLG electrode fabricated in this way could be more suitable for OLEDs than the current $FeCl_3$-FLG produced in the way described in this work.

BIBLIOGRAPHY

[1] Zhichao Weng, Sebastian C. Dixon, Lok Yi Lee, Colin J. Humphreys, Ivor Guiney, Oliver Fenwick, and William P. Gillin. Wafer-Scale Graphene Anodes Replace Indium Tin Oxide in Organic Light-Emitting Diodes. *Advanced Optical Materials*, 10(3):2101675, 2 2022.

PUBLICATIONS

The ideas and data presented in this work are subject to the following publications and identified in the work where appropriate. This work has been presented multiple times at conferences as shown and I won an award for best poster at MRE2020 in London. The remaining unpublished portion of this work will be subject to several publications in progress.

PUBLICATIONS

- *"Improved Stability of Organic Photovotlaic Devices With $FeCl_3$ Intercalated Graphene Electrodes."* Walsh K, Murphy C, Craciun MF, Russo S. Frontiers In Electronics. 2021.
- *"Fully flexible, transparent electrodes for flexible photovoltaic applications."* Walsh K, Koh C, Murphy C, Russo S, Craciun MF. Optics InfoBase Conference Papers. 2020.
- *"Low Operating Voltage Carbon-Graphene Hybrid E-textile for Temperature Sensing."* Rajan G, Morgan JJ, Murphy C, Torres Alonso E, Wade J, Ott AK, Russo S, Alves H, Craciun MF, Neves AIS. ACS Appl Mater Interfaces. 2020.
- *"Wafer scale $FeCl_3$ intercalated graphene electrodes for photovoltaic applications."* Walsh K, Murphy C, Jones GF, Barnes M, De Sanctis A, Shin DW, Russo S, Craciun MF. SPIE Proceedings Photonics for Solar Energy Systems VII. 2018.

AWARDS

- Best Poster. Materials Research Exchange (MRE), London (2020). *"Iron chloride intercalated few-layer graphene electrodes in flexible OLED devices."*

CONFERENCES

- Materials Research Exchange (MRE), London (2020). Poster presentation, *"Iron chloride intercalated few-layer graphene electrodes in flexible OLED devices."*
- International OSA Network of Students (IONS), Exeter (2019). Oral presentation, *"Alternative transparent electrodes for OLEDs"*
- Materials for Clean Energy Conference (MCEC), Teddington (2019). Poster presentation, *"$FeCl_3$ doped few-layer graphene as flexible electrode in solution processed OLED devices."*
- Large-area, Organic and Printed Electronics Convention (LOPEC), Munich (2019). Poster presentation, *"Iron chloride intercalated few-layer graphene electrodes in flexible OLED devices."*

FUTURE PUBLICATIONS

- *"Highly stable, $FeCl_3$ intercalated few-layer graphene transparent electrode for organic light-emitting diodes."* Murphy C*, Lu L-P*, Sadhanala A, Walsh KK, Russo S, Friend RH, Craciun MF. (* - Authors contributions are equal.)
- *"Natural wax coating for long-lasting and waterproof optoelectronics"* Mastria R, Lam H T, Murphy C, Riisnaes K R, Kovalska E, Sadanandan K, Neves AIS, Coriolano A, De Marco L, Craciun MF, Russo S.
- *"Textile triboelectric nanogenerator with ultrasonic spray coated graphene electrode for wearable devices."* Sreeja Sadanandan K, Saadi Z, Murphy C, Grikalaite I, Craciun MF, Neves AIS.
- *"$FeCl_3$ intercalated few-layer graphene-ITO hybrid transparent conducting electrode for use in flexible optoelectronics."* Murphy C, Russo S, Craciun MF.